The potential of assimilating in situ airborne observations within the planetary boundary layer to enhance regional air quality analyses

I n a u g u r a l - D i s s e r t a t i o n
zur
Erlangung des Doktorgrades
der Mathematisch - Naturwissenschaftlichen Fakultät
der Universität zu Köln

vorgelegt von

Hassnae Erraji

aus Salé, Marokko

accepted in 2025

To all who see life
as an endless journey of learning

Abstract

Air pollution represents a serious threat to human health, the environment, and climate. One effective way to protect public health and take action to reduce emissions is through numerical model analysis, which depends on observational data to enhance the pollutant's representation at regional scales. While the observing system network is extensive and diverse, there is a concerning gap in observational data within the Planetary boundary layer (PBL), the most polluted part of the atmosphere, and the location of most emissions. This work aims to evaluate the potential of in situ airborne observations taken within the PBL to improve regional air quality analyses. To achieve this, the impact of assimilating these observations on the horizontal and vertical distribution of air pollutants has been assessed, and the added value of the observations within the PBL has been evaluated by comparing the analyses of different case studies to analyses in which ground-based observations are assimilated. Two types of observations within the PBL are analysed in two separate studies: drone-based and Zeppelin-based measurements. The drone data originate from the MesSBAR campaign in 2021, while the Zeppelin observations, collected in 2020, are used to investigate pollutant distributions in two distinct regions. The EURAD-IM model and its 4D-Var assimilation system are utilised to assimilate both types of observations. A high temporal resolution of 60 seconds and 5 km x 5 km horizontal resolution is employed to align with the high-resolution measurements. A joint optimisation of the initial values and emission rates is applied across all assimilation simulations. For both observation types, the 4D-Var assimilation positively improves the horizontal and vertical representation of pollutants. Despite the drone system being equipped with low-cost sensors, the analysis shows that ground concentrations of nitrogen oxide (NO), nitrogen dioxide (NO_2), and ozone (O_3) were primarily corrected at the campaign location during nighttime and early morning hours. Furthermore, the assimilation of drone observations leads to substantial adjustments of nitrogen oxides emission rates in the vicinity of the campaign site. The analysis applying Zeppelin observations assimilation indicates that these observations effectively enhance corrections of emissions originating from power plants and industrial sources released at high altitudes. Achieving similar results with ground-based observations is challenging due to their limited capacity to observe these elevated concentrations, except under strong wind conditions and enhanced vertical mixing. The comparison with independent observations reveals that assimilation of Zeppelin observations significantly enhances daytime surface O_3 concentrations by up to 54 %, whereas the assimilation of ground-based measurements only yields improvements of up to 22 %. Conversely, during nighttime, the assimilation of ground-based observations demonstrates superior performance, achieving an enhancement of up to 20 %, compared to just 6 % for the assimilation of Zeppelin observations. The daily O_3 analysis is best when

the observations from the Zeppelin and the ground stations are jointly assimilated, leading to additional improvement of up to 6% compared to other simulations. The improvements in the daytime O_3 concentrations resulting from the assimilation of Zeppelin observations are attributed to corrections applied to the initial values within the residual layer. Furthermore, in a polluted urban environment, the assimilation of Zeppelin observations results in a decline in performance during the night. Potential factors contributing to this deterioration include the model resolution, the representation of PBL height, and the poor representation of unobserved pollutants. The positive impact of assimilating in situ drone and Zeppelin data on air quality analyses underscores the importance of observations within the PBL. This importance is further reflected in the optimisation of emission rates, particularly for elevated sources such as power plants and industrial facilities. These findings confirm that PBL observations offer substantial added value compared to ground-based measurements. Therefore, there is a need to increase measurements within the PBL to address the existing observational gap and to provide valuable data for assimilation in air quality models.

Contents

List of Tables

List of Figures

List of Acronyms

4D-Var	Four Dimensional Variational Data Assimilation
CAMS	Copernicus Atmosphere Monitoring Service
CTM	Chemical Transport Model
DA	Data Assimilation
EEM	EURAD Emission Model
EF	Emission Factor
EURAD-IM	European Air pollution Dispersion–Inverse Model
GNFR	Gridding Nomenclature for Reporting
IFS	Integrated Forecasting System
IV	Initial Value
L-BFGS	Limited-memory Broyden-Fletcher-Goldfarb-Shenno algorithm
LIDAR	Light Detection and Ranging
MADE	Modal Aerosol Dynamics model for Europe
MEGAN	Model of Emissions of Gases and Aerosols from Nature
NRW	North Rhine-Westphalia
OSEs	Observing System Experiments
OSSE	Observing System Simulation Experiment
PBL	Planetary Boundary Layer
Radar	Radio Detection and Ranging
RMSE	Root Mean Square Error
S5P	Sentinel-5 Precursor
TNO	Dutch organisation for Applied Scientific Research

TROPOMI	Tropospheric Monitoring Instrument
UAV	Uncrewed Aerial Vehicle
UTC	Universal Time Coordinated
VOCs	Volatile Organic Compounds
WMO	World Meteorological Organisation
WRF	Weather Research and Forecasting Model

1

Introduction

A specific region of the atmosphere has been identified as being particularly important for air quality: the planetary boundary layer (PBL), sometimes also called the atmospheric boundary layer. This is the atmospheric layer closest to the Earth's surface up to a few kilometers in which most human activity takes place. In interaction with the Earth's surface, this layer goes through a typical daily cycle that shapes the physical and chemical processes linked to air pollution. Turbulence, horizontal and vertical dispersion, as well as vertical mixing with the mid and upper troposphere, cause significant variations in pollutant concentrations, while chemical transformations are driven by the interaction with biogenic and anthropogenic emissions in the PBL.

Despite its importance, the PBL remains a region of the atmosphere that lacks to be sufficiently observed. This lack of observations is a major obstacle to improving air quality forecasts (Liu et al., 2021). Several studies have shown that the vertical mixing within the PBL plays a role in determining pollutant concentrations, particularly ozone (O_3) (Qu et al., 2023; Kaser et al., 2017). Other studies have pointed to long-range transport and upper air concentrations as the reason behind the increase in ozone levels during several pollution episodes (Myriokefalitakis et al., 2016; Parrish et al., 2010; Jaffe, 2011). It is therefore imperative to increase the quantity of observations, particularly in the first few kilometers of the troposphere, to better characterise the dynamics and composition of this key region.

Severe pollution episodes result from the complex interaction between natural and anthropogenic emissions, meteorological conditions and chemical transformations. The accurate vertical representation of air pollutants, especially in the PBL, is crucial for understanding and predicting such events using chemical transport models (CTMs). However, current models have intrinsic limitations, as they reflect the current understanding of the atmosphere, which is limited and incomplete (Baklanov and Zhang, 2020; Sokhi et al., 2022). Consequently, the use of atmospheric observations to constrain and refine model predictions has consistently been an essential and well-established approach in atmospheric science (Bauer et al., 2015). This is achieved by the utilisation of data assimilation methods, which aim to correct the initial model state by incorporating additional data sources, such as observations, into the model.

Over the last 25 years, numerous studies have demonstrated the positive impact of data assim-

ilation (Sandu and Chai, 2011; Bocquet et al., 2015; Menut and Bessagnet, 2019) in the context of air quality. Current air quality models generally provide reliable forecasts; however, in the context of extreme weather events and severe pollution episodes, their performance may decline. A good reference to consider is the regional forecast for Europe produced by the Copernicus Atmosphere Monitoring Service (CAMS). The annual assessment of the analyses (i.e. simulations including data assimilation) for the year 2023 (Copernicus Atmosphere Monitoring Service, 2024), revealed that the ensemble of eleven regional models is generally well predicting O_3 with quite high correlation coefficients ranging from 0.8 to 0.9 compared to ground level observations. Nevertheless, the ensemble did not accurately predict exceptional high concentrations above 180 $\mu g\,m^{-3}$ during the summer period. The ozone analysis underestimates the ozone concentrations for southern Europe, where ozone pollution episodes are characterised by higher peak concentrations (Kilian et al., 2024; Chen et al., 2024). To further enhance the forecast accuracy, it is essential not only to increase the volume of observational data assimilated into models but also to prioritize the acquisition of observations from under-observed regions of the atmosphere, such as the PBL.

For several years, efforts have focused on satellites observations, which have become popular for air pollution assessment and monitoring. While a huge number of observations are available today, very few are assimilated by regional models. The reason for this is that these observations do not meet the necessary conditions due to their spatial and temporal resolution, the errors they contain (representativeness errors, noise, etc.) and their form as a full column profile (O_3 tropospheric columns, etc.). Vertical column observations have generally less sensitivity in the PBL due to the definition of the averaging kernel as well as atmospheric scattering and absorption in elevated altitudes of the atmosphere (Boersma et al., 2016). This assertion is supported by scientific research that has assimilated satellite measurements of key tropospheric pollutants such as O_3, nitrogen dioxide (NO_2) and carbon monoxide (CO), among others. In a study of a photochemical ozone pollution event over Europe, Foret et al. (2014) compared ozone retrievals from GOME-2 (Global Ozone Monitoring Experiment-2), OMI (Ozone Monitoring Instrument), and IASI (Infrared Atmospheric Sounding Interferometer) with regional models. Although IASI, with its 12 km resolution, showed a better ability to capture ozone structures compared to GOME-2 and OMI, it still not sufficient to provide accurate representation of ozone concentrations within the boundary layer due to limited sensitivity.

Since 2017, more and more attention has been focused on the state-of-the-art satellite instrument TROPOMI (Tropospheric Monitoring Instrument), with the potential to progress in atmospheric composition monitoring thanks to its high resolution (3.5 km×7 km). The TROPOMI NO_2 tropospheric column product, for example, has already been proven effective for applications such as emission inventory evaluation and point source discrimination in several studies (Beirle et al., 2021). However, in the context of data assimilation, several limitations and uncertainties of TROPOMI need to be considered. Firstly, the detected signal by the instrument is the result of a complex interaction between the absorption and scattering of light along its trajectory, which means that the data are mainly valid during the daytime (Poraicu et al., 2023). Then, clouds can partially or completely mask the signal because of their influence on solar irradiance (Boersma et al., 2004; Koelemeijer et al., 2001). As a result, only cloud-free or low-cloud locations will be observed. Moreover, aerosols and surface albedo produce uncertainties if they are not correctly parameterised in the retrievals. Since these satellite observations

are mainly tropospheric columns, it is necessary to use a model to generate an a priori vertical profile of the atmosphere, which is effectively another source of uncertainty to the retrieved vertical profile. Therefore, satellite data assimilation remains a challenge, intrinsically linked to the advancement of retrieval algorithms.

On the other hand, other types of observations have demonstrated their ability to accurately represent the PBL. These are ground-based remote sensing observations. Among these, aerosol lidars (Light Detection and Ranging), for example, are the strongest instrument for obtaining detailed vertical information on aerosols, as they contain less error than satellites retrievals, and allow vertical profiles to be obtained with high spatio-temporal resolution. Several studies confirmed the impact of lidar assimilation on improving the vertical profile of aerosols. A study by Wang et al. (2013) used an observing system simulation experiment (OSSE) to compare the impact of assimilating observations from 12 aerosol lidars in the European domain and assimilating in situ observations from 488 ground-based stations. The results show that the impact on the surface is almost the same for both types of observations, but the impact of assimilating the lidars lasts for a longer time. Whilst this study demonstrates that a similar impact on the surface can be achieved with a limited number of lidars, it also demonstrates that by optimising the location of the 12 lidars or by increasing their number, the impact is more pronounced and lasts even longer, since more improvements of the atmospheric state have been made at a high altitude. It also states that a lidar network as dense as ground stations seems a distant goal due to the high cost.

This finding is relevant to all instruments capable of delivering high-resolution vertical profiles of pollutants, including Fourier Transform Infrared Spectrophotometers (FTIR). Consequently, expanding the network of such instruments to adequately support the demands of regional models poses a significant challenge.

The emergence of Uncrewed Aerial Vehicles (UAVs), more commonly designated as drones, signifies a revolutionary advancement in atmospheric research. These novel technologies have arisen as efficient platforms for the conduct of measurements in the PBL. A substantial number of campaigns have been conducted for both meteorology (Hervo et al., 2023) and atmospheric composition assessment (for an overview, see Villa et al. (2016); Schuyler and Guzman (2017)). In the field of meteorology, a range of studies have been undertaken to evaluate the quality of collected data, and the subsequent assimilation of this data has been shown to enhance forecasting capabilities (Jensen et al., 2021; Sun et al., 2020). The use of drones in operational meteorology has even been recently a subject of discussion, leading to the largest drone-based measurement campaign in 2024 (UAS Demonstration Campaign (UAS-DC)) initiated by the World Meteorological Organisation (WMO, 2023). However, in the field of air pollution, studies that examine the assimilation of drone data into CTMs remain to be conducted. Consequently, the question concerning the efficacy of this data in enhancing model accuracy remains unresolved. One of the aims of this thesis is precisely to answer this question. Through the assimilation of UAV observations collected during a measurement campaign, the potential of these observations to improve analyses is studied. The aim is to assess the capacity of the drone platform that measure within the PBL to bring improvement to the regional air quality forecast.

Airborne measurement campaigns are also of interest for the assessment of pollutants in the PBL. More suited to research than operational forecasting, these campaigns are carried out as a mission to collect data ideal for studying the lower troposphere. Several campaigns have

been carried out in the past by aircraft and Zeppelins, such as MEGAPOLI in 2009 (Freney et al., 2014), PEGASOS in 2012-2013 (Rosati et al., 2016), ACT-America in 2019 (Barton-Grimley et al., 2022) and Zeppelin in 2020 (Tillmann et al., 2022). Of particular relevance here is the Zeppelin. As large, rigid airships, capable of long-duration, low-altitude flights, they are particularly well-suited for atmospheric research and detailed environmental measurements. However, few studies have been carried out to assimilate these observations to assess their impact on improving air quality forecasts. This gap represents an important scientific opportunity that will be explore in this thesis.

Considering the importance of observations measured in the PBL, the aim of this thesis is to evaluate the impact of assimilating such observations on the improvement of air quality analysis, using a regional chemical transport model. To this end, drone and Zeppelin observations from selected measurement campaigns were considered for data assimilation within the European Air Pollution Dispersion - Inverse Model (EURAD-IM), a state-of-the-art high-resolution model used in both research and operational contexts. The Four-Dimensional Variational (4D-Var) data assimilation technique (Elbern et al., 2007) was chosen to perform model simulations, as it is one of the most advanced and effective data assimilation methods. The 4D-Var corrects both the initial atmospheric state and the emission rates provided as input data to the model. Scientific studies have demonstrated that the simultaneous correction of both variables is the most effective approach to enhancing the accuracy of air quality forecasts (Tang et al., 2011; Peng et al., 2017; Zhang et al., 2022).
In this context, the thesis seeks to answer three main questions:

- What is the potential of drone platforms to improve the 4D-Var air quality analysis?
- What additional value do Zeppelin observations bring to the 4D-Var analysis, in comparison with ground-based observations?
- What are the limitations associated with assimilating observations within the PBL in the EURAD-IM model?

To address the first question, data assimilation experiments were conducted utilising vertical profiles of O_3 and NO from the two-day MesSBAR drone measurement campaign, conducted in 2021.

To investigate the second and third question, a subsequent study focuses on Zeppelin observations from a measurement campaign conducted in 2020. The period of 2020 offers a valuable opportunity to assess the capacity of the 4D-Var system of the EURAD-IM to adjust emission rates, given the significant reduction in emissions that occurred due to the societal restrictions during the COVID-19 pandemic.

This thesis is structured as follows: chapter 2 gives an overview of the 4D-Var data assimilation method for the joint optimisation of initial values and emission rates. The EURAD-IM system is introduced in chapter 3. In chapter 4, the observations used in this study are presented, while chapter 5 presents the MesSBAR case study. Finally, Chapter 6 presents the assimilation of Zeppelin observations and investigates their impact on analyses and emission optimisation, highlighting their added value and limitations. The main conclusions are summarised in chapter 7.

2

Data Assimilation

The objective of data assimilation (DA) is to produce an optimal estimation of the atmospheric state and/or model parameters within a dynamical system. This is accomplished by combining two primary sources of information: first, the a priori knowledge from the model, typically represented by its initial conditions, and second, the observational data. Both sources come with uncertainties. The DA process results in the best possible representation of the system state. This chapter introduces the theory of DA, starting with Bayes' theorem as the fundamental mathematical principle behind the DA approach. It then presents the four-dimensional variational data assimilation (4D-Var) method as implemented in the air quality model — EURAD-IM — used in this work.

2.1 Theoretical background

The Bayesian approach is adopted to solve the DA problem. Assuming that both the model and the observation error are stochastic, it becomes possible to describe these using probability density function (PDF) probabilities (Lorenc, 1986). The Bayesian formulation involves the *a posterior* probability $P(x|y)$ of the unknown variable x given the data y, which is superior to the *a priori* probability $P(x)$ taking into account the *likelihood* $P(y|x)$. This formulation illustrates the process of updating the distribution $P(x)$ in response to new information y. The posterior probability can be derived from Bayes' theorem as

$$P(x|y) = \frac{P(y|x)P(x)}{P(y)}. \tag{2.1}$$

In DA, the variable y denotes the observed data, while x represents the state of the model. To calculate the posterior probability, it is necessary to make an initial assumption: the Gaussian distribution for both the prior probability $P(x)$ and the likelihood $P(y|x)$. This leads to a simple representation of the DA problem. As a result, the probabilities can be expressed in the following format

$$P(y|x) = \frac{1}{\sqrt{2\pi\sigma_y^2}} e^{-\frac{(y-x)^2}{2\sigma_y^2}}, \tag{2.2}$$

$$P(x) = \frac{1}{\sqrt{2\pi\sigma_{x_b}^2}} e^{-\frac{(x-x_b)^2}{2\sigma_{x_b}^2}}, \tag{2.3}$$

Here σ_{x_b} and σ_y denote the standard deviations of the model state x and the observation y, respectively. Since the likelihood $P(y|x)$ is independent of the model state x, it acts as a normalisation constant in the Bayesian framework. As a result, the posterior distribution $P(x|y)$ can be simplified and expressed as shown in Equation (2.4)

$$P(x|y) \propto \exp\left[-\frac{1}{2}\left(\frac{(y-x)^2}{\sigma_y^2} + \frac{(x-x_b)^2}{\sigma_{x_b}^2}\right)\right] . \tag{2.4}$$

The objective is to determine the optimal state x_a that maximizes the posterior probability, representing the most likely model state given the observation y. This state, commonly referred to as the *analysis* in DA, is mathematically expressed as

$$x_a = \arg\max_x P(x|y) .$$

Given that (2.4) represents the probability as an exponential function, maximising the posterior probability is equivalent to minimising the function $J(x)$, where $J(x)$ corresponds to the exponent in the exponential expression

$$x_a = \arg\min_x J(x),$$

$$J(x) = \frac{1}{2}\left(\frac{(y-x)^2}{\sigma_y^2} + \frac{(x-x_b)^2}{\sigma_{x_b}^2}\right). \tag{2.5}$$

The function $J(x)$, known as the *cost function*, is quadratic. This ensures a unique global minimum, leading to a stable and well-posed solution in DA.

2.2 Four-dimensional variational data assimilation (4D-Var)

The 4D-Var method is a DA approach that estimates the model trajectory that best fits all available observations (y_0, . . . , y_p) over a given time window [t_0,t_k]. Like other variational methods, 4D-Var is based on maximising the posterior probability under the assumption of a Gaussian distribution, as outlined earlier. The 4D-Var incorporates both the three-dimensional spatial state and the temporal dimension within a variational assimilation framework. Thus, the state vector x is now represented in $\mathbb{R}^n$, where n denotes the number of model states. The a priori model state x_b is referred as the *background*. Likewise, the observation vector y is an element of $\mathbb{R}^p$, with p representing the number of observations. To reconcile the dimensional mismatch between the model space and observation space, a mapping operator $H : \mathbb{R}^n \to \mathbb{R}^p$ is introduced. This operator is known as the *observation* or *forward operator*.

In EURAD-IM, the 4D-Var formulation not only estimates the model initial state but also includes the emission rates $e \in \mathbb{R}^m$, with m being the dimension of the emission space.The eb is the background emission rates. The emission rates are considered as control parameter to be optimised, as described in Elbern et al. (2007). The resulting 4D-Var cost function is expressed as

$$
\begin{aligned}
J(x,e) &= J_b(x) + J_o(x) + J_e(e) \\
&= \frac{1}{2}(x - x_b)^T \mathbf{B}^{-1}(x - x_b) \\
&+ \frac{1}{2}\sum_{i=0}^{n}\Big((y_i - H_i M_i x)^T \mathbf{R}_i^{-1}(y_i - H_i M_i x)\Big) \\
&+ \frac{1}{2}(e - e_b)^T \mathbf{K}^{-1}(e - e_b)
\end{aligned}
\tag{2.6}
$$

Here, $\mathbf{R} \in \mathbb{R}^{p\times p}$, $\mathbf{B} \in \mathbb{R}^{n\times n}$, and $\mathbf{K} \in \mathbb{R}^{m\times m}$ are the observation, background and emission error-covariance matrices, respectively. The linearised model operator $M\colon \mathbb{R}^n \to \mathbb{R}^n$ propagates the state vector x forward in time from t_0 to the observation time t_i, associated with observation y_i.

Three key assumptions are made in the formulation of 4D-Var. First, the observation errors are assumed to be uncorrelated, meaning the observation error covariance matrix $\mathbf{R}$ is diagonal. Second, it is assumed that there is no correlation between the initial state and the emission rates. Finally, the model itself is considered to be perfect.

The solution x_a to Eq. 2.6, referred to as the *analysis*, is typically obtained by minimising the cost function, which involves computing the gradient with respect to the control parameters x and e

$$
\nabla_{(x_a,e)} J = 0 \ . \tag{2.7}
$$

The gradient is expressed as follows

$$
\begin{aligned}
\nabla_{(x,e)} J = \mathbf{B}^{-1}(x - x_b) + \mathbf{K}^{-1}(e - e_b) \\
- \sum_{t_i=t_0}^{t_n} H^T(t_i)\mathbf{R}^{-1}(\{y_o(t_i) - H(t_i)(x_b(t_i))\} - H(t_i)(x(t_i) - x_b(t_i)))
\end{aligned}
\tag{2.8}
$$

2.2.1 Pre-conditioning in the 4D-Var

A key limitation of the 4D-Var approach is its considerable computational cost, largely due to the iterative nature of the minimisation process required to determine the optimal solution. To enhance the efficiency and speed up convergence, a preconditioning technique is applied to the cost function within the 4D-Var algorithm (Zupanski, 1996). The preconditioning is done by performing a control variable transformation, which introduces the square roots of the background error covariance matrices $\mathbf{B}^{1/2}$ and $\mathbf{K}^{1/2}$

$$
\begin{aligned}
v &= \mathbf{B}^{-1/2}(x - x_b) \\
&= \mathbf{B}^{-1/2}\delta x
\end{aligned}
\tag{2.9}
$$

$$
\begin{aligned}
w &= \mathbf{K}^{-1/2} \ln\left(\frac{e}{e_b}\right) \\
&= \mathbf{K}^{-1/2}\delta u
\end{aligned}
\tag{2.10}
$$

The cost function $J(x,e)$ is then simplified, and its gradient ∇J is expressed in the form

$$
\nabla_{(v,w)^T} J = \begin{pmatrix} v \\ w \end{pmatrix} - \begin{pmatrix} \mathbf{B}^{1/2} & 0 \\ 0 & \mathbf{K}^{1/2} \end{pmatrix} \times \sum_{i=1}^{N} M^T(t_0,t_i) H^T \mathbf{R}^{-1}\left(d(t_i) - H\delta x(t_i)\right) \ . \tag{2.11}
$$

The minimisation problem is solved iteratively, as finding the exact solution that minimises the cost function would be computationally prohibitive. Instead, an approximate solution is obtained by performing a user-defined number of iterations. During each iteration, the control variables are updated through a two-step process. First, the forward model is executed to evaluate the cost function, followed by the backward model (adjoint) to compute the transformed gradient. The minimisation of the gradient is carried out using the limited-memory Broyden–Fletcher–Goldfarb–Shanno (L-BFGS) quasi-Newton method (Liu and Nocedal, 1989), which approximates the inverse of the Hessian matrix (the second derivative of the cost function) to efficiently locate the minimum. This procedure is also iterative and continues until a convergence criterion is satisfied or the maximum number of iterations is reached.

2.2.2 Covariance modelling

The formulation of the 4D-Var cost function (Eq. 2.6) incorporates uncertainties related to the background initial state (x_b) and the emission rates (e_b). Error covariance statistics quantifies these uncertainties: the **B** matrix represents error covariances in the background field, while the **K** matrix characterises uncertainties in emission inventories. Incorporating **B** and **K** into the cost function allows 4D-Var to enhance the analysis by balancing the trust in the background against the observations (with their errors represented in the **R** matrix). Furthermore, these matrices play a dynamic role in the assimilation process. The spatial error covariances determine how observational information is propagated throughout the model domain. The **B** matrix spatially distributes observation increments, ensuring that localised measurements influence neighbouring grid points in a physically consistent manner. Similarly, matrix **K** regulates the adjustment of emission corrections based on observations. This diffusion prevents overfitting to isolated data points and maintains balance in the analysed atmospheric state.
The full determination of the background error covariance matrices would require a priori knowledge of the true atmospheric state across the entire spatio-temporal domain, which is practically unfeasible. Therefore, these matrices cannot be computed explicitly but must be approximated. The following sections provide an overview of the formulation and estimation processes for the **B** and **K** matrices.

Background error covariance matrix

One of the primary challenges in chemical data assimilation is the enormous size of the background error covariance matrix **B**. This matrix has a size in the order of a magnitude of $O(10^{12})$ and explicitly storing it is infeasible. Therefore, it is necessary to approximate the **B** matrix to avoid using its full form. The idea of covariance modelling consists of presenting **B** as an operator. Weaver and Courtier (2001) demonstrated that the application of a diffusion operator can be an effective method for implementing spatial correlations that are typically Gaussian-shaped.
Since **B** is symmetric, it can be factorised as

$$\mathbf{B} = \Sigma C \Sigma, \tag{2.12}$$

where Σ is the diagonal of the background error covariance matrix **B**, representing the standard deviations, and C is a symmetric matrix of the background error correlations. C is defined such that $C = C^{1/2}C^{T/2}$, which results in

$$\mathbf{B} = \mathbf{B}^{1/2}\mathbf{B}^{T/2} = \Sigma C^{1/2} C^{T/2} \Sigma \ . \tag{2.13}$$

The covariance matrix $C^{T/2}$ is modelled using diffusion operators. The decomposition of the square root of the covariance matrix is given by:

$$C^{1/2} = \Lambda L_v^{1/2} L_h^{1/2} W^{-1/2} \tag{2.14}$$

Here, Λ is a normalisation operator; L_h and L_v are the horizontal and vertical diffusion operators, respectively; and W is a diagonal matrix of correction factors necessary for the grid, accounting for the varying heights of grid cells due to the application of σ-coordinates. Additionally, Λ serves as a diagonal matrix designed to counteract the flattening effects induced by the diffusion operators L.

Background emission rate covariance matrix

The background emission rate covariance matrix $\mathbf{K}$ is also factored to facilitate gradient calculation. In this context, Γ represents the standard deviations of the errors in the emitted species, while D denotes the background error correlation between different emitted species.

$$\begin{aligned} \mathbf{K} &= \Gamma D \Gamma \\ &= \Gamma D^{1/2} D^{T/2} \Gamma \end{aligned} \tag{2.15}$$

Although $\mathbf{K}$ is considerably smaller than the background error covariance matrix $\mathbf{B}$, further simplification is applied by treating $\mathbf{K}$ as block-diagonal, ignoring spatial covariances between species except at the same grid point. The standard deviations are provided by (Elbern et al., 2007), and the species correlations are detailed in Paschalidi (2015).

3

Regional air quality model EURAD-IM

To predict air quality, Chemical Transport Models (CTMs) are utilised to simulate the behavior of chemical pollutants in the atmosphere. The European Air pollution Dispersion-Inverse Model (EURAD-IM) is an Eulerian regional CTM that is used not only for atmospheric chemistry research (Franke et al., 2024; De Souza Fernandes Duarte et al., 2021; Vogel and Elbern, 2021) but also in operational forecasting as part of the Copernicus Atmosphere Monitoring Service (CAMS), which provides daily air pollution forecasts for Europe (Colette et al., 2024; Collin, 2020). Operating on a variable regional grid due to the nesting technique, EURAD-IM predicts trace gases and aerosols concentrations in the troposphere. The model includes a variational assimilation system for 3D-Var and 4D-Var (Elbern et al., 2007). The EURAD-IM is dynamically driven by the Weather Research and Forecasting Model (WRF) (Skamarock et al., 2008), which provides an offline meteorological coupling. This chapter provides a more detailed description of the EURAD-IM system.

3.1 Chemical transport model

The EURAD-IM CTM provides forecasts of a large set of gas phase and aerosol compounds in the troposphere. It incorporates the Regional Atmospheric Chemistry Mechanism with the Mainz Isoprene Mechanism (RACM-MIM) (Geiger et al., 2003), that solves a system of partial differential equations for more than 100 chemical species:

$$\frac{\partial c_i}{\partial t} = -\nabla(uc_i) + \nabla \cdot (K \nabla c_i) + A_i + E_i - D_i \tag{3.1}$$

$$A_i = P_i + L_i \tag{3.2}$$

where c_i is the concentration of chemical species i, u is the wind velocity, K is the eddy diffusivity tensor. A_i is the chemical transformation term, representing the net balance of chemical production rate P_i and chemical loss rate L_i for the species i, E_i is the emission rate, and D_i is the deposition rate.

A symmetric operator splitting method (McRae et al., 1982) is utilised to obtain the approximate solution of the partial differential equation (Eq. 3.1) for the dynamic processes, using the chemistry solver module C. The operator splitting scheme is applied to progress from time t to a future time $t + \Delta t$ in the following approach:

$$c_i(t + \Delta t) = T_h T_v D_v C D_v T_v T_h c_i(t) \ . \tag{3.3}$$

Each operator in the sequence represents a different physical or chemical process: T_v and T_h denote vertical and horizontal advection, respectively, which simulate the transport of the species by the atmospheric flow; D_v represent the vertical diffusion, accounting for mixing due to turbulence.

In EURAD-IM, aerosols are managed using the Modal Aerosol Dynamics module for Europe (MADE). This module provides information on the aerosols size distribution and their chemical composition. The aerosol dynamics include nucleation, condensation, coagulation, deposition (dry and wet) and sedimentation. The transport of aerosols is covered along with the gas-phase species. In addition, the MADE simulates the bidirectional exchange between the gas and aerosol phases, thereby accounting for the formation of secondary aerosols via the chemical transformation of gaseous organic and inorganic precursors. A further description for the MADE module could be found in Ackermann et al. (1998).

The emission rates E_i for each species are calculated online in the EURAD-IM. The biogenic emission rates are calculated using the Model of Emissions of Gases and Aerosols from Nature (MEGAN) (Guenther et al., 2012), while the anthropogenic emission rates are calculated in the EURAD emission module (EEM). The main role of EEM is to adapt the annual emissions, given by regional emission inventories, to the spatial and temporal discretisation of the EURAD-IM. Thus, the annual total emissions are converted into hourly emissions for each species and grid cells. A more detailed description of the emissions used in the simulations will be provided in the subsequent section 3.2.3.

The EURAD-IM includes an adjoint model operator M^T, which is essential for the backward calculations within the 4D-Var algorithm (as discussed in Section 2.2). The adjoint model development involves deriving adjoint operators for horizontal transport, vertical transport, vertical diffusion, and gas-phase chemistry. More details about the adjoint code are given in Elbern and Schmidt (1999); Elbern et al. (2007).

3.2 Model set-up and input

3.2.1 Meteorological model WRF

The Weather Research and Forecasting (WRF) model (Skamarock et al., 2008) is a state-of-the-art, limited-area numerical weather prediction system widely used for high-resolution atmospheric simulations. As an offline driver for the EURAD-IM, WRF provides critical meteorological fields, including three-dimensional wind vectors, temperature, pressure, turbulent diffusion coefficients, and planetary boundary layer height, which govern fundamental atmospheric processes such as advective transport, turbulent mixing, and pollutant dispersion within the EURAD-IM.

For this work, the WRF version 4.0.3 is used. The Integrated Forecasting System (IFS) (ECMWF, 2023) global reanalysis ERA5 (Hersbach et al., 2020) is used for the initials and boundary conditions for the WRF simulations.

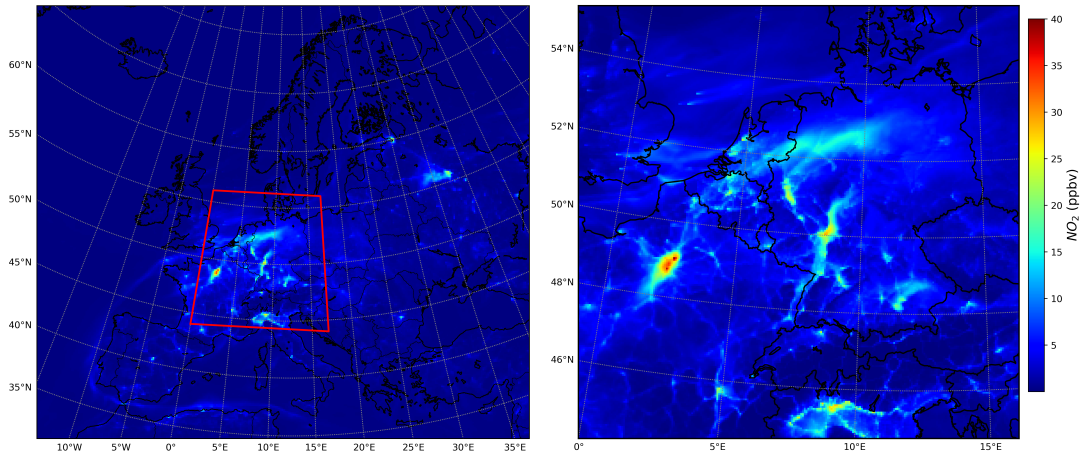

Figure 3.1: *The EURAD-IM model domains, highlighting the 15-km resolution mother domain (left) and the nested 5-km resolution domain (right). Fields of NO_2 concentrations (ppbv) are shown within each domain as example.*

3.2.2 Model discretisation

The model domain for EURAD-IM is defined using a Lambert conformal projection, with a central point situated at 51°N latitude and 12.5°E longitude. The model's horizontal grid structure, as for the WRF, is defined using the Arakawa C grid, as described by Arakawa and Lamb (1977) Arakawa and Lamb (1977). The simulation workflow is designed with a multilevel nesting approach, where a coarse domain captures broader regional dynamics, while a finer nested grid allows for more detailed resolution of local phenomena. The parent domain covers Europe with a resolution of 15 km x 15 km. For the simulations in this thesis a nesting factor of 3 allows to get a finer resolved domain of 5 km x 5 km (Fig. 3.1).
The model uses 30 vertical levels, ranging from the surface to 100 hPa, which corresponds to approximately 15 kilometers above sea level. The layers are defined using terrain-following sigma coordinates σ_k, which are specified as

$$\sigma_k = \frac{p_k - p_{\text{top}}}{p_{\text{bot}} - p_{\text{top}}} \ , \tag{3.4}$$

where p_k is the pressure at a given level k, p_{top} the pressure at the top of the model domain, and p_{bot} is the surface pressure. The level thickness is therefore variable: sigma layers are thinner near the surface, while at higher altitudes, the layers become thicker. There are about 17 layers within the lowest 1 km in altitude.
The model typically provides output on an hourly basis. However, the model performs its calculations at shorter a time step, set at 60 seconds for the 5 km resolution. For the purpose of this study, the output time resolution was adjusted to match the calculation time step.

3.2.3 Emissions

Emissions are used as the main input data to simulate the distribution and transformation of pollutants in the atmosphere. For anthropogenic emissions, annual emissions inventories are provided to EURAD-IM. For the simulations of this work, two inventories are used: the TNO-MACC_ II inventory (Kuenen et al., 2014) of the year 2016 and the CAMS-REG-v6 inventory (der Gon et al., 2023) for the year 2020. The year 2020 is notable for significant temporal

changes in emissions resulting from lockdowns and restrictions implemented in response to the COVID-19 pandemic (Balamurugan et al., 2021). To account for this, a technical modification was implemented in the EEM module to apply a daily adjustment factor that varies by sector, pollutant, and country for simulations using 2020 emissions, as outlined by (Guevara et al., 2022). Both inventories contain the emission rates of the following species: nitrogen oxides (NO_x), sulfur oxides (SO_x), carbon monoxide (CO), ammonia (NH_3), particulate matter with a diameter < 10 µm (PM_{10}), particulate matter with a diameter < 2.5 µm ($PM_{2.5}$), and total non-methane volatile organic compounds (NMVOCs). Emissions are also divided into 12 source sectors, known as Gridding Nomenclature for Reporting (GNFR) sectors, as shown in the Table 3.1.

Table 3.1: *Summary of the 12 GNFR sectors representing different sources of emissions in inventories used in this work.*

Letter	Name of the sector
A	Public power
B	Industry
C	Other stationary combustion
D	Fugitives
E	Solvents
F	Road transport
G	Shipping
H	Aviation
I	Off road
J	Waste
K	Agricultural livestock
L	Agricultural Other

Temporal distribution

The EURAD-IM requires hourly emissions data to simulate air quality, whereas emissions inventories are usually calculated as annual totals. The EEM module uses a sector-dependent temporal distribution to fit these totals to the model's requirements. To do this, it first splits the total emissions by month (1), then by day (2), and finally by hourly parts (3) for each emission species.

1. The monthly distribution allows splitting emissions to accurately represent seasonal variations, which may be especially significant in specific sectors, including agriculture and combustion.

2. The daily distribution primarily aims to calibrate emissions in response to variations between working and non-working days (Guevara et al., 2021). Further, an adjustment is made to account for the effects of public holidays and official vacation periods. The species-dependant daily emission profiles serve as strong constraints in the data assimilation process, ensuring that only daily emission totals are adjusted.

3. The hourly distribution is applied to each emission sector to represent hourly emissions. Certain sectors, such as transportation, exhibit a distribution significantly affected by working hours and peak periods at rush hours, whereas other sectors (e.g. shipping) show minimal hourly variation (Backes, 2023).

Vertical distribution

The vertical distribution of emissions is crucial, as they occur not only at the surface but also across various altitudes. In the EEM module, each sector has a specific vertical profile. Emissions from the energy, industry, and waste sectors are emitted at high altitudes up to 1000 m. In contrast, emissions from the shipping sector are concentrated in the range from 0 m to 100 m. The other sectors emit mainly at ground level around 20 m. It should be noted that the sectors emitting at high altitudes (energy, industry and waste) are significant sources of NO_x and CO, the two most emitted pollutants in the 5 km model domain. Indeed, these sectors are responsible for 40% of the total CO emissions and 35% of the NO_x emissions in the considered domain. Figure 3.2 shows the vertical distribution of CO and NO_x total emissions for these three sectors in Germany. CO is mainly emitted at an altitude of 150 m (corresponding to model level 6), while NO_x show a distribution over several levels up to 500 m.

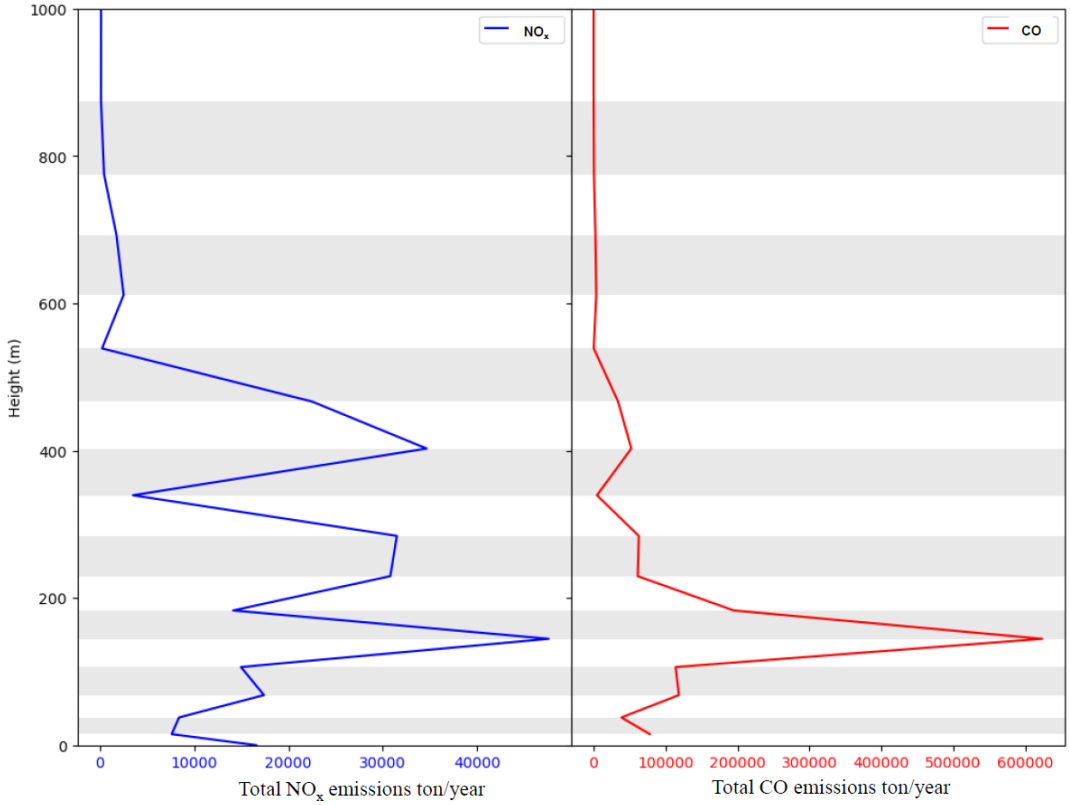

Figure 3.2: *Vertical distribution of the total 2016 TNO-MACC_ II emissions from the energy, industry and waste sectors in Germany, with NO_x emissions (left) and CO emissions (right).*

Temporal variability

Emissions are a major source of uncertainty in air quality forecasts, mainly due to their day-to-day variability, which is difficult to estimate and to predict. In addition, substantial fluctuations can occur from year to year, particularly in response to exceptional events, as it was the case in 2020. Figure 3.3 presents a comparison of the monthly total CO and NO_x emissions for the 5-km domain for three emission datasets: TNO-MACC_ II (2016), CAMS-REG-v6 (2020; business-as-usual scenario), and CAMS-REG-v6 adjusted via daily COVID-19 adjustment factors (Guevara et al., 2022). The daily scaling factors are applied to account for temporal variations in emission reductions during 2020. Unlike the business-as-usual scenario, which assumes constant activity levels, these adjustments reflect periods of significantly reduced emissions (e.g., due to lockdowns or policy measures).

The figure shows a strong annual variability between the 2016 and 2020 emissions. A total reduction of 66% in NO_x emissions and 34% in CO emissions was recorded between 2016 and 2020. This decline in emissions can be linked to Germany's transition to renewable energy, which includes closing down coal-fired power plants and the development of wind and solar energy (Xie et al., 2023). Furthermore, the implementation of Euro 6 standards for vehicles has also played a crucial role in reducing emissions from the transport sector (European Commission, 2022).

The COVID-19 pandemic caused a significant reduction in emissions compared to the business-as-usual scenario (der Gon et al., 2023; Umweltbundesamt, 2023). In particular, NO_x emissions are reduced by up to -30% in April. This period marks the beginning of the lockdown, which involved a strict reduction in mobility (Schlosser et al., 2020). A similar reduction is also evident for CO emissions that decreased by up to -19% in April. Overall, for 2020, the yearly NO_x emissions decreased by 11% and the yearly CO emissions by 5%, largely due to the impact of COVID-19.

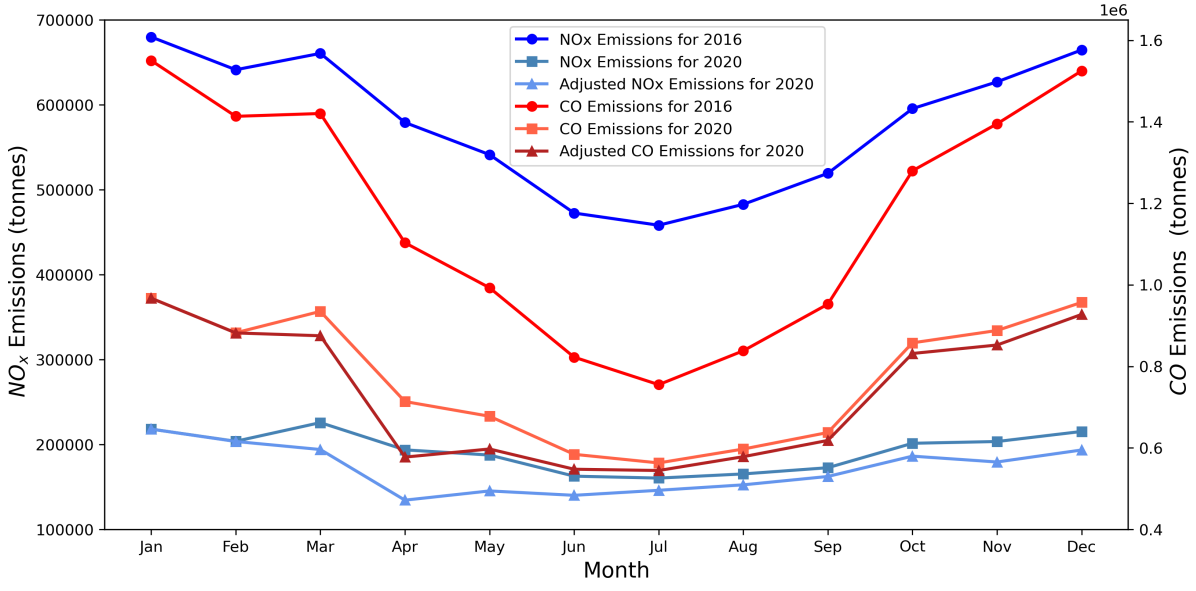

Figure 3.3: *Monthly variation of the total CO and NO_x emissions across three datasets within the 5 km domain: 2016 emissions, 2020 business-as-usual emissions, and adjusted 2020 emissions.*

4

Observations in the PBL

This chapter presents the observational data within the pbl that are assimilated in the EURAD-IM 4D-Var system and those that are used during the validation process. Additionally, this chapter describes the observation error estimation within the model.

4.1 Planetary boundary layer

The lowest layer of the atmosphere, called the planetary boundary layer, is of particular interest for air quality. This is the region where humans live and where pollution levels are often the highest, mainly due to the bulk of emissions. Stull (2012) defines the boundary layer as that part of the troposphere that is directly influenced by the presence of the Earth's surface, and responds to surface forcings with a timescale of about an hour or less. The dynamics of this layer play a crucial role in determining the distribution of pollutants. The thickness of the atmospheric boundary layer varies significantly throughout the day due to the diurnal cycle from several tens of meters to a few kilometers.
Fig. 4.1 illustrates the daily evolution of the PBL. At night, the nocturnal boundary layer is shallow, due to the absence of solar heating, leading to a stable, stratified atmosphere. In this shallow layer, pollutants from sources such as vehicles and industrial activities are trapped near the surface, leading to higher concentrations and poorer air quality. When the sun rises, the PBL increases in height as a results of the solar heating and convection, allowing for more efficient vertical mixing of the air in the mixed layer. This diurnal expansion dilutes the pollutants by spreading them over a larger volume, leading to lower concentrations at the surface. At sunset, the suppression of heat input halts convection, turning the once convective boundary layer into a calm residual layer. In this layer, turbulence fades, leaving a stratified air mass where trace gases and aerosols may accumulate. Near the ground, wind friction creates a new nocturnal boundary layer.

4.2 Assimilated observations

The aim of this study is to investigate the influence of observations in the planetary boundary layer (PBL) on air quality predictions using the EURAD-IM 4D-Var system. For this purpose, two categories of observations are considered: vertical profile measurements from a drone and

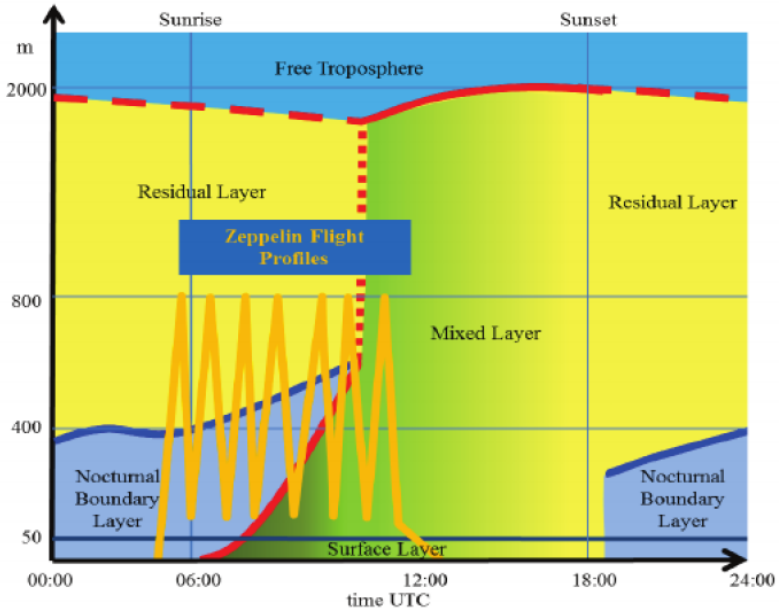

Figure 4.1: *The 24-hour evolution of the planetary boundary layer (PBL).The Zeppelin flight profiles are shown in orange. Source: Jäger (2014).*

in-flight measurements from a Zeppelin. The observations are analysed independently in two case studies in Chapters 5 and 6. In this chapter, these observations are presented and their contribution to atmospheric composition assessment and regional modelling is discussed.

4.2.1 Uncrewed aerial vehicles (UAVs) measurements

In recent decades, UAVs —drones— measurements have become a widely adopted measurement method (Marin et al., 2023; Villa et al., 2016), thanks to significant technological advances and their strong potential to fill critical gaps in the atmospheric observation system, particularly in the planetary boundary layer. These drones have revolutionised the collection of atmospheric composition and meteorological data, providing information on greenhouse gases, aerosols, trace gases, and weather conditions. Equipped with devices such as gas analyzers, spectrometers, meteorological sensors, and particle counters, drones provide vertical and horizontal profiles with high temporal resolution.

Advantages and limitations

The attractiveness of drones as in situ measurement platform lies in the many advantages they offer. First, their cost is considerably lower than that of aircraft or satellites, making them economically viable for a variety of applications in atmospheric research (Villa et al., 2016). Second, their great flexibility qualifies them not only to obtain vertical and horizontal profiles but also to perform measurements in difficult-to-access conditions, such as in arctic regions, nearby active volcanoes, or other remote locations (Lampert et al., 2020; Wood et al., 2020). Drones also allow for approaching emission sources for direct emission fluxes measurements (Bolek et al., 2024). Compared to aircraft, they offer the advantage of simple piloting, requiring less rigorous training and certification, especially for small drones that weigh only a few kilograms. In ad-

dition, drones can be piloted autonomously, with pre-programmed flight paths, thus covering all phases of the mission, from takeoff to landing (Segales et al., 2020). These advantages make drones a solution of choice for in situ data collection for monitoring atmospheric composition. Still, several restrictions of drones have to be considered. Their limited payload capability first affects weight, size, and quantity of onboard instrumentation. Additionally, flight time is a major limitation mostly controlled by the capacity of the onboarded batteries (Villa et al., 2016). Moreover, depending on the weight and size of the drones, specific flying authorisations are usually necessary to follow aviation safety regulations (Alamouri et al., 2021). These criteria can limit the maximum altitude drones are permitted to reach. Finally, weather circumstances constitute another constraint. Indeed, drone operations are often carried out in stable conditions for safety reasons, therefore their use may be limited in case of severe winds, precipitation, or reduced visibility.

The MesSBAR campaign

The MesSBAR project (2020-2023) was designed with the aim of developing UAV multicopter systems capable of autonomously measuring the concentrations of trace gases and particles in the PBL (Fig. 4.2). The development of the MesSBAR multicopter systems followed several requirements for design in order to produce an optimal, manageable, and suitable system that meets the campaign's objectives (Bretschneider et al., 2022). Two quadrocopter prototypes were built, each measuring 16543 mm in length and width, and 1137 mm in height including the payload. The total weight is roughly 25 kg, including payload.
As part of this project, two measurement campaigns took place: the first campaign was conducted in Wesseling, Germany, on 31 May and 01 June 2021. A second followed on 22 and 23 September 2021.
This study focuses on data collected during the second MesSBAR campaign on 22 and 23 September 2021, and concerns the assimilation of trace gas measurements only, namely O_3 and NO. Further details on this data will be presented in Chapter 6.

Figure 4.2: *The MesSBAR Multicopter drone. Source: Bretschneider et al. (2022).*

4.2.2 Zeppelin measurements

The Zeppelin NT is a semi-rigid airship designed for suspended and controlled flight using a lightweight and extremely stable structure that is filled with lighter-than-air helium gas

(Kazanas, 2017). This gas provides lift by displacing denser air, a consequence of Archimedes' law of buoyancy. The airship's rigid framework is composed of carbon-fiber and aluminium that maintains its shape independently of the lift gas. The structure is covered with is a high-strength multilayer laminate to reduce drag. The engines, passengers, and controls are housed in the suspended cabin below the airframe (Fig. 4.3). The Zeppelin has a length of 75 m, a height of 17.5 m, and a diameter of 14.2 m, with a hull volume of 8,425 m^3 (Brandt, 2007). It is capable of carrying a useful load of up to 1,950 kg, with the scientific equipment accounting up to 450 kg. The airship is capable of achieving a maximum speed of 130 $km\,h^{-1}$, with a typical cruising speed of 65 $km\,h^{-1}$, and operates at flight altitudes of up to 3 km. The maximum duration of continuous flights is up to 23 hours.

Figure 4.3: *The Zeppelin NT. Source: © Forschungszentrum Jülich/Ralf-Uwe Limbach.*

Advantages and limitations

The use of Zeppelin as a platform for measuring air pollutant concentrations has emerged as a promising solution to the prevailing observational gap in the PBL. This is strongly motivated by their unique advantages and capabilities, which significantly exceed those of other aircraft. Firstly, Zeppelins enable the measurement of vertical and/or horizontal profiles in PBL with high resolution, due to their relatively slow ascent and descent speeds of 5 $m\,s^{-1}$. Secondly, their capacity for transporting substantial loads facilitates the installation of numerous measuring instruments, including high quality sensors. This is a notable advantage over drones that are constrained by weight and typically utilise low-cost sensors with less accuracy. Moreover, a significant advantage of the Zeppelin lies in its cost-effectiveness when contrasted with alternative aircraft. Its operational requirements are minimal, requiring merely three personnel on the ground and a single pilot, consequently reducing the financial expense associated with measurement campaigns and scientific missions. In contrast, the necessity to comply with a pre-determined flight plan imposes certain constraints on the operational flexibility of Zeppelins when compared with drones. Nevertheless, a particularly noteworthy aspect of the functionality of Zeppelins is their capacity to maintain a constant position, thus facilitating the observation of

the temporal evolution of pollutants in the atmosphere and of emissions flux both from natural and anthropogenic sources. The operations of the Zeppelin NT are restricted to visual meteorological conditions. Specifically, the cloud base must exceed 400 meters above ground level, horizontal visibility must be greater than 5 km, and there should be no fog, hail, or snowfall. Additionally, flights are prohibited during predicted convective activity or in the presence of strong surface winds (https://zeppelinflug.de/).

The 2020 Zeppelin campaign

A measurement campaign with a Zeppelin NT platform was conducted in Germany in 2020. The objective of the campaign was to capture the vertical distribution of air pollutants and to investigate their emission sources. The campaign was organised in two phases: the first from May to June 2020, and the second in September 2020. A total of 172 take-offs and landings were conducted during transfer, commercial and targeted flights. For the present study, two periods of commercial flights that consist of several flights following the same route are analysed and presented here. Table 4.1 provides a comprehensive overview of the flights during these two periods.

- Period 1: This period of four days (29 May 2020, 01–03 June 2020) involved commercial flights departing from Bonn-Hangelar Airport and traversing the region between Bonn, Cologne, Düsseldorf and Möchengladbach. The flights ranged in altitude from the ground to 600 m above sea level, with an average altitude of 400 m.
- Period 2: Over a period of three days (11–13 September 2020), flights were conducted over the city of Frankfurt from Bad Homburg airfield. A series of flights was conducted with an altitude range between ground and 600 m, and an average altitude of 500 m above sea level.

On board the Zeppelin, two sets of instruments were utilised for the purpose of measuring pollutants. The first set was the MIRO instrument (Tillmann et al., 2022), and the second comprised a group of low-cost sensors (Schuldt et al., 2023). In order to ensure the highest possible quality of the data, the analysis is restricted exclusively to the data collected using the MIRO instrument.
The MIRO MGA10-GP is a state-of-the-art multi-compound gas analyzer developed by MIRO Analytical AG in Switzerland. This instrument is designed to measure 10 trace gases — NO, NO_2, O_3, SO_2, CO, CO_2, CH_4, H_2O, NH_3, and N_2O — with high precision and a time resolution of 1 s.

4.2.3 Ground-based observations

Ground-based stations form the most extensive network for monitoring air quality. In Europe, the European Environment Agency (EEA) aggregates hourly measurements of various pollutants, including ozone (O_3), nitrogen dioxide (NO_2), carbon monoxide (CO), particulate matter (PM_{10} and $PM_2 \cdot 5$), and sulfur dioxide (SO_2) from different sites. The Copernicus Atmosphere Monitoring Service (CAMS) validates these observations and incorporates them into data assimilation systems to produce daily air quality forecasts. This study will use a selection of ground-based observations provided by the CAMS for the regions under investigation for data

Table 4.1: *Flight schedule by period.*

Period	Date	First take-off	Last landing	Airport
Period 1	29 May 2020	08:00	18:04	Bonn-Hangelar (BNJ)
	01 June 2020	07:00	16:28	
	02 June 2020	08:00	17:46	
	03 June 2020	06:30	11:15	
Period 2	11 September 2020	09:10	17:00	Bad Homburg (BadH)
	12 September 2020	07:08	16:23	
	13 September 2020	07:07	16:22	

assimilation. A comprehensive list of these stations can be found in the appendix in Tables A.1 and A.2.

4.2.4 Observation error

The observation covariance error matrix R constitutes the variance and the covariance of the observation errors. It enables the consideration of systematic and representative errors in the observations in the assimilation algorithm. It is generally considered to be diagonal, under the assumption that the observation errors are not correlated.
The observation variance error is considered as the sum of measurement and representativeness errors (Kalnay, 2005). In certain instances, measurements are provided without any error information. In such cases, it is essential to estimate the measurement errors prior to the use of measurements within the data assimilation system. This study employs the methodology proposed by (Elbern et al., 2007) for such cases. By defining a relative error ϵ_{rel} and a minimal absolute error ϵ_{abs}, the measurement error is then given by

$$\epsilon_{meas} = \max(\epsilon_{abs}, \epsilon_{rel} \cdot y) \ . \tag{4.1}$$

The absolute and relative errors used in this work are presented for all analysed trace gases in Table 4.2.
The representation error ϵ_{rep} is calculated by applying the corresponding formula from (Elbern et al., 2007), which considers the grid cell spacing dx, the representativeness length of the measurement location L_x, and an absolute error ϵ_a specific to the measured species (Table 4.3). The formula is expressed as

$$\epsilon_{rep} = \sqrt{\frac{dx}{L_x}} \times \epsilon_a. \tag{4.2}$$

The grid cell spacing corresponds to the spatial resolution of the measurement grid, while the representativeness length indicates the effective range over which the measurement is considered representative (Table 4.4).

4.3 Data for model validation

Ground-based observations

To validate the performance of the model, ground-based observations from the TOAR database (Tropospheric Ozone Assessment Report) are used (Schultz et al., 2017). This database in-

Table 4.2: *The values of the relative ϵ_{rel} and absolute ϵ_{abs} errors per species that are utilised to calculate the measurement error for the observations that are assimilated.*

Species	O_3	NO	NO_2	CO
ϵ_{abs} (ppbv)	1.5	1	1.5	30
ϵ_{rel} (%)	10	10	15	15

Table 4.3: *The absolute error ϵ_a for each species utilised in the estimation of the representative error.*

Species	ϵ_a (ppbv)
O_3	2
NO	3
NO_2	1.8
CO	30

Table 4.4: *The representativeness length L_x for each type of stations as applied in EURAD-IM.*

Station type	L_x
Remote/Mountain	20 km
Rural	10 km
Suburban	4 km
Urban	2 km
Traffic	1 km
Unknown	3 km

cludes data from several providers, including the European Environment Agency (EEA) and the German Environment Agency (UBA). The TOAR database provides hourly data of long-term surface in situ air quality measurements from a global network of over 23,000 stations (https://toar-data.org/ and https://toar-data.fz-juelich.de/). Within Germany, approximately 1424 stations are available, including diverse stations types such as background, traffic, industrial stations, and stations located in urban, suburban, and remote areas. While the database offers a comprehensive list of variables, in this study, the primary focus is placed on O_3, NO and NO_2 observations. Only ground-based stations in the study area were used for model results validation. Assimilated stations were excluded.

Satellite observations

The Tropospheric Monitoring Instrument (TROPOMI) on board the Sentinel-5 Precursor (S5P) satellite is a state-of-the-art spectrometer for global monitoring of atmospheric composition with high spatio-temporal resolution (Veefkind et al., 2012). Its main mission is to detect a range of trace gases, aerosols and cloud properties with a focus on air quality, climate change and the ozone layer. Since its launch on 13 October 2017, TROPOMI has been in a polar orbit, making measurements in the ultraviolet (UV), visible, near infrared and shortwave infrared spectral regions with an initial spatial resolution of 3.5x7 km^2, later in 2019 increased to 3.5x5.5 km^2 (Lakkala et al., 2020). The tropospheric NO_2 column data is a key product of the TROPOMI instrument. It refers to the total amount of NO_2 present in a vertical column of the atmosphere

within the troposphere. These high-resolution satellite observations are used to identify hotspots of NO_2 emissions, monitor trends in emissions and support assessments of air quality. For example, NO_2 data are used to validate models (Ialongo et al., 2020) and derive emissions (Lorente and Boersma, 2019; Wang et al., 2020).

In this work, observational data from the TROPOMI NO_2 retrievals are used for comparison with the EURAD-IM outputs to validate NO_2 emissions. The NO_2 data are derived from the TROPOMI Near-Real-Time Initial (NRTI) product, a Level-2 retrieval at 3.5×5.5 km^2 nadir resolution (version v01.03.02). This data provides the total tropospheric NO_2 column from surface to tropopause and includes quality metrics. Before comparing the TROPOMI NO_2 columns with the model results, the averaging kernel is applied to ensure that the comparison takes the specific sensitivity of TROPOMI into account, which strongly depends on the height in the troposphere due to the meteorological conditions. This treatment is explained in Douros et al. (2023). In addition, only data with a quality flag greater than 0.75 are used. This is important for using high-quality data that is not affected by clouds.

5

The potential of drone observations to improve air quality predictions

One approach that addresses the lack of observations within the planetary boundary layer (PBL) is the utilisation of drone systems to obtain vertical and horizontal profiles within the lowest hundreds of meters of the troposphere. Despite the increase in drone measurement campaigns in recent years, there have been no modelling studies that investigate the impact of assimilating these observations on air quality analysis. This study aims to evaluate the potential of drone observations to enhance the analysis of regional air quality. To this end, an assimilation study using in situ drone observations is conducted to investigate their impact on pollutant representation and the ability of emission optimisation.

This work was conducted as part of the MesSBAR[1] project, which focused on the development of multi-copter drone systems to perform high-resolution measurements of air pollutants in urban environments. This study specifically examines the ozone and nitrogen monoxide concentrations recorded during a two-day measurement campaign conducted near Wesseling, Germany, on the 22 and 23 September 2021. The analysis was realised using the EURAD-IM and the 4D-Var data assimilation method. The findings indicate that the assimilation of drone data significantly improves the horizontal and vertical representation of pollutants in the PBL. Furthermore, the results show that the assimilation of drone observations results in substantial corrections of nitrogen oxides emission rates in the grids surrounding the observation site, thereby contributing to the improvement of air quality analyses. This study's results support the assimilation of drone data in modelling applications, highlighting the potential of such aerial platforms as an effective solution for addressing the observational gap in the PBL.

The results of this study are presented in the following published article:

Erraji, H., Franke, P., Lampert, A., Schuldt, T., Tillmann, R., Wahner, A., and Lange, A. C.: The potential of drone observations to improve air quality predictions by 4D-Var, Atmospheric Chemistry and Physics, 24, 13913–13934, https://doi.org/10.5194/acp-24-13913-2024, 2024.

[1] Automatisierte luftgestützte **Mes**sung der **S**chadstoff**B**elastung in der erdnahen **A**tmosphäre in urbanen **R**äumen / Automated airborne measurement of air pollution levels in the near earth atmosphere in urban areas

Atmos. Chem. Phys., 24, 13913–13934, 2024
https://doi.org/10.5194/acp-24-13913-2024

Atmospheric Chemistry and Physics
Open Access
EGU

The potential of drone observations to improve air quality predictions by 4D-Var

Hassnae Erraji[1], Philipp Franke[1], Astrid Lampert[2], Tobias Schuldt[1], Ralf Tillmann[1], Andreas Wahner[1], and Anne Caroline Lange[1]

[1]Forschungszentrum Jülich GmbH, Institute of Climate and Energy Systems – Troposphere (ICE-3), Jülich, Germany
[2]Institute of Flight Guidance, TU Braunschweig, Braunschweig, Germany

Correspondence: Anne Caroline Lange (ann.lange@fz-juelich.de)

Received: 21 February 2024 – Discussion started: 19 March 2024
Revised: 16 October 2024 – Accepted: 16 October 2024 – Published: 16 December 2024

Abstract. Vertical profiles of atmospheric pollutants, acquired by uncrewed aerial vehicles (UAVs, known as drones), represent a new type of observation that can help to fill the existing observation gap in the planetary boundary layer (PBL). This article presents the first study of assimilating air pollutant observations from drones to evaluate the impact on local air quality analysis. The study uses the high-resolution air quality model EURAD-IM (EURopean Air pollution Dispersion – Inverse Model), including the four-dimensional variational data assimilation system (4D-Var), to perform the assimilation of ozone (O_3) and nitrogen oxide (NO) vertical profiles. 4D-Var is an inverse modelling technique that allows for simultaneous adjustments of initial values and emissions rates. The drone data were collected during the MesSBAR (automated airborne measurement of air pollution levels in the near-earth atmosphere in urban areas) field campaign, which was conducted in Wesseling, Germany, on 22–23 September 2021. The results show that the 4D-Var assimilation of high-resolution drone measurements has a beneficial impact on the representation of regional air pollutants within the model. On both days, a significant improvement in the vertical distribution of O_3 and NO is noticed in the analysis compared to the reference simulation without data assimilation. Moreover, the validation of the analysis against independent observations shows an overall improvement in the bias, root mean square error, and correlation for O_3, NO, and NO_2 (nitrogen dioxide) ground concentrations at the measurement site as well as in the surrounding region. Furthermore, the assimilation allows for the deduction of emission correction factors in the area near the measurement site, which significantly contributes to the improvement in the analysis.

1 Introduction

In response to the increasing need for high-resolution and accurate air quality forecasts, extended efforts to improve the performance of chemical transport models (CTMs) have been made over recent decades. One of the effective means of improvement involves the use of advanced data assimilation techniques (Elbern et al., 2007; Liu et al., 2017; Klonecki et al., 2012). The aim is to combine observations and model data to obtain a better representation of the pollutants in the atmosphere as well as to optimise the input parameters, such as emissions, when considering inverse models. Although data assimilation holds significant potential for enhancing air quality modelling, its application is often still limited due to the scarcity of available observational data. In fact, the observational data types, which are usually used for assimilation (ground-based, airborne, and satellite observations), are certainly valuable for enhancing forecast accuracy, but they remain insufficient due to various constraints related to their availability, resolution, and especially their limited vertical coverage. Ground-based observations are the major source of information for regional CTMs and are generally taken from in situ monitoring networks. Even if they are fairly dense in the horizontal distribution on a regional scale, no information regarding the vertical distribu-

tion of air pollutants is provided. In contrast, lidar (light detection and ranging) remote sensing instruments and in situ sonde measurements can provide this information, but unfortunately, only a sparse and limited number of such stations exists. Similarly, ground-based Fourier transform infrared (FTIR) spectrometers, which are part of the Network for the Detection of Atmospheric Composition Change (NDACC), are capable of retrieving vertically resolved mixing ratios for a range of atmospheric constituents. However, the vertical resolution of these profiles is constrained by their dependence on a priori information, and the network's spatial coverage remains sparse (De Mazière et al., 2018; García et al., 2021). Multi-axis differential optical absorption spectroscopy (MAX-DOAS) is also capable of retrieving trace-gas and aerosol vertical profiles (Tirpitz et al., 2021). Airborne observations (e.g. In-service Aircraft for a Global Observing System – IAGOS – or flight campaigns) provide high-resolution vertical profiles during take-off and landing; however, the spatial coverage is still limited because of the high costs (Wang et al., 2022; Petetin et al., 2018; Tillmann et al., 2022). Satellite retrievals mainly provide the total column of air pollutants, thus providing little information on the vertical distribution of the air pollutant concentrations in the planetary boundary layer (PBL) and at the earth surface (Martin, 2008). Consequently, a significant observational gap exists in the PBL, which is the lowest part of the atmosphere characterised by the highest concentrations of air pollutants due to its vicinity to anthropogenic emission sources (Scheffe et al., 2009).

Uncrewed aerial vehicles (UAVs), also known as drones, are comparatively new measurement platforms that have begun to be widely utilised in recent years to obtain in situ measurements of atmospheric trace gases and aerosols within the lower atmosphere (Schuyler and Guzman, 2017; Yang et al., 2023), bringing many opportunities to improve air pollution monitoring. The increase in drone applications comes mainly from their numerous advantages, such as portability and flexibility, while being affordable. In addition, they can provide in situ observations of various atmospheric constituents with high temporal and vertical resolution (Lawrence and Balsley, 2013). However, drone measurements come with some limitations as, for instance, flights are complicated during strong wind conditions, require good visibility, and are often restricted to maximum altitudes due to aviation safety reasons. Nevertheless, they can fill the existing observational gap in the PBL and provide valuable information on the distribution of air pollutants.

Several studies present drone campaigns that have observed the atmospheric composition and meteorological parameters during the last 2 decades (Villa et al., 2016; Bretschneider et al., 2022). The measured data, mostly from the PBL region, were used for research on the atmospheric boundary layer (Wang et al., 2021) and pollutants' variability and distribution (Altstädter et al., 2015; Illingworth et al., 2014), as well as to study the properties of aerosols (Roberts et al., 2008; Corrigan et al., 2008) and to qualify local emissions sources (Nathan et al., 2015). Furthermore, drone campaigns have been conducted in remote areas, such as the Arctic and Antarctic regions (Lampert et al., 2020), as well as during volcano eruptions (Diaz et al., 2012).

To our knowledge, the assimilation of drone observations has only been tested in the context of numerical weather prediction (NWP) models (Flagg et al., 2018; Leuenberger et al., 2020), and no study has yet explored their impact in the case of chemical data assimilation. Meteorological studies have shown that the assimilation of meteorological drone data has a positive impact on improving weather forecasts. This has prompted further ongoing research regarding the possibility of implementing drone observations in support of operational meteorology forecasting and for real-time data assimilation studies (O'Sullivan et al., 2021). Impact studies have revealed a large improvement in the vertical distribution of temperature, relative humidity, and wind, as well as a reduction in bias and root mean square error (RMSE), when drone observations are assimilated using a variational data assimilation system within high-resolution NWP models (Jonassen et al., 2012; Flagg et al., 2018; Jensen et al., 2021; Sun et al., 2020; Leuenberger et al., 2020).

Given the positive impact that has been reported in the case of meteorological applications, questions arise about the potential benefits and limitations of drone observations when assimilated within a CTM. In this study, the impact of drone data assimilation on air quality analyses is investigated using the regional and high-resolution EURopean Air pollution Dispersion – Inverse Model (EURAD-IM) with its four-dimensional variational (4D-Var) data assimilation system (Elbern et al., 2007). Vertical profiles of ozone (O_3) and nitrogen oxide (NO) collected during the MesSBAR (Automatisierte luftgestützte Messung der Schadstoff-Belastung in der erdnahen Atmosphäre in urbanen Räumen – automated airborne measurement of air pollution levels in the near-earth atmosphere in urban areas) field campaign are assimilated. The potential of drone observations to improve air quality analysis and forecast is explored in a 2 d (day) case study by applying the joint optimisation of initial values and emission rates. The aim is to investigate the ability of the 4D-Var system to adjust local emission rates using vertical profiles that were collected in a region characterised by diverse emission sources. This paper is structured as follows: in Sect. 2, the EURAD-IM and its 4D-Var data assimilation system are presented. The MesSBAR field campaign and the experimental design are described in Sect. 3. The results of the 4D-Var data assimilation experiments are discussed in Sect. 4. Finally, the summary and conclusions are given in Sect. 5.

2 The modelling system

2.1 The EURAD-IM model

EURAD-IM (EURopean Air pollution Dispersion – Inverse Model) is a three-dimensional high-resolution Eulerian CTM simulating air pollution in the troposphere at continental to regional scales. It has been used for several scientific studies for air quality forecasting, episode scenarios, data assimilation, and inverse modelling (Deroubaix et al., 2024; Gama et al., 2019; Elbern et al., 2007; Duarte et al., 2021; Franke et al., 2022, 2024). EURAD-IM is part of the regional Copernicus Atmosphere Monitoring Service (CAMS), providing daily air quality forecasts and reanalysis over Europe which enable continuous quality assurance using observations and inter-model evaluation (Marécal et al., 2015).

Table 1 presents a summary of the specific model settings and modules utilised in the EURAD-IM configuration employed in this study. EURAD-IM describes the transport by diffusion and advection of various trace-gas components emitted both by anthropogenic and biogenic sources and considers the gas-phase chemical transformation of about 110 chemical species with 265 reactions. The MADE (Modal Aerosol Dynamics model for Europe) module is employed to investigate aerosol dynamics within EURAD-IM, providing information on aerosol size distribution and chemical composition. This module simulates the formation and transformation of both primary and secondary aerosols, considering the interactions between the gas phase and aerosols. EURAD-IM accounts for the loss of chemical components through wet and dry deposition, as well as aerosol sedimentation. Moreover, EURAD-IM includes a 4D-Var assimilation system, as described in the subsequent section, along with the adjoint code derived from the forward code detailed in Elbern et al. (2007). The adjoint model incorporates the transport, diffusion, and gas transformation processes of the chemical species as well as secondary inorganic aerosol formation.

The CTM is driven by meteorological fields from the Weather Research and Forecasting (WRF) model (version 3.7; Skamarock et al., 2008) as thermodynamical forcing. The ECMWF (European Centre for Medium-Range Weather Forecasts) IFS (Integrated Forecasting System) global analysis (ERA5) is used for initialisation and boundary conditions for the WRF simulations. Chemical boundary conditions are generated by the CAMS global reanalysis data set (EAC4) that is produced by the ECMWF Composition Integrated Forecasting System (C-IFS). Anthropogenic emissions used for this study are provided by the German Environment Agency (Umweltbundesamt, UBA) for Germany and by the TNO-MACC_II inventory (Kuenen et al., 2014) for the rest of Europe. The emission data set is subject to processing in the EURAD Emission Module (EEM) (Memmesheimer et al., 1995) for seasonal and diurnal redistribution, as well as attributions to working days and weekends. The emission data are divided into point and area sources. The data contain emissions of gaseous air pollutants, i.e. carbon monoxide (CO), nitrogen oxides (NO_x), sulfur dioxide (SO_2), total non-methane volatile organic compounds (NMVOCs), and ammonia (NH_3), as well as the aerosols PM_{10} (particulate matter with a diameter $< 10\,\mu m$) and $PM_{2.5}$ (particulate matter with a diameter $< 2.5\,\mu m$). Biogenic emissions are calculated online using the Model of Emissions of Gases and Aerosols from Nature (MEGAN), while wild-fire emissions are not considered here and did not play a role in the investigated case.

2.2 4D-Var data assimilation

The EURAD-IM data assimilation system is based on the 4D-Var method as described in Elbern and Schmidt (2001) and Elbern et al. (2007). The 4D-Var approach aims to determine the optimal model state by combining the prior information (e.g. provided by a forecast) with observational data over an assimilation window through the minimisation of the following cost function $\mathcal{J}$:

$$\begin{aligned}\mathcal{J}(\boldsymbol{x}_0, \boldsymbol{e}) &= \mathcal{J}_\mathrm{b}(\boldsymbol{x}_0) + \mathcal{J}_\mathrm{o}(\boldsymbol{x}_0) + \mathcal{J}_\mathrm{e}(\boldsymbol{e}) \\ &= \frac{1}{2}\left(\boldsymbol{x}_0 - \boldsymbol{x}^b\right)^T \mathbf{B}^{-1}\left(\boldsymbol{x}_0 - \boldsymbol{x}^b\right) + \frac{1}{2} \\ &\sum_{i=0}^{n}\left(\left(\boldsymbol{y}_i - \mathbf{H}_i\mathbf{M}_i\boldsymbol{x}_0\right)^T \mathbf{R}_i^{-1}\left(\boldsymbol{y}_i - \mathbf{H}_i\mathbf{M}_i\boldsymbol{x}_0\right)\right) \\ &+ \frac{1}{2}\left(\boldsymbol{e} - \boldsymbol{e}^b\right)^T \mathbf{K}^{-1}\left(\boldsymbol{e} - \boldsymbol{e}^b\right). \end{aligned} \quad (1)$$

Here, the optimisation is subject to the initial conditions $\boldsymbol{x}_0$ and the emission correction factor $\boldsymbol{e}$. The cost function equation includes an additional element (in contrast to the usual 4D-Var used for NWP) that accounts for emissions ($\mathcal{J}_\mathrm{e}(\boldsymbol{e})$). The model state is mapped from the model space to the observation space by the observation operator $\mathbf{H}_i$ and the model operator $\mathbf{M}_i$, producing the model equivalents of each observation $\boldsymbol{y}_i$. The matrices $\mathbf{B}$, $\mathbf{R}$, and $\mathbf{K}$ represent the error covariance matrices associated with the a priori state vector $\boldsymbol{x}^b$, the observations $\boldsymbol{y}_i$, and a priori emissions $\boldsymbol{e}^b$, respectively. The matrix $\mathbf{R}$ considers only diagonal elements (i.e. it ignores any error correlation between different observations) while accounting for the uncertainties in the measurements and model representation error. The matrix $\mathbf{B}$ is estimated using error variances and the diffusion operator proposed by Weaver and Courtier (2001). Thus, $\mathbf{B}$ can be factorised as $\mathbf{B} = \mathbf{B}^{1/2}\mathbf{B}^{T/2}$ for use in the preconditioning of the highly underdetermined data assimilation system. The matrix $\mathbf{K}$ is defined as block diagonal, with non-zero entries for correlations between species and nearby emissions. The variance and correlation values are provided in Paschalidi (2015). The minimisation of the cost function $\mathcal{J}$ is performed through an iterative process using the quasi-Newton limited-memory L-BFGS algorithm (Liu and Nocedal, 1989), which includes

Table 1. Summary of EURAD-IM configuration.

	Processes	Modules and references
Transport	Advection	Walcek scheme (Walcek, 2000)
Gas-phase chemistry	Kinetic chemistry mechanism	RACM-MIM (Stockwell et al., 1997)
	Dry deposition	Zhang et al. (2003) scheme
	Wet deposition	Roselle and Binkowski (1999)
	Chemistry solver	KPP (Sandu and Sander, 2006)
Aerosols	Aerosol dynamics	MADE (Ackermann et al., 1998)
	Secondary inorganic aerosols	HDMR (Rabitz and Aliş, 1999)
	Secondary organic aerosols	SORGAM (Schell et al., 2001)
Emissions	Biogenic emissions	MEGAN (Guenther et al., 2012)
	Anthropogenic emissions	TNO–UBA emission inventory (Kuenen et al., 2014)
Assimilation	4D-Var system	Elbern et al. (2007)
	Minimisation algorithm	L-BFGS algorithm (Liu and Nocedal, 1989)
	Background error covariance modelling	Weaver and Courtier (2001)

the iterative integration of the forward and adjoint EURAD-IM.

3 The MesSBAR campaign analysis

3.1 Air quality measurements

The MesSBAR field campaign took place near Wesseling, Germany, on 22–23 September 2021. During these 2 d, a multicopter system composed of a drone and a set of low-cost air quality monitoring instruments was used to carry out vertical profile measurements of air pollutants during the morning hours. Among the instruments loaded on the multicopter, electrochemical sensors were used to monitor nitrogen oxide (NO), and a personal ozone monitor (POM) was deployed for assessing ozone (O_3) concentrations. The NO drone observations have an accuracy of 35 % at 40 ppbv with a precision of $\pm$ 2.5 ppbv (1σ at 30 s time resolution). POM provides an accuracy of 1.5 ppbv and a precision of 1.5 ppbv (1σ at 10 s time resolution) in the observed O_3 mixing ratio range. The feasibility of using these sensors for measurements in the PBL was discussed in Schuldt et al. (2023) and Tillmann et al. (2022). A detailed description of the development, technical characteristics, and calibration of the multicopter system can be found in Bretschneider et al. (2022). The campaign's base was located within the proximity of the A555 highway, which is a much-frequented connection between the German cities of Cologne and Bonn. The measurements were conducted above agricultural land located about 1 km south of the town of Wesseling. The city centres of Cologne and Bonn are about 15 km north and 10 km south of the measurement location, respectively (Fig. 1). The Wesseling region is located within the Rhineland chemical region and is widely recognised as a leading chemical hub in Europe. Wesseling, in particular, hosts a remarkable level of industrial activity attributed to the presence of major companies operating in the chemical and petroleum sectors (source: https://www.chemcologne.de/en/investments/the-rhineland-chemical-region, last access: 21 February 2024).

The objective of this campaign was to capture the early-morning evolution of air pollutant concentrations with the development of the PBL. Furthermore, the proximity to the highway allows for measurements of pollutants specifically originating from traffic sources.

The drone is operated by an autopilot system that uses an inertial navigation solution with an earth-related position based on GNSS (Global Navigation Satellite System) data. During the measurements, the autopilot controls a constant lateral position and a constant vertical climb rate of approximately 1 m s^{-1}. Wind affects only the attitude of the copter, but given the low-wind situations during this campaign, the effect on the attitude can be neglected. The drone reached a maximum altitude of 350 m. This altitude limitation was imposed by air traffic restrictions in the area due to its proximity to the Cologne Bonn Airport. During each drone flight, two profiles were acquired: one ascending profile and one descending profile were done in a short period of time. For the assimilation experiments carried out with EURAD-IM, only the ascending profiles were utilised due to their higher accuracy (Schlerf et al., 2024). The measurements during the descending flights are strongly influenced by the turbulence generated by the drone's propellers, which reduces the data quality. In this study, the vertical profiles of O_3 and NO obtained from the multicopter are utilised and assimilated within EURAD-IM. The vertical resolution of these profiles is approximately 10 m, with 254 data points assimilated on 22 September 2021 and 257 on 23 September 2021 for both O_3 and NO. Additionally, observations from two ground-based stations situated on both sides of high-

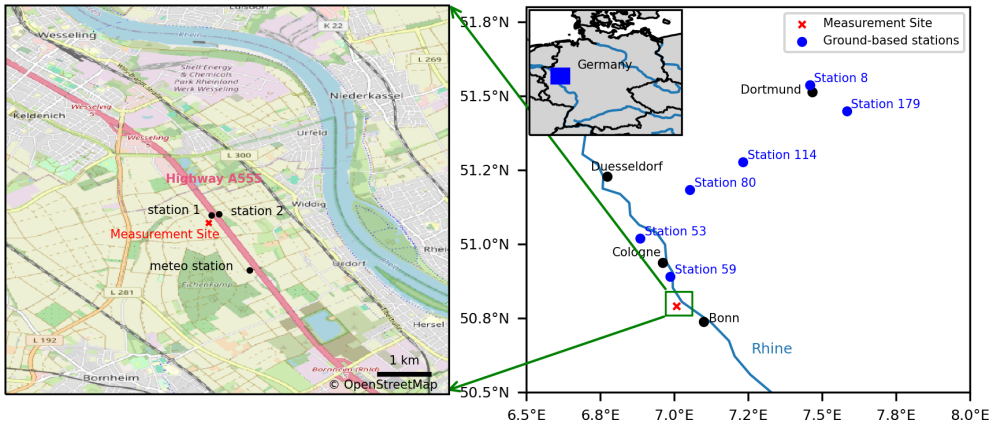

Figure 1. Geographic map displaying the MesSBAR measurement location, air quality ground stations, and meteorological station situated near the A555 highway. (Source: ©OpenStreetMap contributors 2023; distributed under the Open Data Commons Open Database License (ODbL) v1.0.)

way A555 (Fig. 1) are used to validate the simulation results. Furthermore, meteorological observations from an automatic weather station, located approximately 1 km southeast of the measurement site, are employed for comparing meteorological data, especially the wind fields.

3.2 Simulation set-up

The objective of this study is to investigate the impact of O_3 and NO drone profile assimilation on the air quality analysis using high-resolution EURAD-IM simulations. The model grid has a horizontal resolution of 5 km × 5 km and is vertically divided into 30 layers defined by terrain following sigma coordinates between the surface and 100 hPa, with about 19 layers covering the lowest 1 km of the atmosphere. The EURAD-IM domain covers central Europe, including Germany with 271 × 298 grid points. The model output is adjusted to provide forecasts with a temporal resolution of 60 s, allowing for a more precise comparison with the high-resolution drone observations. To assess the impact of drone data assimilation on air quality forecasts, simulations are conducted both with and without data assimilation (Table 2). The joint initial value and emission rate optimisation mode of EURAD-IM is activated for this purpose. Two 24 h experiments are performed without assimilation: one on 22 September 2021 and the other on 23 September 2021. For these experiments, the model is initialised from a climatological chemical state with a spin-up simulation of 6 d (16–21 September 2021) prior to the campaign dates in order to establish a chemically balanced initial state. Moreover, two additional simulations focusing on O_3 and NO data assimilation are performed for 24 h on 22 and 23 September 2021. The assimilation window is deliberately selected to coincide with the availability of observations, aiming to minimise computational time in the simulations while also ensuring a meaningful lead time for emission optimisation. For drone data assimilation, the observation error is considered as the sum of measurement and representativeness errors. The measurement error for O_3 is taken as the standard deviation of the measurements. For NO, the error ϵ_{meas} is estimated according to Elbern et al. (2007) by defining a relative error ϵ_{rel} and a minimal absolute error ϵ_{abs}:

$$\epsilon_{\text{meas}} = \max(\epsilon_{\text{abs}}, \epsilon_{\text{rel}} \cdot y), \tag{2}$$

where y is the individual observation. The absolute error used for NO is 2 ppbv, and the relative error is considered to be 20 % of the observed values.

The representation error is calculated by applying the corresponding formula from Elbern et al. (2007), which considers the grid cell spacing (Δx), the representativeness length of the measurement location (L_{rep}), and an absolute error specific to the measured species. The formula is expressed as

$$\epsilon_{\text{rep}} = \sqrt{\frac{\Delta x}{L_{\text{rep}}}} \times \epsilon_{\text{abs}}. \tag{3}$$

The grid cell spacing (Δx) corresponds to the spatial resolution of the measurement grid, while the representativeness length (L_{rep}) indicates the effective range over which the measurement is considered representative. In this case study, L_{rep} is set to 3 km. The absolute error (ϵ_{abs}) varies by species: it is 2 ppbv for O_3 and 3 ppbv for NO. For the estimation of background errors, horizontal correlation lengths of 2.5, 10, and 20 km are employed at the surface, at the top of the PBL, and at the upper model levels, respectively.

3.3 Evaluation of the wind situation

The wind is a critical parameter that governs the dispersion of air pollutants and their transport, with a direct influence on emission optimisation within the framework of inverse

Table 2. Model simulations presented in this study.

Experiment name	Assimilation	Period	Assimilation window	Assimilated observations
REF_22SEP	No	24 h, 22 September 2021	–	–
REF_23SEP	No	24 h, 23 September 2021	–	–
DA_22SEP	Yes	24 h, 22 September 2021	00:00–11:00 UTC	Six drone profiles of O_3 and NO
DA_23SEP	Yes	24 h, 23 September 2021	00:00–09:00 UTC	Five drone profiles of O_3 and NO

CTMs. The wind conditions at the observation site are evaluated for two purposes: firstly to validate the suitability of the measurement site location for measuring local traffic emissions and secondly to assess the horizontal wind for applications to emission optimisation.

Figure 2a and b show the surface wind speed and direction observed by the nearby weather station during the flights' operation hours. The dominant wind direction is primarily from the southeast on 22 September 2021, with a maximum speed of 1.3 $m\,s^{-1}$, while it comes from the south to southeast in the morning hours of 23 September 2021, with a maximum recorded speed of 2.0 $m\,s^{-1}$. This indicates that the observation point is strategically located downwind of the nearest traffic emission source, which enabled the multicopter to successfully capture the emissions from the highway.

Apart from the surface conditions during the measuring period, each of the 2 d is characterised by a distinct wind situation, as shown in the horizontal wind profiles extracted from the WRF simulations in Fig. 2c and d. On 22 September 2021, the wind patterns exhibit vertical wind shear throughout the day and across all levels, changing direction from the east-southeast at lower altitudes to the west-northwest at higher altitudes. However, the wind intensity remains relatively low, measuring less than 3.0 $m\,s^{-1}$. On 23 September 2021, the surface wind direction aligns with the observations during the campaign period. Nevertheless, at higher levels and beyond the campaign period, westerly and southwesterly winds dominate, and their speed increases with height. The maximum speed of 12.0 $m\,s^{-1}$ is reached at 450 m between 05:00 and 07:00 UTC. The difference in the wind profiles between the 2 d may result in variations in the assimilation results, particularly with respect to emission optimisation.

4 Results

4.1 Impact on vertical profiles

In order to evaluate the impact of the drone data assimilation on the air pollutants' vertical distribution and given the lack of independent vertical profiles, the simulation results are first compared to the drone observations that are assimilated. Figure 3 presents the observed O_3 and NO drone profiles as well as vertical profiles resulting from the 4D-Var assimilation and the reference simulations. For both days, the 4D-Var analyses agree better with the drone observations in comparison to the reference forecast for both species, which indicates the successful assimilation of the drone observations. On 22 September 2021, an underestimation by the reference simulation is observed for the O_3 levels at altitudes above 200 m, with discrepancies reaching up to 15 ppbv, especially for the first three flights (F1, F2, and F3). The assimilation of drone profiles significantly reduces this underestimation. The bias was reduced by 98 % (−4.58 ppbv) for F1, 36 % (−0.74 ppbv) for F2, and 41 % (−1.44 ppbv) for F3, with an average reduction of 30 % (−0.73 ppbv) across all flights (Table 3). On 23 September 2021, the reference model run overestimates O_3 concentrations at both ground and near-surface levels. The most pronounced overestimations occur during the first three flights of the day (F7, F8, and F9), with discrepancies reaching up to 20 ppbv. Following the 4D-Var assimilation, the O_3 bias is reduced by more than 82 % (−12.49 ppbv) for F7, 56 % (−2.86 ppbv) for F8, and 25 % (−0.96 ppbv) for F9. As a result, the overall O_3 bias on the second day is reduced by approximately 55 % (−3.46 ppbv) (Table 3).

On both days, the reference simulations underestimate the NO vertical distribution at all heights, with the strongest discrepancies at ground level. Improvement due to the assimilation is accomplished mostly at surface and near-surface levels for the initial three flights of each day (F1, F2, F3, F7, F8, and F9), with more pronounced adjustments on the second day at ground level, while at higher levels during these same flights, the impact of the assimilation is minimal to non-existent, for instance, for flights F7 and F8 above 150 m. Overall, bias reductions of 24 % (6.78 ppbv), 33 % (11.61 ppbv), and 23 % (8.91 ppbv) were observed for F1, F2, and F3, respectively. On the second day, greater improvements were achieved, with reductions of 30 % (4.17 ppbv) for F7, 49 % (10.1 ppbv) for F8, and 57 % (15.29 ppbv) for F9. Because the pollutant concentrations are well-mixed in the PBL, a uniformly positive impact throughout the vertical can be seen in the NO analyses of the later flights of the day (F4, F5, F6, F10, and F11). The bias is reduced by 38 % (−10.81 ppbv) for F4, 54 % (−15.26 ppbv) for F5, and 49 % (−14.66 ppbv) for F6. On the following day, the bias reduction is smaller, with a 27 % (−7.48 ppbv) reduction for F10 and 18 % (−5.58 ppbv) for F11. Overall, the 4D-Var assimilation of drone observations leads to a substantial reduction in NO biases, with a 36 % reduction (−11.34 ppbv) on the

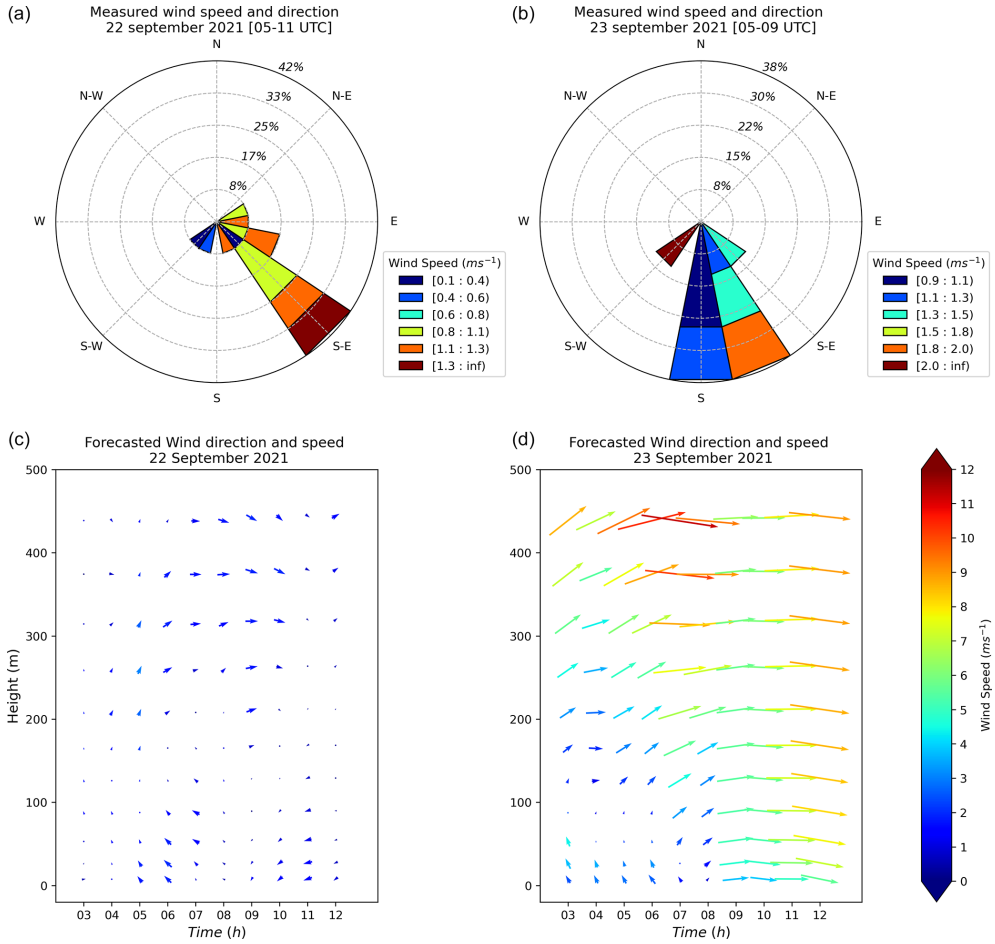

Figure 2. Observed surface wind speed and direction during the measurement period on 22 September 2021 **(a)** and 23 September 2021 **(b)**. Forecast of horizontal wind profiles for different hours for the lowest 500 m at the campaign location on 22 September 2021 **(c)** and 23 September 2021 **(d)**.

first day and a 35 % reduction (−8.52 ppbv) on the second day, between the reference model forecast and observations (Table 3).

These results highlight the successful assimilation of drone observations by the EURAD-IM 4D-Var system. The accuracy of these findings is further examined and discussed in Sect. 4.3 through a validation process using independent observations.

4.2 Emission optimisation

The 4D-Var data assimilation method applied here aims at finding the best representation of the pollutants combining the knowledge provided by the EURAD-IM simulations and the drone O_3 and NO profile observations. The method relies on the assumption that the largest uncertainties in the modelled pollutant concentrations are based on uncertainties in initial values and emission rates. Emission correction factors for 25 anthropogenic pollutants can be deduced from the analysis. Consequently, it is worth looking at the emission factors being analysed to gain a first insight into the potential to retrieve detailed information about emission assessment by applying this inverse modelling technique. However, their generalisation and significance should be carefully evaluated, mainly because of the limited number of drone profiles available, their unequal distribution during the course of the day, the resulting short assimilation windows, and the lack of a long-term statistical analysis.

The assimilation experiments performed with the O_3 and NO drone observations result in significant corrections of NO and NO_2 emission rates in the grids surrounding the observation site. The resulting emissions factors, which represent the ratio between the optimised emission rates and the input emission rates for each species, have variability that ranges from 1 to 4 for NO and from 1 to 6 for NO_2 in the DA_22SEP experiment. In contrast, the variability extends from 1 to 14 for both NO and NO_2 in the DA_23SEP experiment (Fig. A1). This indicates that an increase in emissions is analysed in the studied region. Figure 4 (first row) displays the original daily NO_x emissions rates and the anal-

Table 3. O_3 and NO biases (model value minus observation; in ppbv) for each flight.

Model runs	O_3 vertical profiles						
	F 1	F 2	F 3	F 4	F 5	F 6	Daily absolute bias
REF_22SEP	−4.65	−2.06	−3.53	−1.23	−0.91	−2.49	2.48
DA_22SEP	0.07	−1.32	−2.09	−0.38	−2.42	−4.20	1.75
	F 7	F 8	F 9	F 10	F 11		Daily absolute bias
REF_23SEP	15.20	5.12	3.81	3.64	3.86		6.33
DA_23SEP	2.71	−2.26	−2.85	−3.92	−2.63		2.87
	NO vertical profiles						
	F 1	F 2	F 3	F 4	F 5	F 6	Daily absolute bias
REF_22SEP	−27.96	−35.39	−39.34	−28.21	−28.11	−30.09	31.52
DA_22SEP	−21.18	−23.78	−30.43	−17.40	−12.85	−15.43	20.18
	F 7	F 8	F 9	F 10	F 11		Daily absolute bias
REF_23SEP	−13.95	−20.75	−26.65	−28.03	−30.88		24.05
DA_23SEP	−9.78	−10.65	−11.37	−20.55	−25.30		15.53

ysed emission changes on 22 and 23 September 2021. A significant increase in NO_x emissions is obtained in the DA_22SEP results, with changes in emission rates reaching up to 16 Mg d^{-1} in the grid cells located north and northwest of the observation site. The emission of 16 Mg d^{-1} represents approximately 3.46 % of the total daily NO_x emissions in the analysed region, which is about 462 Mg d^{-1}. For DA_23SEP in contrast, the emission rates increase by up to 10 Mg d^{-1} in the grid cells surrounding the observation site. Based on the chemical coupling with NO and O_3, carbon monoxide (CO), sulfur dioxide (SO_2), and sulfate (SO_4) emissions are optimised, resulting in emission correction factors between 1 and 3 (not shown).

To interpret the results and to investigate this discrepancy between the 2 d, the changes in NO_x emissions are evaluated according to the emission source sectors. Figure 4 additionally shows the original NO_x emissions and the analysed emission changes for three dominant polluter sectors in this region: power production, industry, and road transport. The original emission data set includes in total 12 GNFR (gridded nomenclature for reporting) sectors, while only these three sectors are substantially affected in the analysis. The DA_22SEP results indicate that 75 % of the emissions increase can be attributed to power generation and industrial activities. The remaining emission increase is mainly attributed to the road transportation sector. For the DA_23SEP results, almost half of the analysed emissions come from the road transport sector. In some grid cells, the additional road emissions of DA_23SEP are twice as high as those of DA_22SEP, reaching up to 6 Mg d^{-1} compared to 1.5 Mg d^{-1}, respectively.

The area affected by the emission corrections differs for the two consecutive analysis days. This disparity lies in the different meteorological conditions, particularly in the variation in wind patterns, that occur during these days. As shown in Fig. 2 the prevailing winds in the studied region have low intensity and significant variability at the ground and high altitude on 22 September 2021, while on 23 September, the wind is more intense and predominantly originating from the west. This causes different dispersion situations for the pollutant during the 2 d.

This can be seen in Fig. 5, which shows tropospheric NO_2 columns observed by TROPOMI (Tropospheric Monitoring Instrument) on board the Sentinel-5 Precursor (Sentinel-5P) satellite. These data highlight that the accumulation of pollutants resulting in high NO_2 concentrations is very distinct for each individual day. On 22 September 2021, TROPOMI data show a highly polluted area north and northwest of the observation site, which does not persist on 23 September 2021. This might explain the increase in emissions rates seen in the DA_22SEP results to the north and northwest of the observation site. However, it is unfortunately not possible to directly obtain information about the NO_2 emissions from the TROPOMI data. Nevertheless, the 4D-Var assimilation algorithm seems to react to the high concentrations by attributing corrections to emission increases.

These results indicate the strong effects of the wind condition on the observability of the drone measurement. Nevertheless, it shows the potential that the drone observations have for emission optimisation, especially for emissions that are emitted at higher altitudes, such as power plants and industries. Drawing definitive conclusions regarding the accuracy of emissions changes is consistently challenging, primarily due to the scarcity of emissions observations. Consequently, we will validate the 4D-Var analysis using independent ground-based observations, and we will analyse the

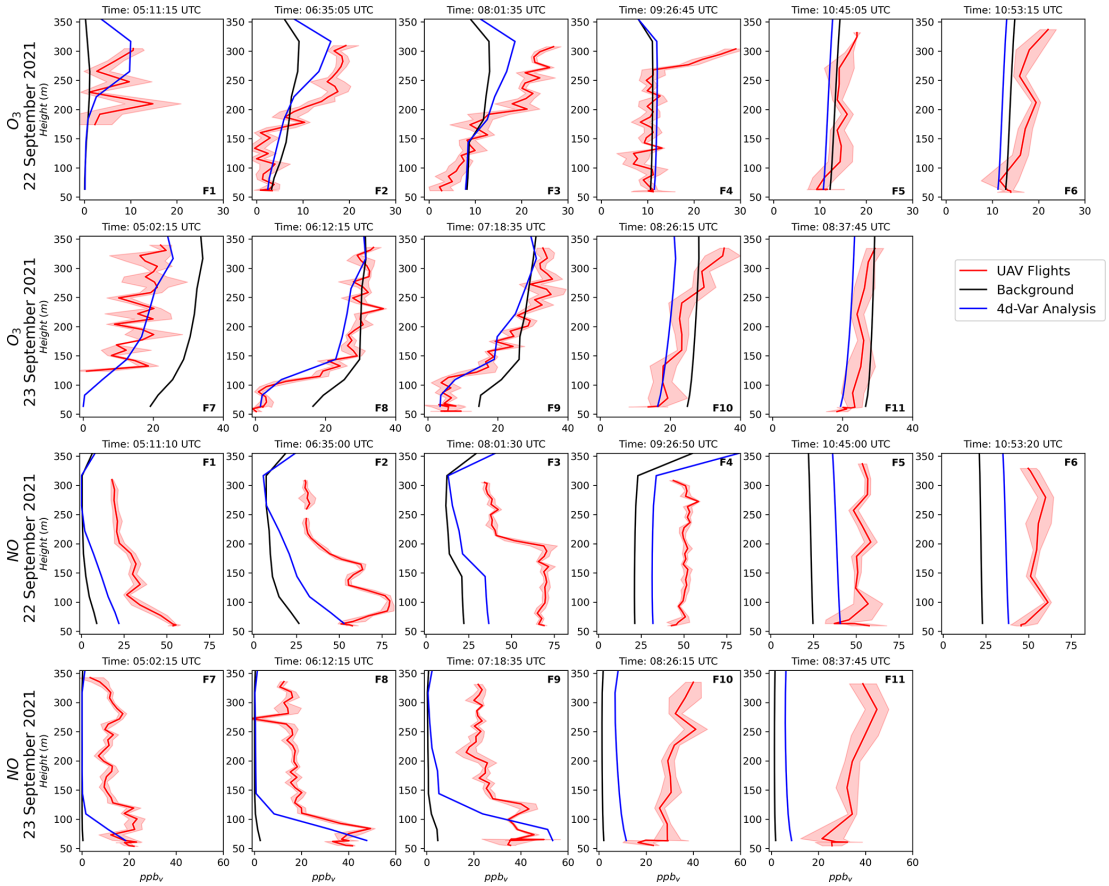

Figure 3. The vertical profiles of O_3 and NO measured by the drone system (red line) and compared to the 4D-Var analysis (blue line) and the reference run (black line) for all flights on 22–23 September 2021. The red shading highlights the standard deviation of the drone observations.

contribution of emission changes to the observed improvements in order to evaluate the potential of drone observations in optimising emission rates.

4.3 Validation against independent observations

4.3.1 Local impact

To validate the impact of the drone data assimilation, we compare the experiment results with independent ground-based observations. Local observations from two monitoring stations located one on each side of the A555 highway but in the same grid cell as the assimilated data (Fig. 1) are used for this evaluation. Figure 6 shows the daily time series of observed O_3, NO, and NO_2 concentrations along with the modelled concentrations from both the reference and assimilation experiments. To evaluate the benefits of the drone data assimilation, the bias, RMSE (root mean square error), and Pearson correlation are examined for all experiments averaged over the assimilation window and over a 24 h period (Table 4) using the means of the observations from the two stations as reference.

The DA_22SEP experiment performance for the O_3 concentrations is almost similar to the reference experiment (REF_22SEP). Following the analysis of Sect. 4.1, this is expected because the a priori forecast and the drone observation for near-ground O_3 concentration agree well during this day. The main improvement during the first day is seen for the NO concentrations within the assimilation window as well as during the subsequent free forecast. The assimilation of drone observations results in a strong reduction in the bias of 87 % ($-20.48\,\mu g\,m^{-3}$) and the RMSE of 20 % ($-7.7\,\mu g\,m^{-3}$), with an amelioration in the Pearson correlation of 0.15 over the 24 h period. The daily NO_2 cycle is impacted by the assimilation due to its chemical coupling with O_3 and NO. Therefore, the assimilation experiment exhibits a better performance during the daytime relative to the reference experiment. However, during the late afternoon and nighttime, REF_22SEP performs better than DA_22SEP, as NO_2 is slightly overestimated. The best performance of the drone data assimilation results is obtained on 23 September 2021. A remarkable improvement in the O_3 concentration is noticed within the initial 7 h of the day, while a deterioration is observed between 16:00 and 24:00 UTC.

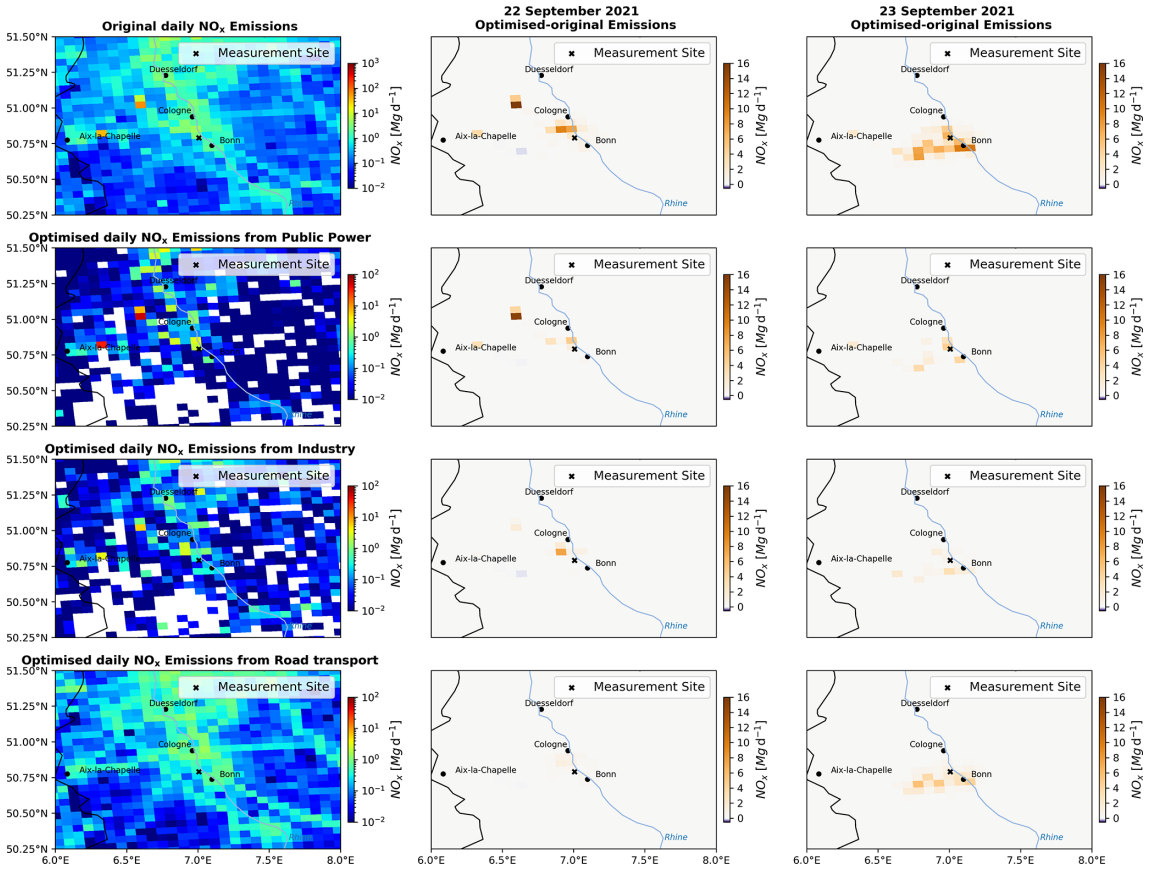

Figure 4. Daily NO_x emissions within the analysed domain (left column) and the analysed NO_x emission changes on 22 September (middle column) and 23 September (right column) 2021. The rows (from top to bottom) display the total NO_x emissions and the emissions from public power production, industry, and road transport.

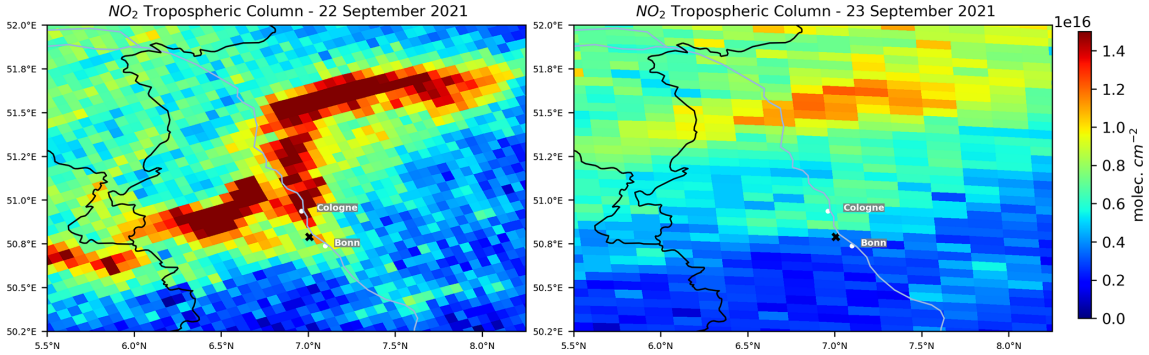

Figure 5. Maps of the TROPOMI NO_2 tropospheric columns (in molec. cm^{-2}) over the studied area on 22 September 2021 at 11:00 UTC (left) and on 23 September 2021 at 12:18 UTC (right). Source: https://browser.dataspace.copernicus.eu/ (last access: 30 May 2024).

The daily bias is reduced by 60 % ($-11.18\,\mu g\,m^{-3}$) and the RMSE by 46 % ($-11.06\,\mu g\,m^{-3}$), which also results in an improvement in the correlation of 0.22 during the assimilation window. An improvement in the assimilation results is achieved for NO concentrations. The assimilation experiment reduces the bias by 53 % ($-13.07\,\mu g\,m^{-3}$) and RMSE by 28 % ($-11.59\,\mu g\,m^{-3}$), with an amelioration in the correlation of 0.5 over the 24 h evaluation period. For NO_2, a notable improvement can be seen in the forecast from DA_23SEP compared to REF_23SEP. Within the assimilation window, the bias reduced by 43 % ($-7.77\,\mu g\,m^{-3}$), the RMSE reduced by 29 % ($-6.68\,\mu g\,m^{-3}$), and the correlation improved by 0.19.

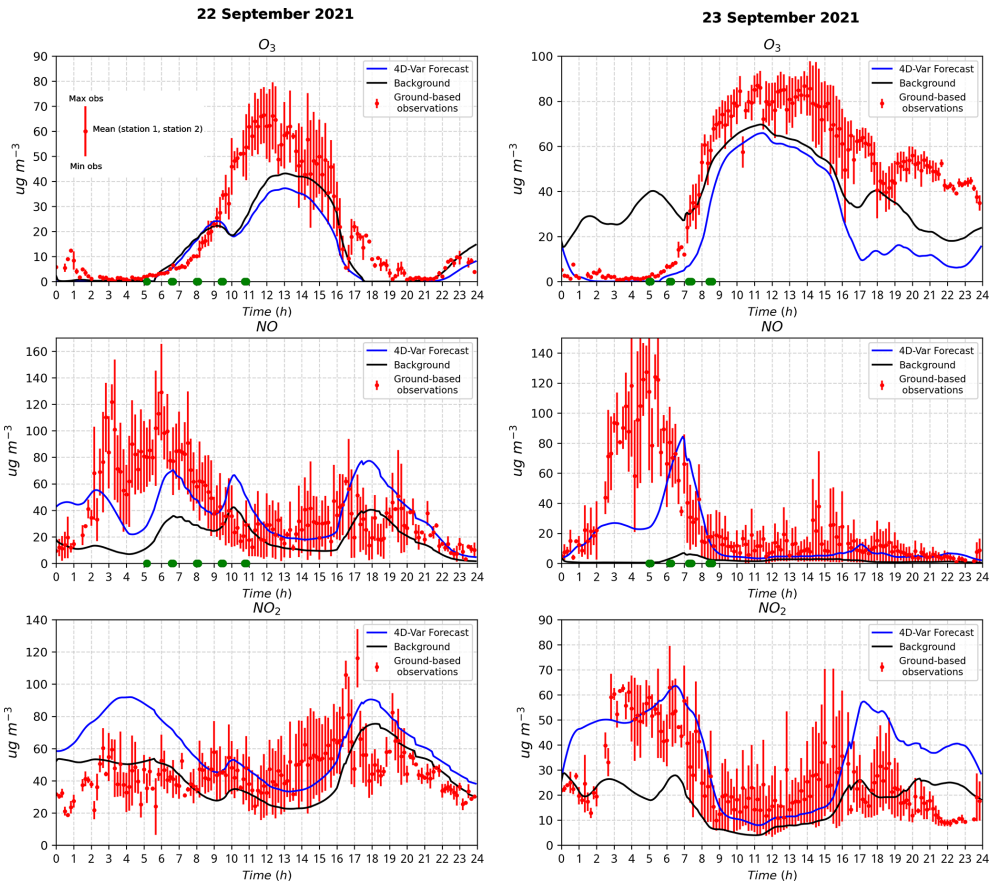

Figure 6. Temporal evolution of the O_3, NO, and NO_2 concentrations as observed by the ground stations (red line) and given by the model in the corresponding grid cell: the reference (black line) and the analysis (blue line) over the 24 h forecast period on 22 and 23 September 2021. Green dots highlight the time of the assimilated drone profiles.

Table 4. Statistical comparison of ground-based observations and model outputs (REF: reference run; DA: assimilation run) for O_3, NO, and NO_2 during the assimilation window and, in parentheses, the 24 h forecast on 22–23 September 2021. The bias and RMSE are in micrograms per cubic metre (µg m^{-3}).

		Statistics	O_3		NO		NO_2	
			REF	DA	REF	DA	REF	DA
22 Sep	2021	Bias	−3.91 (−6.02)	−4.37 (−8.50)	−39.93 (−23.45)	−14.52 (−2.97)	2.97 (−1.40)	27.17 (15.73)
		RMSE	10.52 (11.42)	10.93 (13.73)	53.17 (37.84)	38.44 (30.14)	13.90 (17.66)	32.08 (26.10)
		Correlation	0.83 (0.92)	0.81 (0.92)	−0.14 (0.13)	−0.10 (0.28)	−0.13 (0.20)	0.16 (0.18)
23 Sep	2021	Bias	18.53 (−5.37)	−7.35 (−21.60)	−52.62 (−24.82)	−23.61 (−11.75)	−17.83 (−9.45)	10.06 (8.99)
		RMSE	24.10 (21.91)	13.04 (26.32)	66.16 (41.77)	46.93 (30.18)	22.84 (17.40)	16.16 (18.70)
		Correlation	0.70 (0.71)	0.92 (0.86)	−0.28 (−0.07)	0.22 (0.56)	0.40 (0.28)	0.59 (0.49)

These results indicate that the 4D-Var assimilation of the drone observations has the potential to improve the concentration of O_3, NO, and NO_2 during the early morning and daytime when optimising both the initial values and emissions rates simultaneously. The observed deterioration of the O_3 and NO_2 forecast during the late afternoon and nighttime in the DA_23SEP assimilation run is likely related to the NO_x titration process. During the night, O_3 removal is the dominant process in areas with significant NO emission sources (Sillman, 1999). Taking this into account may indicate that the drone data assimilation provides a higher estimate of NO_2 emissions during the night. Since the assimilation algorithm derives only one emission factor per day, the amplitude of the daily temporal emission profile is adjusted. It is assumed that the temporal emission profile is more certain than the emission strength. Deriving, for exam-

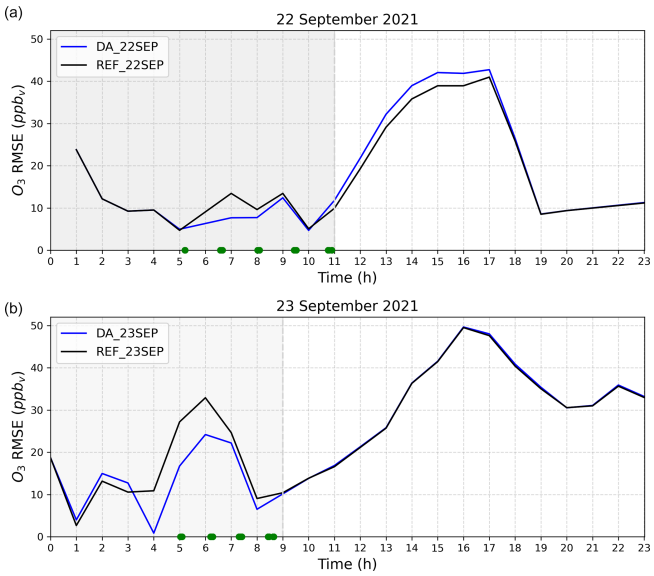

Figure 7. Temporal evolution of the RMSE (model − observations) (in ppbv) for O_3 calculated for the reference (black) and the data assimilation (blue) runs over the 24 h forecast period across all ground stations on 22 September 2021 **(a)** and 23 September 2021 **(b)**. Green dots highlight the time of the assimilated drone profiles.

ple, hourly emission factors instead would allow for more flexible adjustments of the emissions, which would be beneficial for the nowadays strongly regulated emission sources, such as power production (dependent on the availability of renewable energy). Previous studies demonstrated that the temporal distribution of traffic emissions significantly influences nighttime concentrations of NO_2 and O_3 (Menut et al., 2012). As the emission optimisation process maintains the same temporal variability, it is necessary to have 24 h data assimilation to improve the nighttime O_3 and NO_2 forecasts. Moreover, an inaccurately predicted PBL height can lead to uncertainties in the O_3 and NO_2 forecasts. A full analysis of the PBL representation is however beyond the scope of this study.

4.3.2 Regional impact

To further investigate the effect on a larger spatial scale, an additional validation is performed using independent ground-based observations from six different ground-based air quality monitoring stations situated in the vicinity of the observation site (Fig. 1, Table A1). For this validation, only stations that are impacted by the assimilation are selected. These are located at distances ranging from 12 to 85 km from the campaign location. Given the unavailability of NO observations, this validation considers only O_3 and NO_2. Although NO_2 is not assimilated in this study, it is indirectly influenced due to chemical coupling with the observed species and via the optimised NO_x emissions. Figure 7 presents the hourly RMSE time series of O_3 concentrations for the assimilation and reference experiments, averaged over all selected stations. Corresponding results for NO_2 are depicted in Fig. A2. The individual RMSEs of O_3 and NO_2 within the assimilation window for all simulations per station are presented in Table 5.

Figure 7 shows that the O_3 RMSE for DA_22SEP and DA_23SEP is notably lower than that REF_22SEP within the data assimilation window. Outside the assimilation window, only a small added error is noted between 11:00 and 17:00 UTC for DA_22SEP, which appears similar to the results of the local validation, while no impact is observed during the subsequent free-forecast period for DA_23SEP. The largest RMSE reduction of 30 % takes place at Station 59 (−2.26 ppbv) on 22 September and of 40 % (−6.61 ppbv) on 23 September, as well as 35 % at Station 80 (−2.22 ppbv) on 22 September and 34 % (−4.98 ppbv) on 23 September. These stations are situated 12 and 43 km north of the campaign site, respectively. The smallest reductions occur at the stations of furthest distance, namely 5 % at Station 8 (−0.59 ppbv) on 22 September and 4 % (−0.46 ppbv) on 23 September and 2 % at Station 179 (−0.73 ppbv) on 22 September and 7 % (−1.22 ppbv) on 23 September, which are located approximately 85 km northeast of the campaign site. These results suggest that the positive impact of the drone data assimilation is transported to a broader area surrounding the campaign location, resulting in an improvement in O_3 concentrations across a larger area.

For NO_2, a significant RMSE reduction is found at Station 80, with a decrease of 72 % (−7.7 ppbv) for DA_22SEP. However, the RMSEs for Station 59 and Station 53 show an increase within the assimilation window. For DA_23SEP, better results can be seen for all stations except for the rural Station 59. The best reduction of 21 % is achieved at Station 80 (−4.16 ppbv) and 22 % at Station 114 (−2.80 ppbv).

Despite the simplicity of the current assimilation approach, which only incorporates data from a single grid box, a positive effect of assimilation is apparent even for stations situated at greater distances from the drone campaign location. This is attributed to the spatial spread of the analysis increment throughout large areas of the studied region.

4.4 Discussion of the potential and limitations of drone data assimilation

The analysis of the DA_22SEP and DA_23SEP experiments shows that the assimilation of drone observations has a positive impact on the vertical distribution of O_3 and NO and on the daily cycle of O_3 and NO_x at ground level. These promising results underscore the significant potential of drone data assimilation in enhancing regional air quality analysis. Moreover, the assimilation process provides optimised emissions rates for each day. To investigate the role of emission optimisation in the analysis improvement, Table 6 presents the cost reduction for O_3 and NO, as well as the partial costs attributed to the optimisation of the initial

Table 5. The O_3 and NO_2 RMSEs between observation data and model results obtained with (DA) and without (REF) drone data assimilation. The results are shown for every ground-based station for the assimilation window. The RMSE is in parts per billion by volume (ppbv).

RMSE		DA window		DA window	
		REF_22SEP	DA_22SEP	REF_23SEP	DA_23SEP
O_3	Station 8	11.33	10.74	12.17	11.71
	Station 53	10.29	9.66	8.19	7.29
	Station 59	7.75	5.49	16.71	10.10
	Station 80	6.35	4.13	14.58	9.60
	Station 114	25.86	24.39	22.69	19.87
	Station 179	27.96	27.23	17.55	16.33
NO_2	Station 8	18.11	17.49	24.05	22.92
	Station 53	12.85	23.81	10.26	10.77
	Station 59	24.25	44.34	16.88	24.45
	Station 80	10.63	2.93	19.59	15.43
	Station 114	24.14	25.82	12.81	10.01
	Station 179	17.78	18.04	19.85	18.08

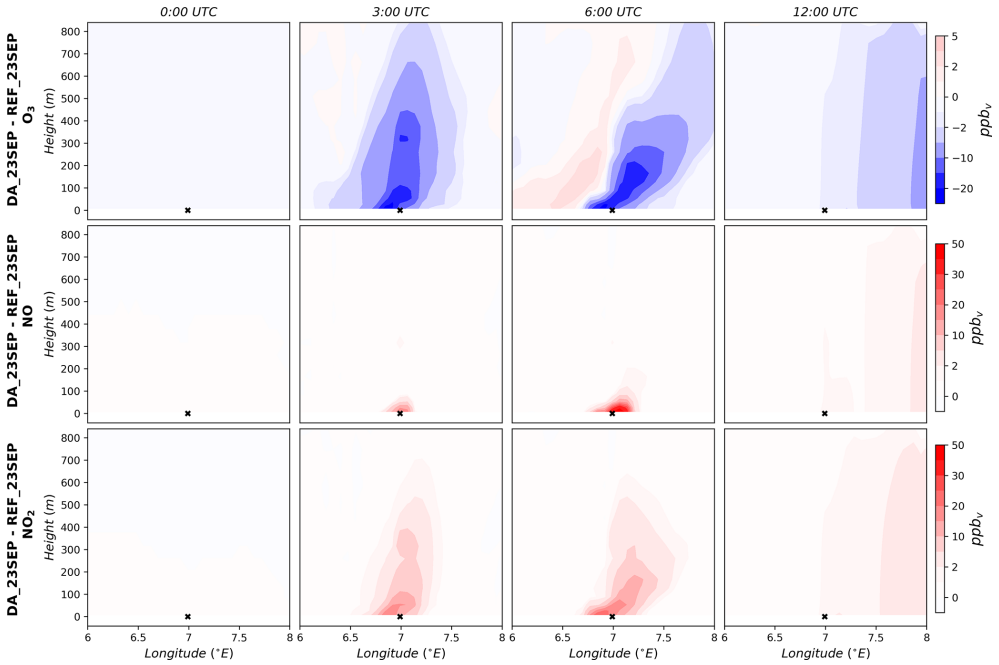

Figure 8. Vertical cross section of the analysis increment of O_3, NO, and NO_2 on 23 September 2021 at selected time steps. The cross section is located along the latitude of the MesSBAR campaign site.

values (IVs) $\left(\frac{\mathcal{J}_b(x_0)}{\mathcal{J}(x_0,e)}\right)$ and the emission correction factors (EFs) $\left(\frac{\mathcal{J}_e(e)}{\mathcal{J}(x_0,e)}\right)$. For both assimilation experiments, the costs are reduced by more than 30 %, which confirms the successful assimilation of the drone profiles. In particular, the O_3 costs of DA_23SEP are highly reduced by 80 %, resulting in a precise alignment between the 4D-Var analysis and the O_3 observations. The partial costs vary between the 2 d. For DA_22SEP, the costs associated with IV are more than twice those of EF, which indicates important IV adjustments and a minimal impact of the emission changes in the cost minimisation. In contrast for DA_23SEP, the effect of optimising the emissions is higher. This indicates that a significant part of the improvement observed in the analysis is due to the optimisation of EF. Therefore, the drone observations may also have significant potential for assessing local emissions. In a recent study by Wu et al. (2022), it was demonstrated that for high-altitude observations, the efficiency of emission rate optimisation is conditioned by favourable wind conditions and strong vertical diffusion.

Despite the observed improvements in the analysis, some limitations are noted. Firstly, the results reported in

Table 6. The percentage of cost reduction achieved for O_3 and NO, as well as the percentage of the partial costs attributed to initial value correction (IV) and emission correction factor (EF) relative to the total cost function.

	Cost reduction		Partial costs	
	O_3	NO	EF	IV
DA_22SEP	34 %	41 %	9 %	25 %
DA_23SEP	80 %	36 %	10 %	4 %

Sect. 4.1 show a limited impact on the NO vertical profiles on 23 September 2021. Although effective correction is achieved at the ground and near-ground levels, limited improvements are obtained for the NO concentrations at higher altitudes (above 150 m) for the first three profiles of the day. Figure 8 illustrates the vertically resolved analysis increment (4D-Var analysis – reference run) for O_3, NO, and NO_2 on 23 September 2021. A negative O_3 increment alongside a positive NO_2 increment is noted, both exhibiting a well-developed vertical spread. The NO increment is constrained near ground level during the early hours of the day. The reason behind this is the NO_x titration process, where freshly emitted NO, including additional NO emissions resulting from emission optimisation, reacts with O_3 to produce NO_2. To achieve better results, a larger NO increment is needed. However, the NO observations from the drone exhibit high measurement errors compared to the background errors, which limits the effectiveness of assimilating these data.

Secondly, some suboptimal outcomes are observed in the free run, namely for O_3 and NO_2 ground concentrations, suggesting that the advantage of the drone data assimilation is limited to the assimilation window (Figs. 6, A3, and A4). Nevertheless, this result is not surprising and is completely explainable. Initially, it is important to note that the reference model simulation already provides underestimations of O_3 peaks during the afternoon and nighttime, which may be linked to uncertainties in the boundary layer height at night, vertical diffusion, and/or emission profiles. Through the 4D-Var assimilation of drone data, adjustments are made to the NO_x emissions. However, in regions characterised by high NO_x emissions, O_3 formation exhibits reduced sensitivity to NO_x emissions but increased sensitivity to VOCs (Visser et al., 2019; Sillman, 1999). Thus, the inability to adjust O_3 concentrations and, consequently, NO_2 in our simulations is not a limitation specific to drone data assimilation.

5 Conclusion

In this study, drone profile measurements of O_3 and NO are assimilated using the 4D-Var data assimilation system of EURAD-IM. This represents the first application of drone data assimilation within a CTM. The primary objective is to assess the ability of drone observations to improve regional air quality analysis when the joint initial value and emission correction factor optimisation approach is applied. The research is conducted using data collected during the 2 d MesSBAR campaign in 2021. To evaluate the results, a comparison is made with ground-based observations obtained at stations very close to the drone flight base location. Moreover, regional validation is conducted using ground-based data from the European air quality monitoring network.

The 4D-Var assimilation of drone data has a positive impact on the representation of these pollutants in the PBL. First, significant improvements are noted in the O_3 and NO vertical profiles, with biases decreasing by 30 % and 55 %, respectively, on the first day and by 35 % on the second day for both species. Moreover, there is a noticeable impact on ground concentrations in the analysis. In the studied grid cell, biases are reduced by up to 60 % for O_3, 55 % for NO, and 43 % for NO_2 ground concentrations within the assimilation window. Furthermore, due to the pollution transport and the connected information propagation in the 4D-Var algorithm, a positive impact is seen in the ground concentrations of O_3 and NO_2 in locations farther from the measurement site. This study also identifies the assessment of emission correction factors as one component of the analysis improvements which underline the potential of the drone observations to be beneficial for emission optimisation.

There are some limitations to this study. Firstly, due to constraints in data availability, the study is restricted to assimilating drone data within a singular grid cell column. Therefore, it would be advantageous to include multiple measurement points distributed across the region, strategically positioned both upwind and downwind of emission sources. Another limitation of this study is the assimilation of data available only during a partial time window of the day. The inclusion of a more extensive observational data set covering longer periods, ideally over 24 h to enable an extended assimilation window, would greatly enhance the optimisation of emission rates.

In conclusion, the 4D-Var assimilation of drone data within the regional air quality model EURAD-IM yields promising results by improving the vertical distribution of pollutants and correcting ground concentrations. From a future perspective, a valuable extension of this work will be to conduct observing system simulation experiments (OSSEs) to evaluate the added value of integrating drone-based observations into the air quality forecasting system in comparison to conventional observations such as ground-based measurements and satellite data.

Appendix A

Table A1. Information about the ground-based monitoring stations.

Station number	Station code	Station name	Distance from campaign site	Station type	Latitude (°N)	Longitude (°E)	Altitude
8	DENW008	Dortmund-Eving	86.5 km	Suburban	51.5369	7.4575	75 m
53	DENW053	Köln-Chorweiler	28.2 km	Suburban	51.0193	6.8846	45 m
59	DENW059	Köln-Rodenkirchen	12.1 km	Rural	50.8898	6.9852	45 m
80	DENW080	Solingen-Wald	43.2 km	Rural	51.1838	7.0526	207 m
114	DENW114	Wuppertal-Langerfeld	56.8 km	Suburban	51.2776	7.2319	186 m
179	DENW179	Schwerte	82.4 km	Suburban	51.4488	7.5823	157 m

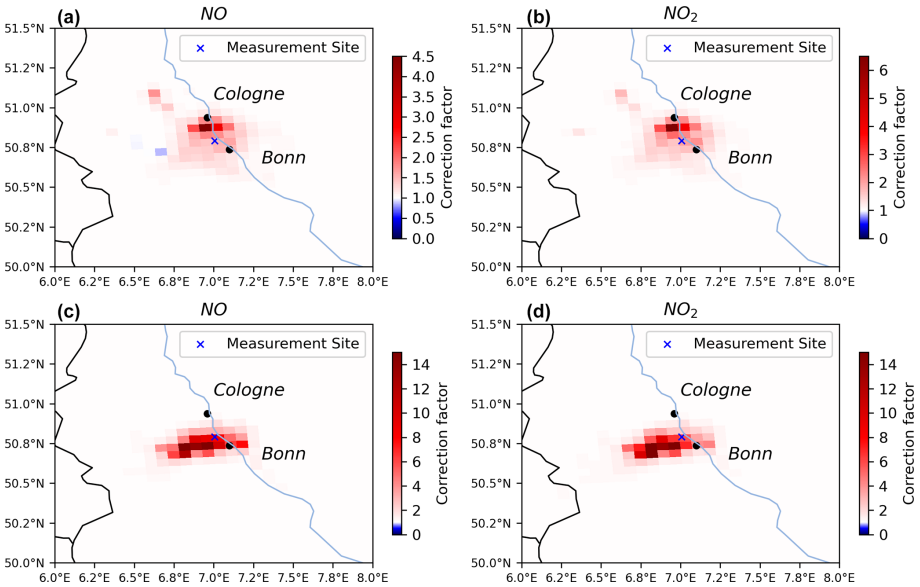

Figure A1. Emission correction factors of NO and NO_2 resulting from the conducted assimilation experiments on 22 September 2021 (**a** and **b**) and 23 September 2021 (**c** and **d**).

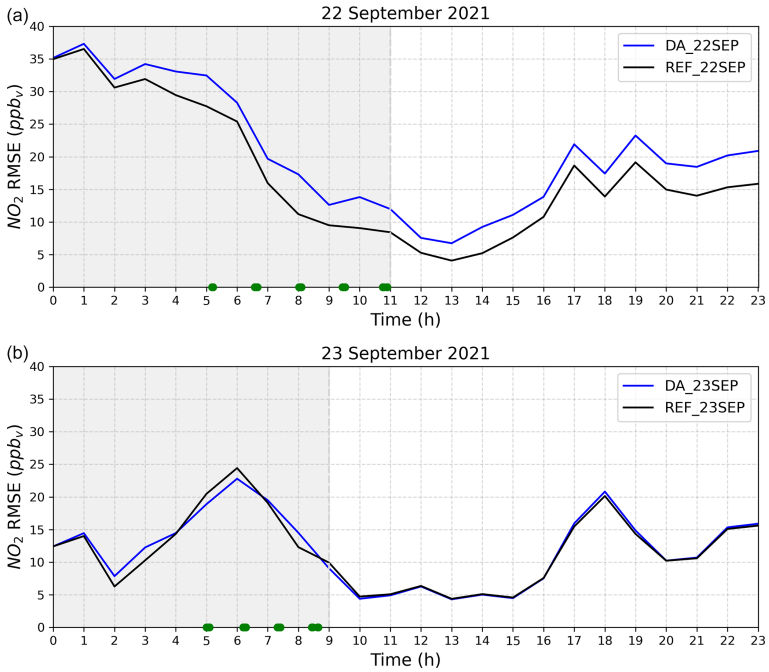

Figure A2. Temporal evolution of the RMSE (model − observations) in parts per billion by volume (ppbv) for NO_2 calculated for the reference (black) and the analysis (blue) over the 24 h forecast period across all ground stations on 22 September 2021 **(a)** and 23 September 2021 **(b)**. Green dots highlight the time of the assimilated drone profiles. The grey shade illustrates the length of the assimilation window.

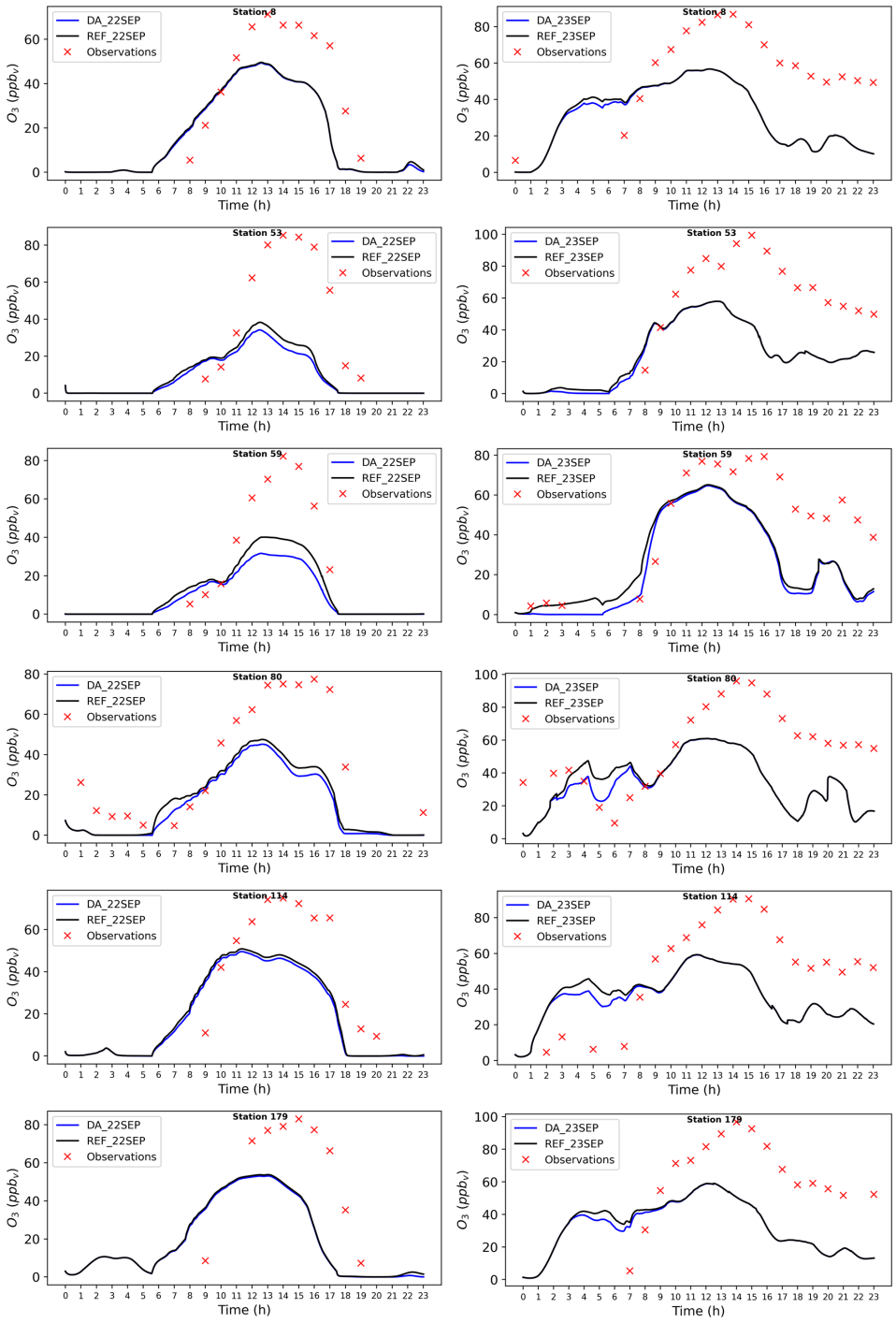

Figure A3. Time series of O_3 concentrations in parts per billion by volume (ppbv) as measured by ground-based stations and predicted by the model. The left panels show data from 22 September 2021, while the right panels display data from 23 September 2021.

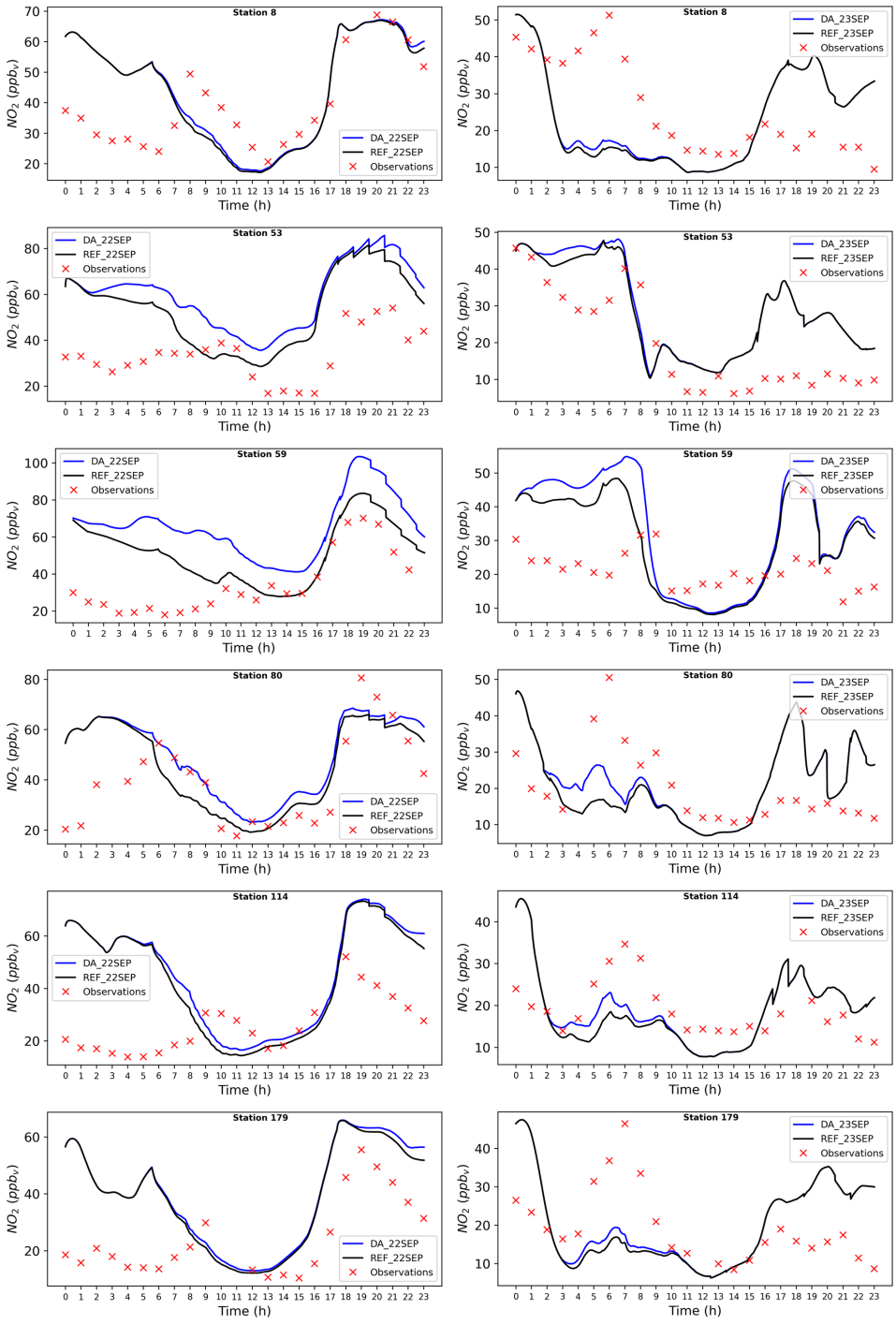

Figure A4. Same as Fig. A3 but for NO_2.

Data availability. The drone data from the MesSBAR campaign used in this study are publicly available from Schlerf et al. (2024) on PANGAEA at the following DOI: https://doi.org/10.1594/PANGAEA.971503.

Author contributions. HE and ACL designed the study. HE conducted the simulations and performed the analyses under the scientific supervision of ACL, PF, and AW. TS and RT provided the observational profile data. The manuscript was prepared by HE with the help of all co-authors. All authors reviewed the manuscript.

Competing interests. The contact author has declared that none of the authors has any competing interests.

Disclaimer. Publisher's note: Copernicus Publications remains neutral with regard to jurisdictional claims made in the text, published maps, institutional affiliations, or any other geographical representation in this paper. While Copernicus Publications makes every effort to include appropriate place names, the final responsibility lies with the authors.

Acknowledgements. The authors gratefully acknowledge all the MesSBAR project partners for their valuable efforts in conducting the campaign and processing the data used in this work. We also thank the Federal Highway Research Institute (BASt) for providing the ground-based observations and meteorological data. We would like to extend our gratitude to the Copernicus Atmosphere Monitoring Service (CAMS) for providing the ground station observation data. The authors also gratefully acknowledge the computing time granted through JARA on the supercomputer JURECA (Jülich Supercomputing Centre, 2021) at Forschungszentrum Jülich.

Financial support. This research has been supported by the Bundesministerium für Verkehr und Digitale Infrastruktur (mFUND grant no. 19F2097C).

The article processing charges for this open-access publication were covered by the Forschungszentrum Jülich.

Review statement. This paper was edited by Kelvin Bates and reviewed by four anonymous referees.

References

Ackermann, I. J., Hass, H., Memmesheimer, M., Ebel, A., Binkowski, F. S., and Shankar, U.: Modal aerosol dynamics model for Europe: development and first applications, Atmos. Environ., 32, 2981–2999, https://doi.org/10.1016/S1352-2310(98)00006-5, 1998.

Altstädter, B., Platis, A., Wehner, B., Scholtz, A., Wildmann, N., Hermann, M., Käthner, R., Baars, H., Bange, J., and Lampert, A.: ALADINA - an unmanned research aircraft for observing vertical and horizontal distributions of ultrafine particles within the atmospheric boundary layer, Atmos. Meas. Tech., 8, 1627–1639, https://doi.org/10.5194/amt-8-1627-2015, 2015.

Bretschneider, L., Schlerf, A., Baum, A., Bohlius, H., Buchholz, M., Düsing, S., Ebert, V., Erraji, H., Frost, P., Käthner, R., Krüger, T., Lange, A. C., Langner, M., Nowak, A., Pätzold, F., Rüdiger, J., Saturno, J., Scholz, H., Schuldt, T., Seldschopf, R., Sobotta, A., Tillmann, R., Wehner, B., Wesolek, C., Wolf, K., and Lampert, A.: MesSBAR-Multicopter and Instrumentation for Air Quality Research, Atmosphere, 13, 629, https://doi.org/10.3390/atmos13040629, 2022.

Corrigan, C. E., Roberts, G. C., Ramana, M. V., Kim, D., and Ramanathan, V.: Capturing vertical profiles of aerosols and black carbon over the Indian Ocean using autonomous unmanned aerial vehicles, Atmos. Chem. Phys., 8, 737–747, https://doi.org/10.5194/acp-8-737-2008, 2008.

De Mazière, M., Thompson, A. M., Kurylo, M. J., Wild, J. D., Bernhard, G., Blumenstock, T., Braathen, G. O., Hannigan, J. W., Lambert, J.-C., Leblanc, T., McGee, T. J., Nedoluha, G., Petropavlovskikh, I., Seckmeyer, G., Simon, P. C., Steinbrecht, W., and Strahan, S. E.: The Network for the Detection of Atmospheric Composition Change (NDACC): history, status and perspectives, Atmos. Chem. Phys., 18, 4935–4964, https://doi.org/10.5194/acp-18-4935-2018, 2018.

Deroubaix, A., Hoelzemann, J. J., Ynoue, R. Y., de Almeida Albuquerque, T. T., Alves, R. C., de Fatima Andrade, M., ao, W. L. A., Bouarar, I., de Souza Fernandes Duarte, E., Elbern, H., Franke, P., Lange, A. C., Lichtig, P., Lugon, L., Martins, L. D., de Arruda Moreira, G., Pedruzzi, R., Rosario, N., and Brasseur, G.: Intercomparison of Air Quality Models in a Megacity: Toward an Operational Ensemble Forecasting System for São Paulo, J. Geophys. Res.-Atmos., 129, e2022JD038179, https://doi.org/10.1029/2022JD038179, 2024.

Diaz, J., Corrales, E., Madrigal, Y., Pieri, D., Bland, G., Miles, T., and Fladeland, M.: Volcano Monitoring with small Unmanned Aerial Systems, American Institute of Aeronautics and Astronautics, ISBN 978-1-60086-939-6, https://doi.org/10.2514/6.2012-2522, 2012.

Duarte, E. D. S. F., Franke, P., Lange, A. C., Friese, E., da Silva Lopes, F. J., ao da Silva, J. J., dos Reis, J. S., Landulfo, E., e Silva, C. M. S., Elbern, H., and Hoelzemann, J. J.: Evaluation of atmospheric aerosols in the metropolitan area of São Paulo simulated by the regional EURAD-IM model on high-resolution, Atmos. Pollut. Res., 12, 451–469, https://doi.org/10.1016/j.apr.2020.12.006, 2021.

Elbern, H. and Schmidt, H.: Ozone episode analysis by four-dimensional variational chemistry data assimilation, J. Geophys. Res.-Atmos., 106, 3569–3590, https://doi.org/10.1029/2000JD900448, 2001.

Elbern, H., Strunk, A., Schmidt, H., and Talagrand, O.: Emission rate and chemical state estimation by 4-dimensional variational inversion, Atmos. Chem. Phys, 7, 3749–3769, https://doi.org/10.5194/acp-7-3749-2007, 2007.

Flagg, D. D., Doyle, J. D., Holt, T. R., Tyndall, D. P., Amerault, C. M., Geiszler, D., Haack, T., Moskaitis, J. R., Nachamkin, J., and Eleuterio, D. P.: On the Impact of Unmanned Aerial System Observations on Numerical Weather Pre-

diction in the Coastal Zone, Mon. Weather Rev., 146, 599–622, https://doi.org/10.1175/MWR-D-17-0028.1, 2018.

Franke, P., Lange, A. C., and Elbern, H.: Particle-filter-based volcanic ash emission inversion applied to a hypothetical sub-Plinian Eyjafjallajökull eruption using the Ensemble for Stochastic Integration of Atmospheric Simulations (ESIAS-chem) version 1.0, Geosci. Model Dev., 15, 1037–1060, https://doi.org/10.5194/gmd-15-1037-2022, 2022.

Franke, P., Lange, A. C., Steffens, B., Pozzer, A., Wahner, A., and Kiendler-Scharr, A.: European air quality in view of the WHO 2021 guideline levels: Effect of emission reductions on air pollution exposure, Elem. Sci. Anth., 12, 00127, https://doi.org/10.1525/elementa.2023.00127, 2024.

Gama, C., Ribeiro, I., Lange, A. C., Vogel, A., Ascenso, A., Seixas, V., Elbern, H., Borrego, C., Friese, E., and Monteiro, A.: Performance assessment of CHIMERE and EURAD-IM' dust modules, Atmos. Pollut. Res., 10, 1336–1346, https://doi.org/10.1016/j.apr.2019.03.005, 2019.

García, O. E., Schneider, M., Sepúlveda, E., Hase, F., Blumenstock, T., Cuevas, E., Ramos, R., Gross, J., Barthlott, S., Röhling, A. N., Sanromá, E., González, Y., Gómez-Peláez, Á. J., Navarro-Comas, M., Puentedura, O., Yela, M., Redondas, A., Carreño, V., León-Luis, S. F., Reyes, E., García, R. D., Rivas, P. P., Romero-Campos, P. M., Torres, C., Prats, N., Hernández, M., and López, C.: Twenty years of ground-based NDACC FTIR spectrometry at Izaña Observatory – overview and long-term comparison to other techniques, Atmos. Chem. Phys., 21, 15519–15554, https://doi.org/10.5194/acp-21-15519-2021, 2021.

Guenther, A. B., Jiang, X., Heald, C. L., Sakulyanontvittaya, T., Duhl, T., Emmons, L. K., and Wang, X.: The Model of Emissions of Gases and Aerosols from Nature version 2.1 (MEGAN2.1): an extended and updated framework for modeling biogenic emissions, Geosci. Model Dev., 5, 1471–1492, https://doi.org/10.5194/gmd-5-1471-2012, 2012.

Illingworth, S., Allen, G., Percival, C., Hollingsworth, P., Gallagher, M., Ricketts, H., Hayes, H., Ładosz, P., Crawley, D., and Roberts, G.: Measurement of boundary layer ozone concentrations on-board a Skywalker unmanned aerial vehicle, Atmos. Sci. Lett., 15, 252–258, https://doi.org/10.1002/asl2.496, 2014.

Jensen, A. A., Pinto, J. O., Bailey, S. C. C., Sobash, R. A., de Boer, G., Houston, A. L., Chilson, P. B., Bell, T., Romine, G., Smith, S. W., Lawrence, D. A., Dixon, C., Lundquist, J. K., Jacob, J. D., Elston, J., Waugh, S., and Steiner, M.: Assimilation of a Coordinated Fleet of Uncrewed Aircraft System Observations in Complex Terrain: EnKF System Design and Preliminary Assessment, Mon. Weather Rev., 149, 1459–1480, https://doi.org/10.1175/MWR-D-20-0359.1, 2021.

Jonassen, M. O., Ólafsson, H., Ágústsson, H., Ólafur Rögnvaldsson, and Reuder, J.: Improving High-Resolution Numerical Weather Simulations by Assimilating Data from an Unmanned Aerial System, Mon. Weather Rev., 140, 3734–3756, https://doi.org/10.1175/MWR-D-11-00344.1, 2012.

Jülich Supercomputing Centre: JURECA: Data Centric and Booster Modules implementing the Modular Supercomputing Architecture at Jülich Supercomputing Centre, J. Large-Scale Res. Facil. JLSRF, 7, A182, https://doi.org/10.17815/jlsrf-7-182, 2021.

Klonecki, A., Pommier, M., Clerbaux, C., Ancellet, G., Cammas, J.-P., Coheur, P.-F., Cozic, A., Diskin, G. S., Hadji-Lazaro, J., Hauglustaine, D. A., Hurtmans, D., Khattatov, B., Lamarque, J.-F., Law, K. S., Nedelec, P., Paris, J.-D., Podolske, J. R., Prunet, P., Schlager, H., Szopa, S., and Turquety, S.: Assimilation of IASI satellite CO fields into a global chemistry transport model for validation against aircraft measurements, Atmos. Chem. Phys., 12, 4493–4512, https://doi.org/10.5194/acp-12-4493-2012, 2012.

Kuenen, J. J. P., Visschedijk, A. J. H., Jozwicka, M., and Denier van der Gon, H. A. C.: TNO-MACC_II emission inventory; a multi-year (2003–2009) consistent high-resolution European emission inventory for air quality modelling, Atmos. Chem. Phys., 14, 10963–10976, https://doi.org/10.5194/acp-14-10963-2014, 2014.

Lampert, A., Altstädter, B., Bärfuss, K., Bretschneider, L., Sandgaard, J., Michaelis, J., Lobitz, L., Asmussen, M., Damm, E., Käthner, R., Krüger, T., Lüpkes, C., Nowak, S., Peuker, A., Rausch, T., Reiser, F., Scholtz, A., Zakharov, D. S., Gaus, D., Bansmer, S., Wehner, B., and Pätzold, F.: Unmanned Aerial Systems for Investigating the Polar Atmospheric Boundary Layer – Technical Challenges and Examples of Applications, Atmosphere, 11, 416, https://doi.org/10.3390/atmos11040416, 2020.

Lawrence, D. A. and Balsley, B. B.: High-Resolution Atmospheric Sensing of Multiple Atmospheric Variables Using the Data-Hawk Small Airborne Measurement System, J. Atmos. Ocean. Technol., 30, 2352–2366, https://doi.org/10.1175/JTECH-D-12-00089.1, 2013.

Leuenberger, D., Haefele, A., Omanovic, N., Fengler, M., Martucci, G., Calpini, B., Fuhrer, O., and Rossa, A.: Improving High-Impact Numerical Weather Prediction with Lidar and Drone Observations, B. Am. Meteorol. Soc., 101, E1036–E1051, https://doi.org/10.1175/BAMS-D-19-0119.1, 2020.

Liu, D. C. and Nocedal, J.: On the limited memory BFGS method for large scale optimization, Math. Program., 45, 503–528, https://doi.org/10.1007/BF01589116, 1989.

Liu, X., Mizzi, A. P., Anderson, J. L., Fung, I. Y., and Cohen, R. C.: Assimilation of satellite NO_2 observations at high spatial resolution using OSSEs, Atmos. Chem. Phys., 17, 7067–7081, https://doi.org/10.5194/acp-17-7067-2017, 2017.

Marécal, V., Peuch, V.-H., Andersson, C., Andersson, S., Arteta, J., Beekmann, M., Benedictow, A., Bergström, R., Bessagnet, B., Cansado, A., Chéroux, F., Colette, A., Coman, A., Curier, R. L., Denier van der Gon, H. A. C., Drouin, A., Elbern, H., Emili, E., Engelen, R. J., Eskes, H. J., Foret, G., Friese, E., Gauss, M., Giannaros, C., Guth, J., Joly, M., Jaumouillé, E., Josse, B., Kadygrov, N., Kaiser, J. W., Krajsek, K., Kuenen, J., Kumar, U., Liora, N., Lopez, E., Malherbe, L., Martinez, I., Melas, D., Meleux, F., Menut, L., Moinat, P., Morales, T., Parmentier, J., Piacentini, A., Plu, M., Poupkou, A., Queguiner, S., Robertson, L., Rouïl, L., Schaap, M., Segers, A., Sofiev, M., Tarasson, L., Thomas, M., Timmermans, R., Valdebenito, A., van Velthoven, P., van Versendaal, R., Vira, J., and Ung, A.: A regional air quality forecasting system over Europe: the MACC-II daily ensemble production, Geosci. Model Dev., 8, 2777–2813, https://doi.org/10.5194/gmd-8-2777-2015, 2015.

Martin, R. V.: Satellite remote sensing of surface air quality, Atmos. Environ., 42, 7823–7843, https://doi.org/10.1016/j.atmosenv.2008.07.018, 2008.

Memmesheimer, M., H. Hass, J. Tippke, and A. Ebel: Modeling of episodic emission data for Europe with the EURAD Emission Model EEM, in: the International Speciality Conference "Re-

gional Photochemical Measurement and modeling studies", San Diego, CA, USA, 101 pp., Vol. 2, edited by: Ranzieri, A. and Solomon, P., 495–499 pp., Air and Waste Management Association, 1995.

Menut, L., Goussebaile, A., Bessagnet, B., Khvorostiyanov, D., and Ung, A.: Impact of realistic hourly emissions profiles on air pollutants concentrations modelled with CHIMERE, Atmos. Environ., 49, 233–244, https://doi.org/10.1016/j.atmosenv.2011.11.057, 2012.

Nathan, B. J., Golston, L. M., O'Brien, A. S., Ross, K., Harrison, W. A., Tao, L., Lary, D. J., Johnson, D. R., Covington, A. N., Clark, N. N., and Zondlo, M. A.: Near-Field Characterization of Methane Emission Variability from a Compressor Station Using a Model Aircraft, Environ. Sci. Technol., 49, 7896–7903, https://doi.org/10.1021/acs.est.5b00705, 2015.

O'Sullivan, D., Taylor, S., Elston, J., Baker, C. B., Hotz, D., Marshall, C., Jacob, J., Barfuss, K., Piguet, B., Roberts, G., Omanovic, N., Fengler, M., Jensen, A. A., Steiner, M., and Houston, A. L.: The Status and Future of Small Uncrewed Aircraft Systems (UAS) in Operational Meteorology, B. Am. Meteorol. Soc., 102, E2121–E2136, https://doi.org/10.1175/BAMS-D-20-0138.1, 2021.

Paschalidi, Z.: Inverse Modelling for Tropospheric Chemical State Estimation by 4-Dimensional Variational Data Assimilation from Routinely and Campaign Platforms, Ph.D. thesis, University of Cologne, 101 pp., https://kups.ub.uni-koeln.de/6588/ (last access: 27 November 2024), 2015.

Petetin, H., Jeoffrion, M., Sauvage, B., Athier, G., Blot, R., Boulanger, D., Clark, H., Cousin, J.-M., Gheusi, F., Nedelec, P., Steinbacher, M., and Thouret, V.: Representativeness of the IAGOS airborne measurements in the lower troposphere, Elementa-Sci. Anthrop., 6, 23, https://doi.org/10.1525/elementa.280, 2018.

Rabitz, H. and Aliş, O. F.: General foundations of high-dimensional model representations, J. Math. Chem., 25, 197–233, https://doi.org/10.1023/A:1019188517934, 1999.

Roberts, G. C., Ramana, M. V., Corrigan, C., Kim, D., and Ramanathan, V.: Simultaneous observations of aerosol-cloud-albedo interactions with three stacked unmanned aerial vehicles, P. Natl. Acad. Sci. USA, 105, 7370–7375, https://doi.org/10.1073/pnas.0710308105, 2008.

Roselle, S. and Binkowski, F.: Cloud Dynamics and Chemistry, in Science Algorithms of the EPA Models-3 Community Multiscale Air Quality (CMAQ) Modeling System, Research Triangle Park, EPA 600/R-99-030, https://www.cmascenter.org/cmaq/science_documentation/pdf/ch11.pdf (last access: 27 November 2024), 1999.

Sandu, A. and Sander, R.: Technical note: Simulating chemical systems in Fortran90 and Matlab with the Kinetic PreProcessor KPP-2.1, Atmos. Chem. Phys, 6, 187–195, https://doi.org/10.5194/acp-6-187-2006, 2006.

Scheffe, R., Philbrick, R., on Macdonald, C., Dye, T., Gilroy, M., and Carlton, A.-M.: Observational Needs for Four-dimensional Air Quality Characterization, https://cfpub.epa.gov/si/si_public_record_report.cfm?Lab=NERL&dirEntryId=213564 (last access: 27 November 2024), 2009.

Schell, B., Ackermann, I. J., Hass, H., Binkowski, F. S., and Ebel, A.: Modeling the formation of secondary organic aerosol within a comprehensive air quality model system, J. Geophys. Res.-Atmos., 106, 28275–28293, https://doi.org/10.1029/2001JD000384, 2001.

Schlerf, A., Bretschneider, L., Schuchard, M., Düsing, S., Käthner, R., Wehner, B., Schuldt, T., Wesolek, C., Tillmann, R., Lange, A. C., Erraji, H., Krüger, T., Scholz, H., Frost, P., Sobotta, A., Baum, A., Ebert, V., Bohlius, H., Nowak, A., Langner, M., and Lampert, A.: Validation and optimization of the drone air quality measurement system MesSBAR, Pangaea [data set], https://doi.org/10.1594/PANGAEA.971503, 2024.

Schuldt, T., Gkatzelis, G. I., Wesolek, C., Rohrer, F., Winter, B., Kuhlbusch, T. A. J., Kiendler-Scharr, A., and Tillmann, R.: Electrochemical sensors on board a Zeppelin NT: in-flight evaluation of low-cost trace gas measurements, Atmos. Meas. Tech., 16, 373–386, https://doi.org/10.5194/amt-16-373-2023, 2023.

Schuyler, T. and Guzman, M.: Unmanned Aerial Systems for Monitoring Trace Tropospheric Gases, Atmosphere, 8, 206, https://doi.org/10.3390/atmos8100206, 2017.

Sillman, S.: The relation between ozone, NO_x and hydrocarbons in urban and polluted rural environments, Atmos. Environ., 33, 1821–1845, https://doi.org/10.1016/S1352-2310(98)00345-8, 1999.

Skamarock, W. C., Klemp, J. B., Dudhia, J., Gill, D. O., Barker, D. M., Duda, M. G., Huang, X.-Y., Wang, W., and Powers, J. G.: A Description of the Advanced Research WRF Version 3, https://doi.org/10.5065/D68S4MVH, 2008.

Stockwell, W. R., Kirchner, F., Kuhn, M., and Seefeld, S.: A new mechanism for regional atmospheric chemistry modeling, J. Geophys. Res., 102, 847–872, https://doi.org/10.1029/97JD00849, 1997.

Sun, Q., Vihma, T., Jonassen, M. O., and Zhang, Z.: Impact of Assimilation of Radiosonde and UAV Observations from the Southern Ocean in the Polar WRF Model, Adv. Atmos. Sci., 37, 441–454, https://doi.org/10.1007/s00376-020-9213-8, 2020.

Tillmann, R., Gkatzelis, G. I., Rohrer, F., Winter, B., Wesolek, C., Schuldt, T., Lange, A. C., Franke, P., Friese, E., Decker, M., Wegener, R., Hundt, M., Aseev, O., and Kiendler-Scharr, A.: Air quality observations onboard commercial and targeted Zeppelin flights in Germany – a platform for high-resolution trace-gas and aerosol measurements within the planetary boundary layer, Atmos. Meas. Tech., 15, 3827–3842, https://doi.org/10.5194/amt-15-3827-2022, 2022.

Tirpitz, J.-L., Frieß, U., Hendrick, F., Alberti, C., Allaart, M., Apituley, A., Bais, A., Beirle, S., Berkhout, S., Bognar, K., Bösch, T., Bruchkouski, I., Cede, A., Chan, K. L., den Hoed, M., Donner, S., Drosoglou, T., Fayt, C., Friedrich, M. M., Frumau, A., Gast, L., Gielen, C., Gomez-Martín, L., Hao, N., Hensen, A., Henzing, B., Hermans, C., Jin, J., Kreher, K., Kuhn, J., Lampel, J., Li, A., Liu, C., Liu, H., Ma, J., Merlaud, A., Peters, E., Pinardi, G., Piters, A., Platt, U., Puentedura, O., Richter, A., Schmitt, S., Spinei, E., Stein Zweers, D., Strong, K., Swart, D., Tack, F., Tiefengraber, M., van der Hoff, R., van Roozendael, M., Vlemmix, T., Vonk, J., Wagner, T., Wang, Y., Wang, Z., Wenig, M., Wiegner, M., Wittrock, F., Xie, P., Xing, C., Xu, J., Yela, M., Zhang, C., and Zhao, X.: Intercomparison of MAX-DOAS vertical profile retrieval algorithms: studies on field data from the CINDI-2 campaign, Atmos. Meas. Tech., 14, 1–35, https://doi.org/10.5194/amt-14-1-2021, 2021.

Villa, T., Gonzalez, F., Miljievic, B., Ristovski, Z., and Morawska, L.: An Overview of Small Unmanned Aerial

Vehicles for Air Quality Measurements: Present Applications and Future Prospectives, Sensors, 16, 1072, https://doi.org/10.3390/s16071072, 2016.

Visser, A. J., Boersma, K. F., Ganzeveld, L. N., and Krol, M. C.: European NOx emissions in WRF-Chem derived from OMI: impacts on summertime surface ozone, Atmos. Chem. Phys., 19, 11821–11841, https://doi.org/10.5194/acp-19-11821-2019, 2019.

Walcek, C. J.: Minor flux adjustment near mixing ratio extremes for simplified yet highly accurate monotonic calculation of tracer advection, J. Geophys. Res.-Atmos., 105, 9335–9348, https://doi.org/10.1029/1999JD901142, 2000.

Wang, H., Lu, X., Jacob, D. J., Cooper, O. R., Chang, K.-L., Li, K., Gao, M., Liu, Y., Sheng, B., Wu, K., Wu, T., Zhang, J., Sauvage, B., Nédélec, P., Blot, R., and Fan, S.: Global tropospheric ozone trends, attributions, and radiative impacts in 1995–2017: an integrated analysis using aircraft (IAGOS) observations, ozonesonde, and multi-decadal chemical model simulations, Atmos. Chem. Phys., 22, 13753–13782, https://doi.org/10.5194/acp-22-13753-2022, 2022.

Wang, Y.-C., Wang, S.-H., Lewis, J. R., Chang, S.-C., and Griffith, S. M.: Determining Planetary Boundary Layer Height by Micropulse Lidar with Validation by UAV Measurements, Aerosol. Air. Qual. Res., 21, 200336, https://doi.org/10.4209/aaqr.200336, 2021.

Weaver, A. and Courtier, P.: Correlation modelling on the sphere using a generalized diffusion equation, Q. J. Roy. Meteor. Soc., 127, 1815–1846, https://doi.org/10.1002/qj.49712757518, 2001.

Wu, X., Elbern, H., and Jacob, B.: The assessment of potential observability for joint chemical states and emissions in atmospheric modelings, Stoch. Environ. Res. Risk. Assess., 36, 1743–1760, https://doi.org/10.1007/s00477-021-02113-x, 2022.

Yang, S., Li, X., Zeng, L., Yu, X., Liu, Y., Lu, S., Huang, X., Zhang, D., Xu, H., Lin, S., Liu, H., Feng, M., Song, D., Tan, Q., Cui, J., Wang, L., Chen, Y., Wang, W., Sun, H., Song, M., Kong, L., Liu, Y., Wei, L., Zhu, X., and Zhang, Y.: Development of multi-channel whole-air sampling equipment onboard an unmanned aerial vehicle for investigating volatile organic compounds' vertical distribution in the planetary boundary layer, Atmos. Meas. Tech., 16, 501–512, https://doi.org/10.5194/amt-16-501-2023, 2023.

Zhang, L., Brook, J. R., and Vet, R.: A revised parameterization for gaseous dry deposition in air-quality models, Atmos. Chem. Phys., 3, 2067–2082, https://doi.org/10.5194/acp-3-2067-2003, 2003.

6

The effects of assimilating Zeppelin campaign measurements on air quality analyses

This chapter presents the results of the assimilation of flight data from the 2020 Zeppelin campaign into EURAD-IM, using its 4D-Var assimilation system. The objective of this study is to investigate the additional information content of these observations collected in the planetary boundary layer (PBL) and to evaluate its impact on air quality analysis at local and regional scales. To this end, two periods of the Zeppelin campaign are selected for a case study in two areas with distinct emission profiles to investigate the impact of the assimilation of measurements collected in the PBL. The first studied episode analyses air quality in North Rhine-Westphalia, which is one of the most polluted urban and industrial regions in Germany, from 29 May to 03 June 2020. The second period includes 11 to 13 September 2020, when the Zeppelin flew over the city of Frankfurt. The chapter is divided into three sections, each designed to answer a specific research question:

1. Section 6.1: This case study examines the impact of Zeppelin-based data assimilation on pollutant distribution under a highly uncertain emission rate scenario. It aims to evaluate the effectiveness of in situ observations within the PBL for optimising emission estimates compared to conventional ground-based observations.

2. Section 6.2: The goal of this study is to assess the model's performance when assimilating different observational datasets and to identify the specific contribution and the added value of the airborne observations within the PBL.

3. Section 6.3: This study explores the usability of the Zeppelin observations in a polluted urban environment such as Frankfurt. It evaluates the potential benefits of assimilating

Zeppelin-based observations for improving the vertical distribution of pollutants in the PBL and discusses the limitations related to the model performance. The potential benefits of Zeppelin observation assimilation that can be achieved in this area are evaluated and the limitations encountered when assimilating observations from the PBL into the EURAD-IM model are discussed.

6.1 Case Study 1: Impact of Zeppelin data assimilation on air quality analysis and emissions observability

The impact of Zeppelin data assimilation (DA) on the air pollution analysis is studied and evaluated using EURAD-IM with its 4D-Var assimilation system. The data collected by the Zeppelin NT in the North Rhine-Westphalia (NRW) region for 29 May and between 01 and 03 June 2020 are considered (see Table 4.1). The selection of this region is particularly pertinent as it is a prominent pollution hotspot in both Germany and Europe. With a population exceeding 18 million, NRW is not only subject to urban pollution but also experiments high emissions from industrial and energy activities, including those of large power plants, in addition to emissions from a dense highway network.

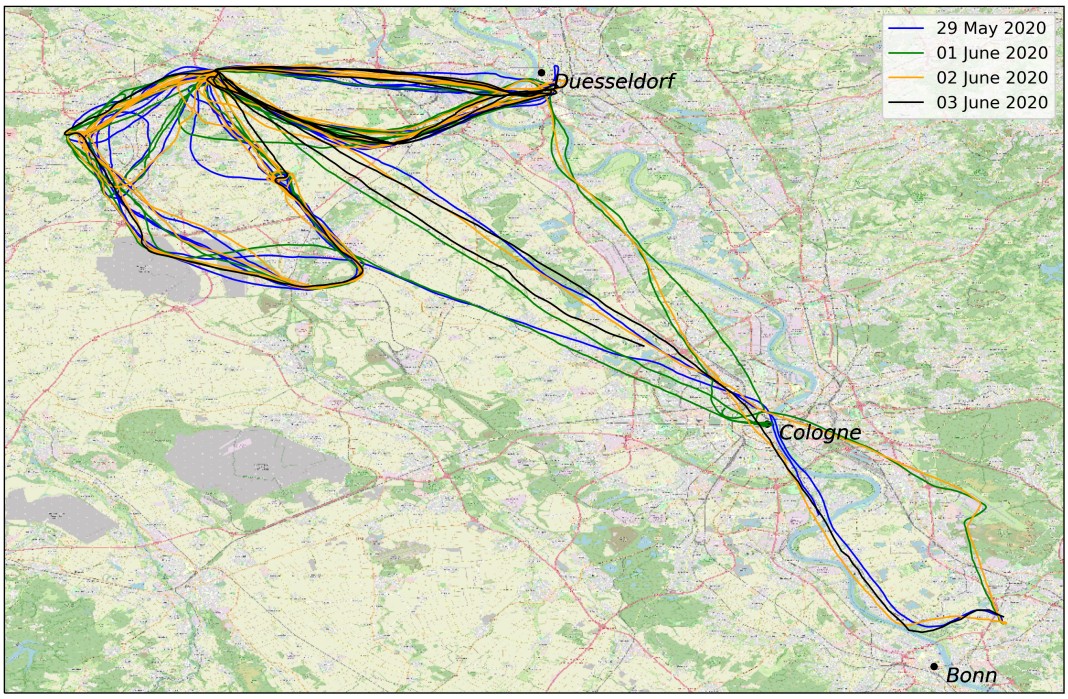

Figure 6.1: *Zeppelin flights path in North Rhine-Westphalia on 29 May and 01–03 June 2020.*

6.1.1 Meteorological conditions

Meteorology plays a key role in the development, intensification, or dissipation of pollution episodes (Seinfeld and Pandis, 2016). At the end of May 2020, the expansion of the high-pressure ridge towards Western Europe led to high pressure over most of Germany, as shown by the geopotential height at 500 hPa on 29 May 2020 in Fig. 6.2a. The presence of a warm air mass, advected by a trough over the eastern Atlantic Ocean, resulted in unusually high temperatures for the season. This heat peaked from 30 May to 01 June, with temperatures

exceeding 29°C in NRW.
From the beginning of June, a low pressure system formed over Poland and Ukraine, accompanied by an upper air cut-off (Fig. 6.2b) due to the inflow of cold air at high altitudes. The transition between these two pressure systems on 02 and 03 June led to a decrease in pressure over western Germany and a change in wind direction from easterly to westerly winds, as shown by the WRF model wind data for Cologne in Fig. 6.3. Temperatures also began to decrease, and several thunderstorms developed in the western part of Europe.
Three out of the four considered days are therefore characterised by high atmospheric stability, creating a stable boundary layer that keeps pollutants close to the surface and causes them to accumulate. High temperatures, long periods of insolation, and clear skies favour the development of tropospheric ozone concentrations, particularly in areas with high ozone precursor emissions such as the NRW region.

(a) *29 May 2020*

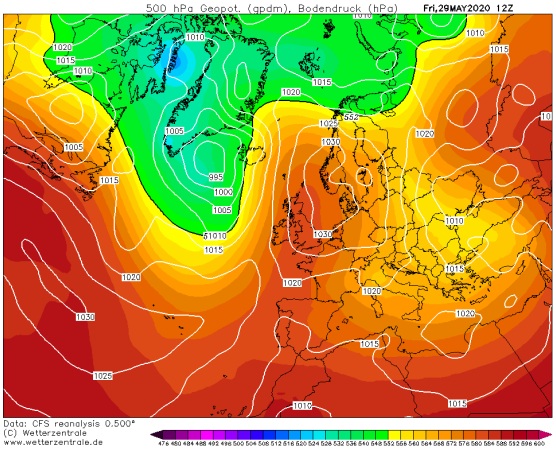

(b) *03 June 2020*

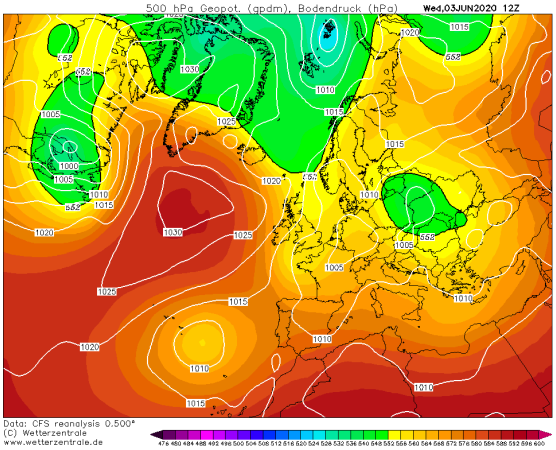

Figure 6.2: *500 hPa geopotential height (in gpdm, color-coded) and surface pressure (in hPa, white lines) over Europe on 12 September 2020 at 00 UTC from GFS reanalysis data (`www.Wetterzentrale.de`). The black line indicates the 552 gpdm contour.*

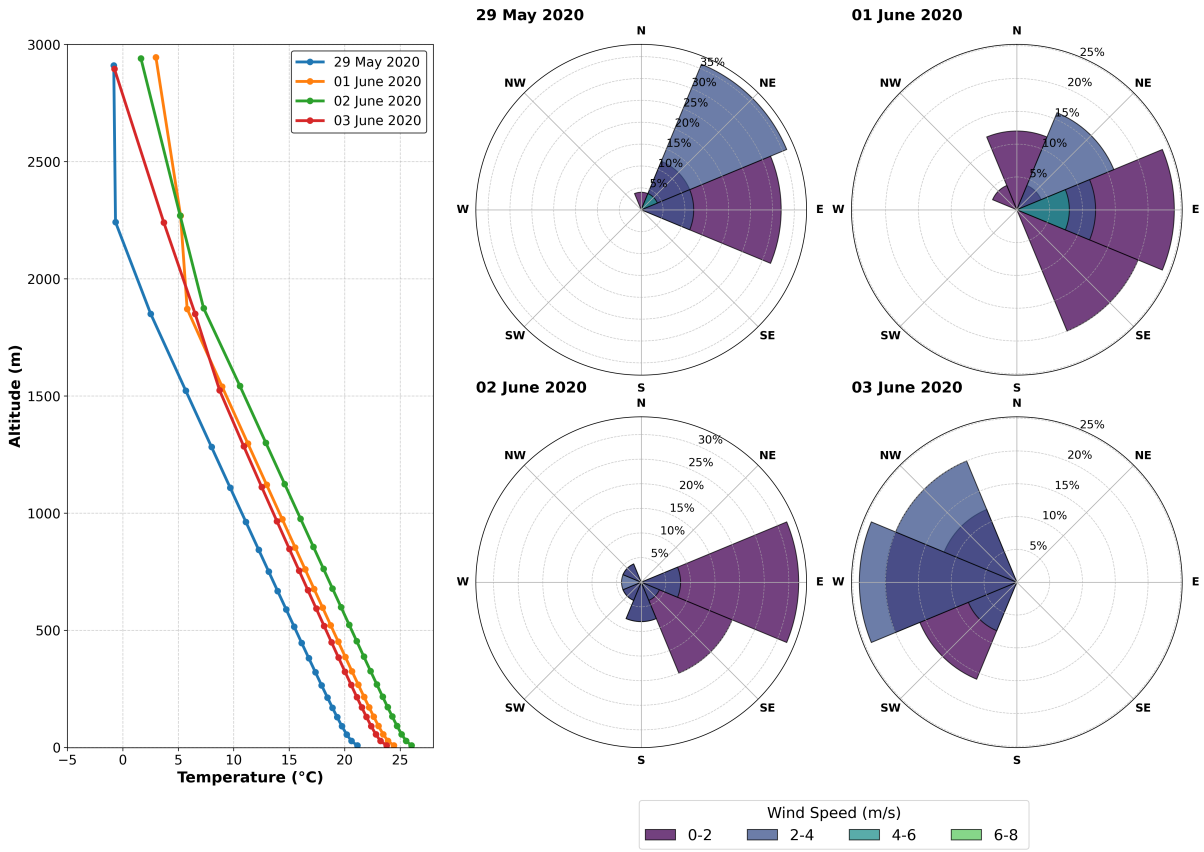

Figure 6.3: *Temperature profiles (°C) at 15 UTC and daily wind roses at the Cologne city grid box for 29 May and 01–03 June 2020 from WRF model output.*

6.1.2 Simulation setup

Three different simulations are conducted using the EURAD-IM for the dates 29 May and 01 to 03 June 2020. They were configured as follows:

1. *EXP-CTR* represents the background simulation or control simulation (without assimilation).
2. *EXP-ZEP* represents the 4D-Var simulation in which the O_3, NO, NO_2 and CO from the 2020 Zeppelin campaign are assimilated.
3. *EXP-GRD* represents the simulation in which observations of O_3 and NO_2 from ground-based monitoring stations in NRW are assimilated.

A six-day spin-up period (from 23 May to 28 May 2020) was conducted to ensure that the simulations started with a realistic initial state. During this stage, no data assimilation was performed. Table 6.1 presents a summary of the characteristics of each simulation. For all simulations, as well as the spin-up, the business-as-usual TNO-MACC_ II emissions inventory for the year 2016 was used. Notably, the emission corrections for each day remain independent of the one derived at previous days. Thus, only the initial conditions are provided by the previous day's analysis. This approach allows for a comprehensive analysis of the model's performance on a day-by-day basis.

Table 6.1: *Details of simulation setups.*

Simulation	Number of Iterations	Assimilated Observations	Assimilation Window
EXP-CTR	-	-	-
EXP-ZEP	10	Observations of O_3, NO, NO_2, and CO from Zeppelin flights	From 00 UTC to the hour for which Zeppelin observations are available
EXP-GRD	15	Observations of O_3 and NO_2 from ground-based stations	24 hours

6.1.3 Assimilation results

The reduction of the cost function J (see section 2.2) is a key performance indicator for verifying the successful assimilation of observations in the 4D-Var system. A significant reduction indicates that the model has accurately identified and applied corrections that minimise the discrepancy between the analysis (i.e. the model prediction after the 4D-Var assimilation) and the observations. Due to the high temporal resolution of the Zeppelin data, the number of iterations was reduced to 10 in order to keep the computational cost to a reasonable level.
The total costs of the *EXP-ZEP* simulations were successfully reduced by more than 63% and up to 90% after 10 iterations, while the costs of the *EXP-GRD* simulation were reduced by 38% to 63% in 15 iterations (Table 6.2). This indicates that the convergence to the solution was faster for the Zeppelin data assimilation. It is known that the speed of convergence is higher when the assimilation window is shorter in complex, chaotic and non-linear systems (Pires et al., 1996), as is the case here for chemical data assimilation. The assimilation window is 24 hours

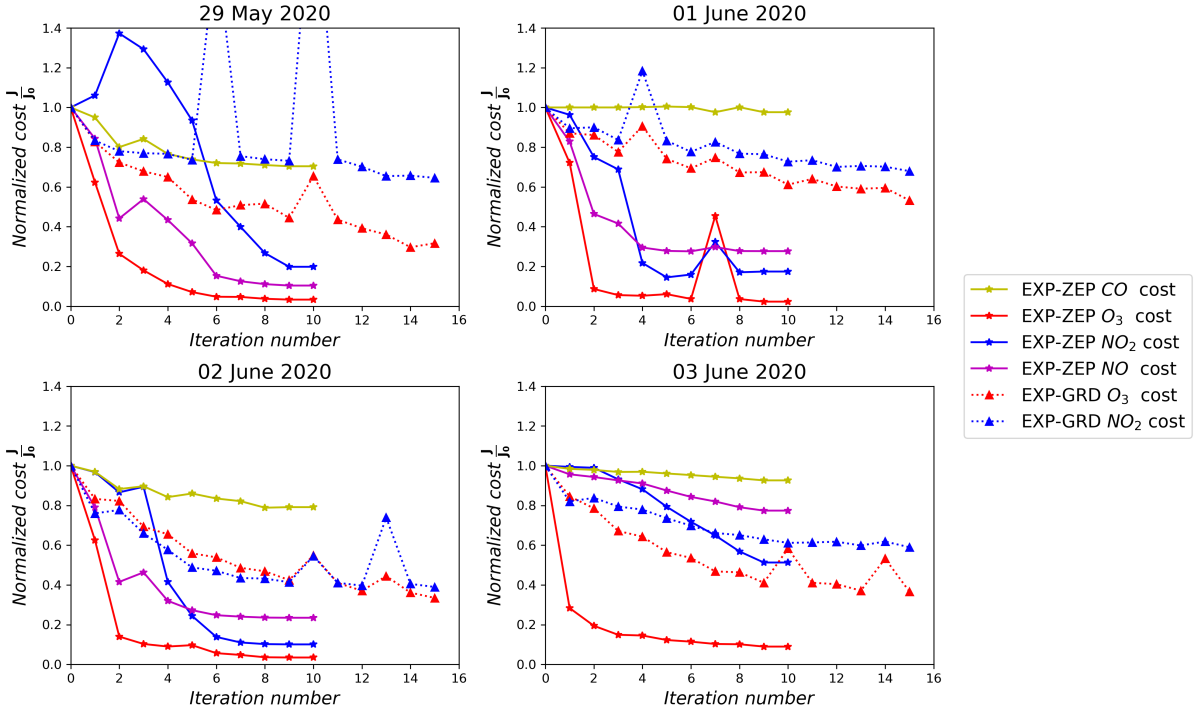

Figure 6.4: *Evolution of species-specific costs over iterations for the 4 studied days for the two assimilation runs: EXP-ZEP and EXP-GRD.*

Table 6.2: *The total cost reduction for data assimilation simulations.*

Simulation	Date	Initial cost	Cost at the best iteration	Number of observations	Reduction
EXP-ZEP	29 May 2020	715	261	2256	63.5%
	01 June 2020	2017	218	2146	89.2%
	02 June 2020	4925	511	2093	89.6%
	03 June 2020	1994	183	1017	90.8%
EXP-GRD	29 May 2020	1338	647	712	51.6%
	01 June 2020	1192	433	677	63.7%
	02 June 2020	1777	1087	663	38.8%
	03 June 2020	1872	880	652	53.0%

for *EXP-GRD* and less than a 18 hours for *EXP-ZEP*. The largest reduction for *EXP-ZEP* was noted for O_3, with a reduction of more than 90%, while a weaker reduction of up to 30% was seen for CO (Fig. 6.4). This can be explained by the small contribution of CO to the total cost (only between 4% and 14%) and the fact that the CO background model states are close to the observations. As CO is not assimilated in the *EXP-GRD* simulation, the analysis of the results will focus exclusively on O_3, NO, and NO_2.

Emission rate optimisation

The emission correction factors (EFs) for the two assimilation experiments for NO_2 are presented in Fig. 6.5. NO_2 is the emitted species with the largest correction factors; however, smaller factors were derived for NO, CO, and SO_2 due to the correlation between species. In the case of *EXP-ZEP*, the emission factors demonstrate a range of 0.09 to 1.79. The corrected area is more localised around the areas where the Zeppelin was flying. In the case of *EXP-GRD*, the emission factors exhibit a range of variation between 0 and 4.5. The area affected is typically larger than that observed in *EXP-ZEP*, due to the extensive distribution of stations. Consequently, regions outside of NRW and nearby countries were impacted by emission corrections. In terms of absolute values, the assimilation of Zeppelin data resulted in a reduction of NO_x emissions by up to -48.3 t, -28.5 t, -46.5 t and -38.4 t per grid box, and an increase of +3 t, +0.1 t, +0.7 t and +0,2 t per grid box for 29 May and from 01 to 03 June 2020, respectively. For *EXP-GRD*, a reduction of up to -4 t, -9.3 t, -8.8 t and -31.9 t per grid box and an increase of +3.4 t, +3.3 t, +0.7 t and +2 t per grid box (Fig. A.2) was analysed for the same dates. Overall, the reduction in emissions is more intensive in the case of *EXP-ZEP*. Furthermore, the emission factors within the same region fluctuate on a daily basis, likely due to variations in wind patterns and their effect on the inversion process. This occurs because emission optimisation relies on utilising the information content provided by the observations in the 4D-Var inversion system. When wind conditions change from day to day, the dispersion of pollution and transport also differs, leading to changes in the information content. Therefore, the assimilation of these observations results in different emission correction factors.

Although the optimisation of emission rates in the 4D-Var system does not allow sector-specific optimisation, but rather optimisation of total emissions per grid, the model provides good optimisation for certain sectors, especially for the dominant sector. As an example, Fig. 6.6 shows the total change in NO_x emissions between the optimised and original emission in-

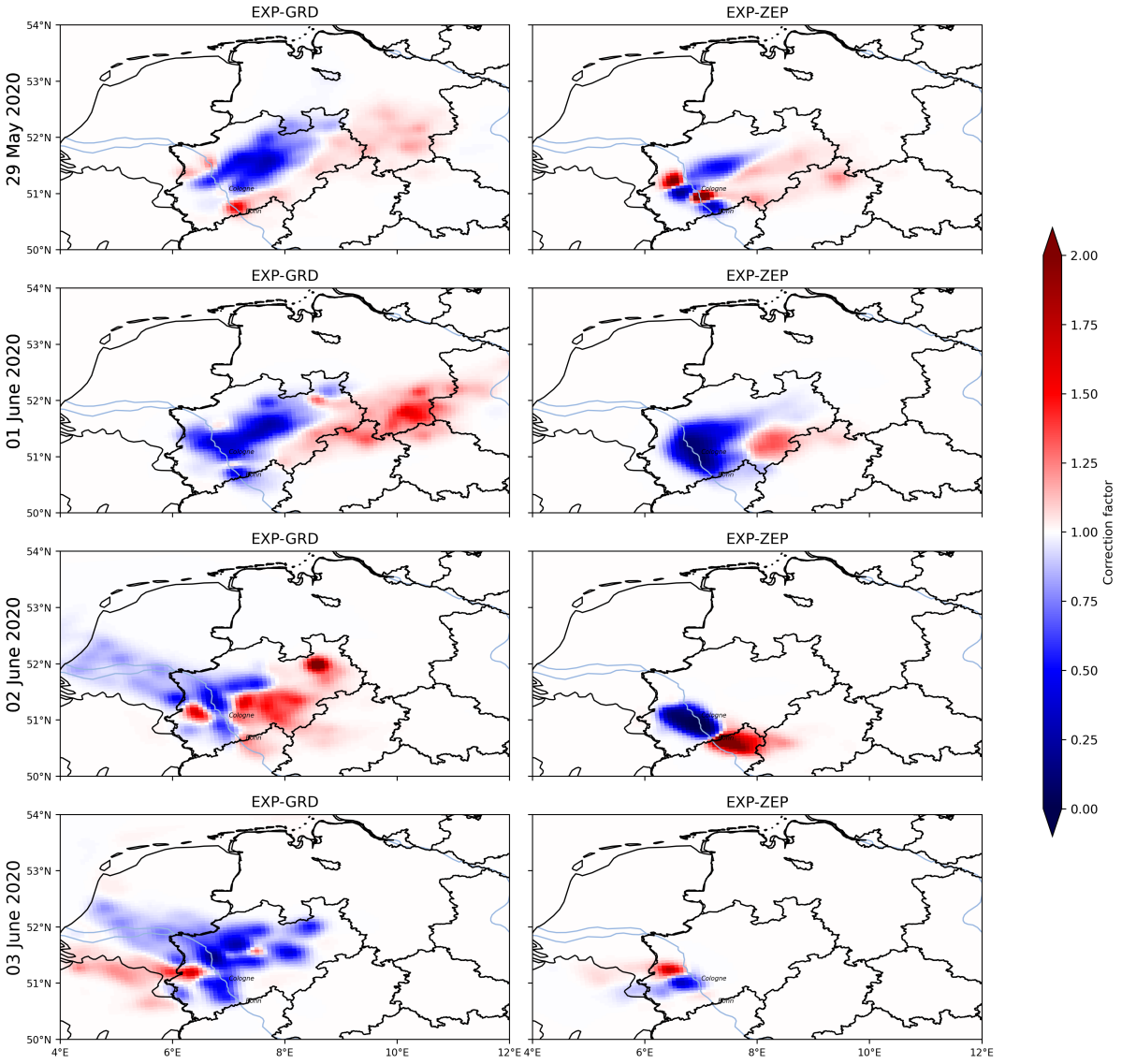

Figure 6.5: *NO_2 emission factors resulting from the EXP-ZEP and EXP-GRD simulations for the four study days.*

ventories for different emission sectors on 02 June 2020 for *EXP-ZEP* and *EXP-GRD*. The optimised NO_x emissions for each sector are derived by applying the daily emission factors for NO and NO_2 to the corresponding original emissions of each sector separately. In the figure, negative changes (reductions) and positive changes (increases) are summed separately for all grid boxes.

The public energy sector is the primary sector impacted by the change in emissions for the *EXP-ZEP* experiment, with a notable total reduction of -101.2 t. Regarding *EXP-GRD*, emissions from the public energy sector, transport sector and industry sector are most significantly reduced, with total reductions of 45.1 t, 42.9 t and 36.5 t, respectively. This indicates that the assimilation of Zeppelin data led to a more than twofold reduction in emissions in the public energy sector compared to the reduction achieved by the assimilation of ground station data alone. In the study area, three point sources of emissions classified as public energy sector

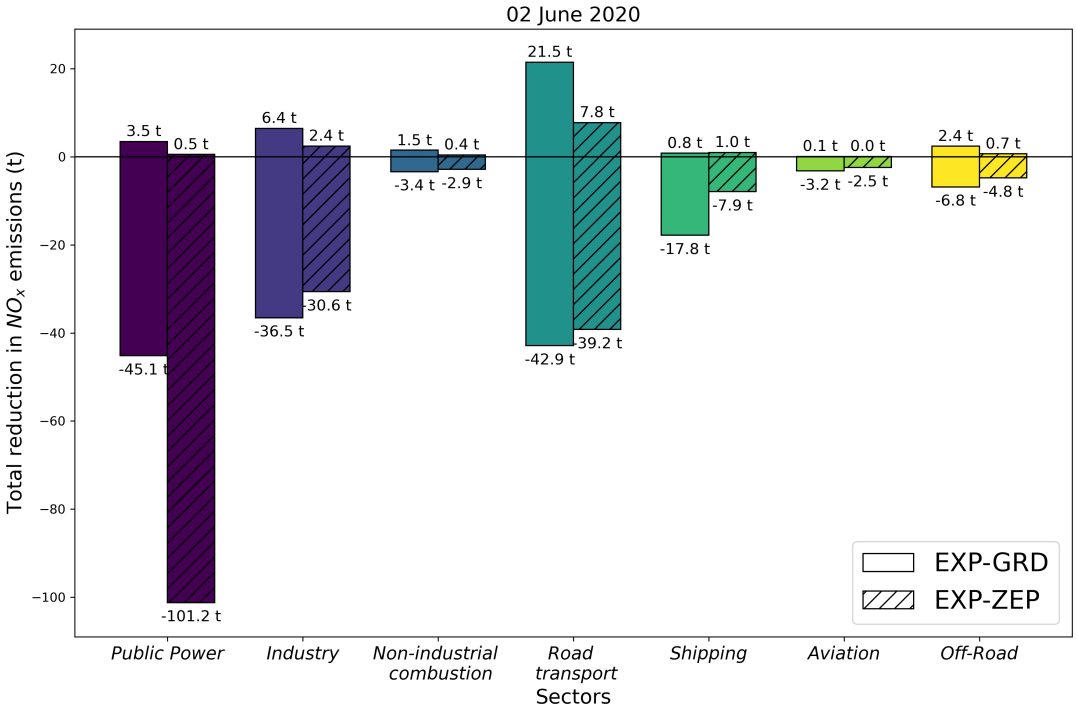

Figure 6.6: *Total change in NO_x emissions between the optimised and original emission inventories for different emission sectors on 02 June 2020. Emission reductions and increases are summed separately. Bars indicate contributions from EXP-ZEP (non-shaded) and EXP-GRD (shaded) to the emission change.*

were identified, namely the Neurath, Niederaußem and Weisweiler power plants. These plants are among the largest power plant emitters in Germany (Fig. 6.7). The assimilation of the Zeppelin observations reduced the emissions of the two power plants Neurath and Niederaußem significantly.

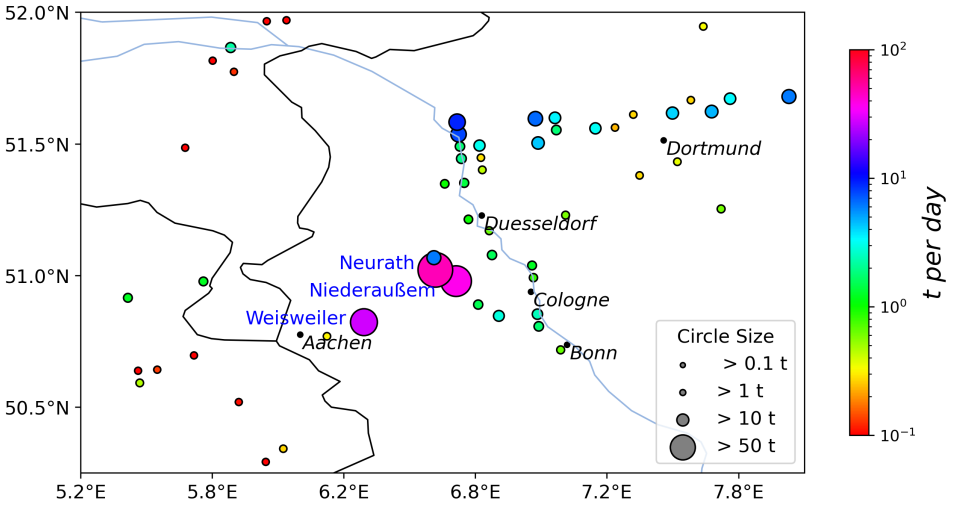

Figure 6.7: *Map of daily NO_x emissions from point sources (mainly industry and power plants) in the region of North Rhine-Westphalia (NRW).*

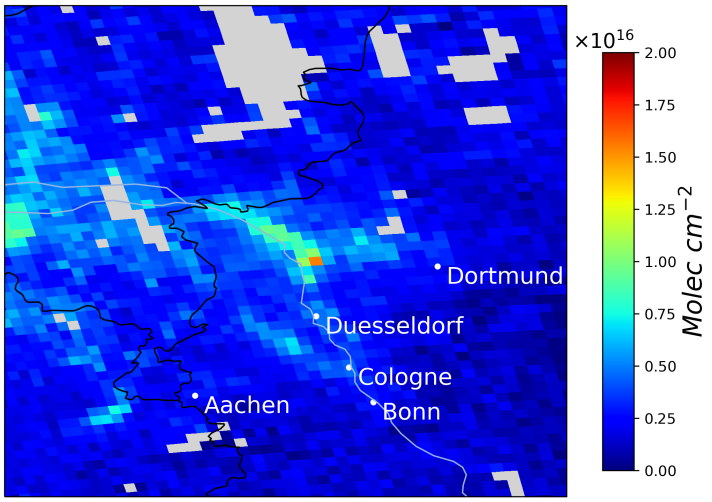

Figure 6.8: *Tropospheric NO_2 column (in molec cm^{-2}) derived from TROPOMI data at 12:43 UTC on 02 June 2020. Grey pixels indicate data filtered out based on the TROPOMI quality flag ($q < 0.75$).*

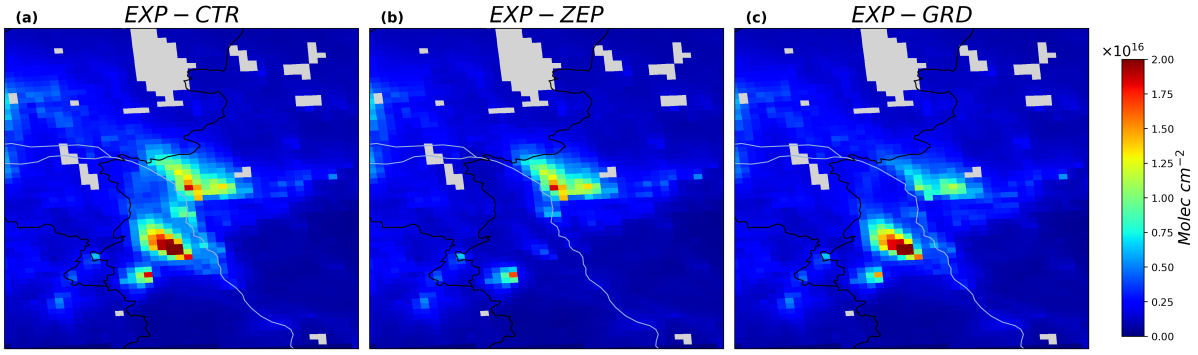

Figure 6.9: *The modelled tropospheric column NO_2 (in molec cm^{-2}) over the analysis region for 02 June 2020 at 12:43 UTC. The three subfigures represent: (a) the reference simulation (left), (b) the 4D-Var analysis from the Zeppelin simulation (middle), and (c) the 4D-Var analysis from the ground-based assimilation simulation (right). Grey pixels indicate data filtered out based on the TROPOMI quality flag ($q < 0.75$).*

In general, the validation of emission fluxes is challenging due to the unavailability of observations with the necessary spatial and temporal resolution. However, the TROPOMI satellite observations, which provide high spatial and temporal coverage and high spatial resolution, make this possible. An improvement in the modelled spatial distribution of pollutant concentrations, when compared to satellite observations, indicates a better representation of the underlying emission sources. Several studies have demonstrated that the tropospheric NO_2 columns collected by TROPOMI provide the best opportunity to date for determining sources of NO_2 during daytime (Griffin et al., 2020; Jin et al., 2021; Lange et al., 2022).
Figure 6.8 presents TROPOMI satellite images from 02 June 2020 for the NO_2 tropospheric column. The model equivalent of the NO_2 tropospheric column was calculated for the 4D-Var analyses and the background as shown in Fig. 6.9. Figure 6.9(a) shows the background NO_2 column including a plume of elevated NO_2 column values with a maximum value of 2.38×10^{16}

molec cm^{-2}. This plume is attributed to the Neurath and Niederaußem power plants that are only separated by about 5-10 km. A similar plume is visible in Fig. 6.9(c), which relates to the *EXP-GRD* simulation and shows with NO_2 column values of up to 2.35×10^{16} molec cm^{-2} at the same location. In contrast, Fig. 6.9(b), which shows the tropospheric NO_2 column derived from the Zeppelin data assimilation analysis, demonstrates the absence of this plume from the power plants with a maximum value of 0.40×10^{16} molec cm^{-2}. The satellite image displays a plume of 0.69×10^{16} molec cm^{-2}, thereby confirming the strength of the reduction. On 02 June 2020, the assimilation of Zeppelin observations proved effective in optimising emissions, while the assimilation of ground-based data was unable to reproduce the reduced plume from the power plants Niederaußem and Neurath.

Given that the power plant's emissions are released at high altitudes (approximately 350 m), the Zeppelin emerges as the most suitable platform for conducting observations with rich information content about pollutant concentrations at such heights. Ground observations on 02 June 2020 did not provide information that could help integrate a substantial change in power plant emission rates, further highlighting the need for observations in the PBL. One of the main advantages of Zeppelin observations lies not only in their ability to operate at high altitudes but also to cross emission plumes multiple times during a flight. On the one hand, the Zeppelin thus provides valuable information on the spatio-temporal evolution of the emitted pollutants. On the other hand, these repeated observations near the emission sources will constrain the assimilation system toward an optimal optimisation of the emission rates.

The findings of the emission optimisation for 29 May, 01 and 02 June demonstrate substantial reductions in NO_x emissions for the *EXP-ZEP* experiment, which exceeds those derived for the *EXP-GRD* experiment (see Fig. A.2). However, the results for 03 June demonstrate a high similarity between the two experiments, with a reduction in NO_x emissions of up to -38.4 t for *EXP-ZEP* compared to -31.9 t for *EXP-GRD* experiment. To elucidate the reasons for this variation in performance for *EXP-GRD* compared to *EXP-ZEP*, Fig. 6.10 illustrates the analysis increments of NO_x (NO + NO_2) as well the wind field at Model level 9 (at approximately 350 m altitude). On 02 June 2020, the Zeppelin flew downwind and close to the power plants Niederaußem and Neurath, while the ground stations were mainly located on the upwind side. The wind was relatively weak (about 2 m s^{-1} around the power plants), which led to a weak dispersion of the pollution. In the case of 03 June 2020, the Zeppelin was flying on the downwind side during part of the flight, which facilitated the detection of emissions from the power plants. Most of the ground monitoring stations (12 out of 15) were located on the downwind side. In addition, the dispersion of pollutants was enhanced due to the presence of strong winds of up to 7 m s^{-1} in the Northeast of the domain. As a result, emissions from power plants and industries located at high altitudes are transported over long distances and captured by ground stations. Furthermore, the reduced atmospheric stability results in enhanced turbulence and vertical mixing within the planetary boundary layer, facilitating the exchange of pollutants between higher altitudes and the surface.

These results demonstrate that Zeppelin observations are more effective at measuring elevated emissions compared to ground-based observations. This advantage is particularly evident in situations where ground-based stations are inadequately positioned relative to large-point emission sources and during stable atmospheric conditions with limited vertical mixing.

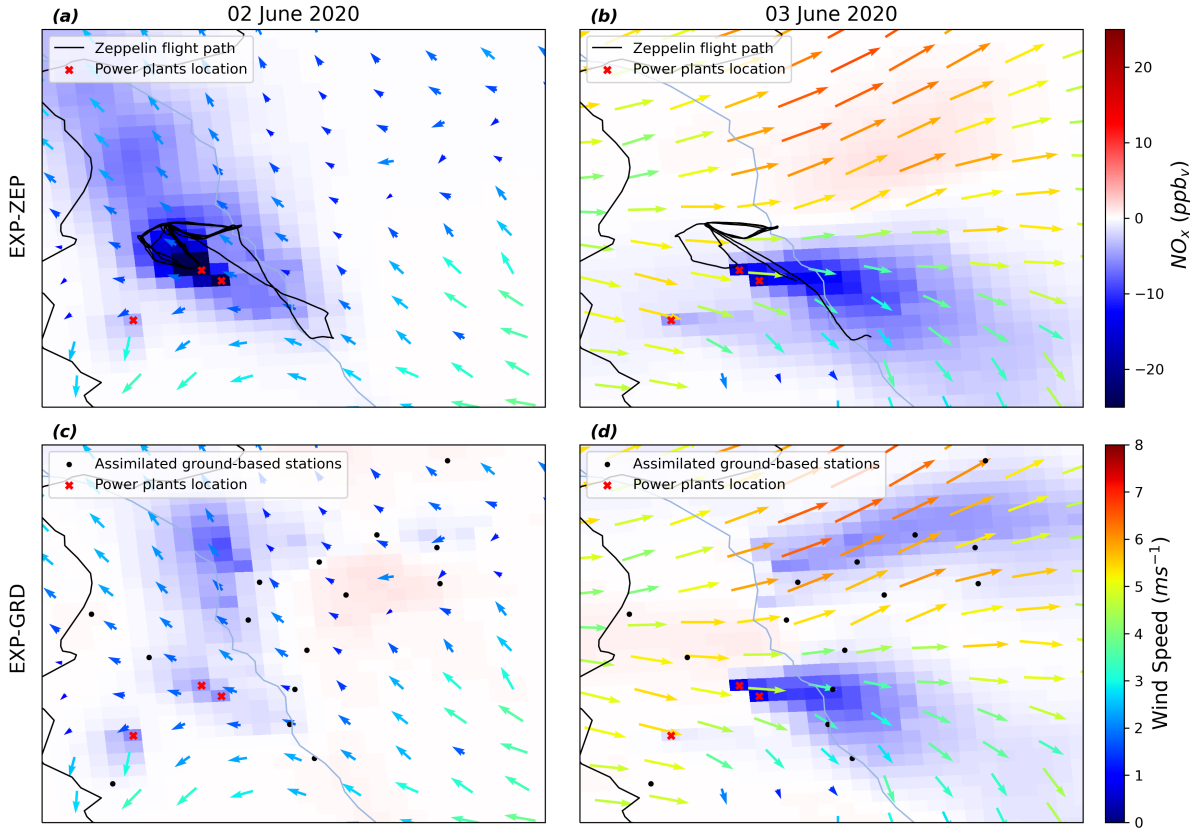

Figure 6.10: *NO_x (NO_2 + NO) analysis increment (analysis - background) at model layer 9 (350 m) at 10:00 on 02 and 03 June 2020 for the two experiments: EXP-ZEP (upper panels) and EXP-GRD (lower panels). Wind vectors at the same model layer at 10:00 are shown on the right. The location of the observations being assimilated is indicated on each map, showing the Zeppelin flight path (upper panels) and ground stations (lower panels).*

Validation against independent observations

For the evaluation of the performance of the 4D-Var assimilation of Zeppelin observations, it is necessary to have a comparison with independent observations. For this purpose, a number of ground-based stations in NRW that were not assimilated in the *EXP-GRD* simulations are selected. The region of validation is illustrated in Fig. A.3. Figure 6.11 and 6.12 show the root mean square error (RMSE) of each day for the three species NO, NO_2 and O_3, averaged over all validation observations.

For NO and NO_2, statistics show no significant difference between the experiments, except for 01 June. On this day, *EXP-ZEP* shows a superior RMSE reduction for NO of -1.64 $\mu g\,m^{-3}$ compared to the -1.51 $\mu g\,m^{-3}$ achieved by *EXP-GRD*. Similarly, the NO_2 statistics are improved for both assimilation experiments compared to the reference simulation *EXP-CTR*. The *EXP-ZEP* reduces the RMSE by -3.78 $\mu g\,m^{-3}$ against -3 $\mu g\,m^{-3}$ for *EXP-GRD*. Both assimilation experiments yield nearly identical results, with a negligible impact on all days except for one (01 June 2020). These findings suggest that there may be no significant difference in the corrections of surface emissions between the two assimilation experiments. The improvement obtained from *EXP-ZEP* on 01 June 2020 underscores the potential of Zeppelin data assimilation to positively

impact the surface concentrations for NO and NO_2, similarly to the ground data assimilation.

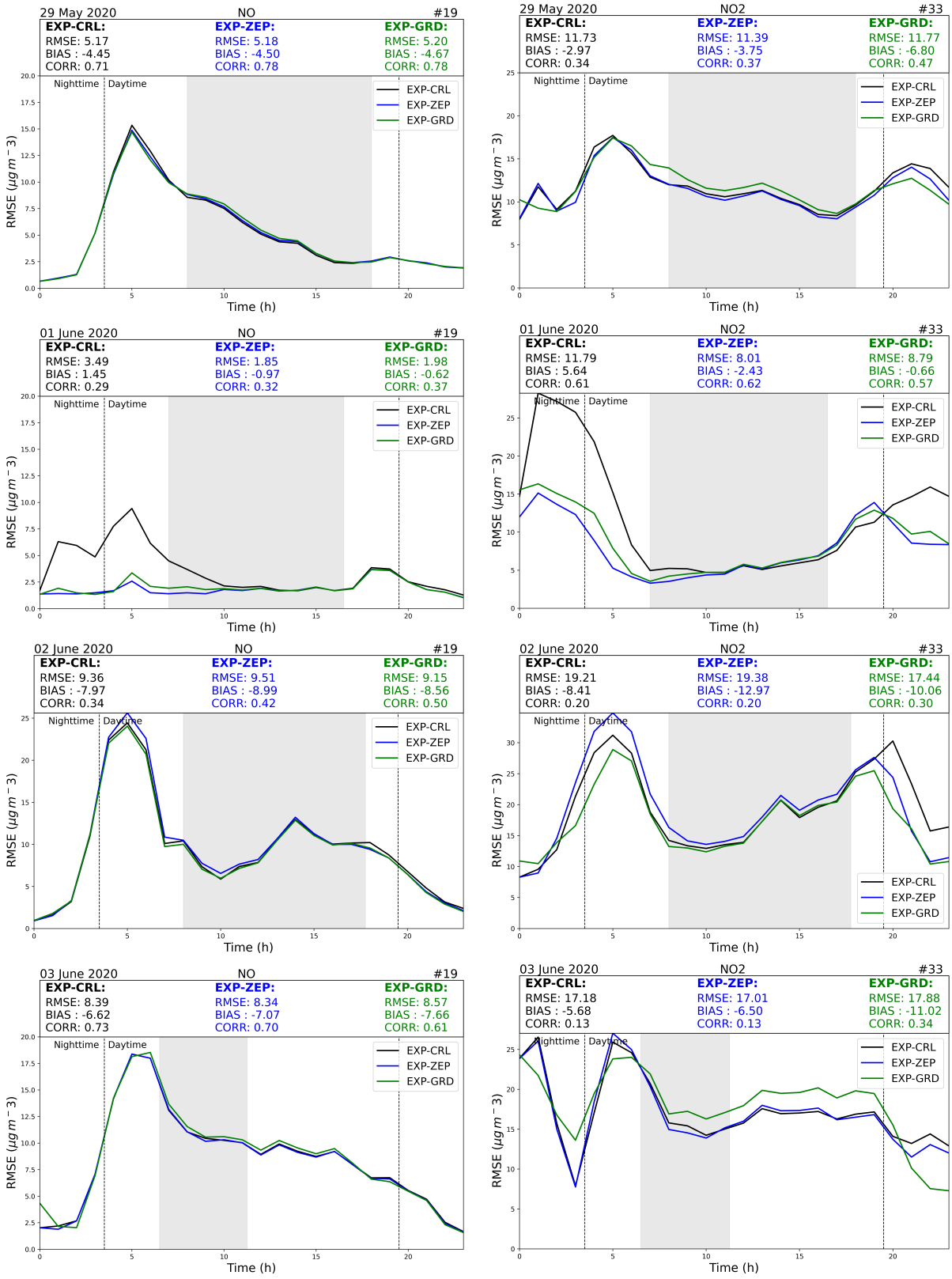

Figure 6.11: *Root mean square error (RMSE) for NO and NO_2 from all model simulations, based on the comparison with independent ground-based observations for the four days under consideration. The shaded grey region represents the period of available Zeppelin data. Black dashed lines indicate local sunrise and sunset times.*

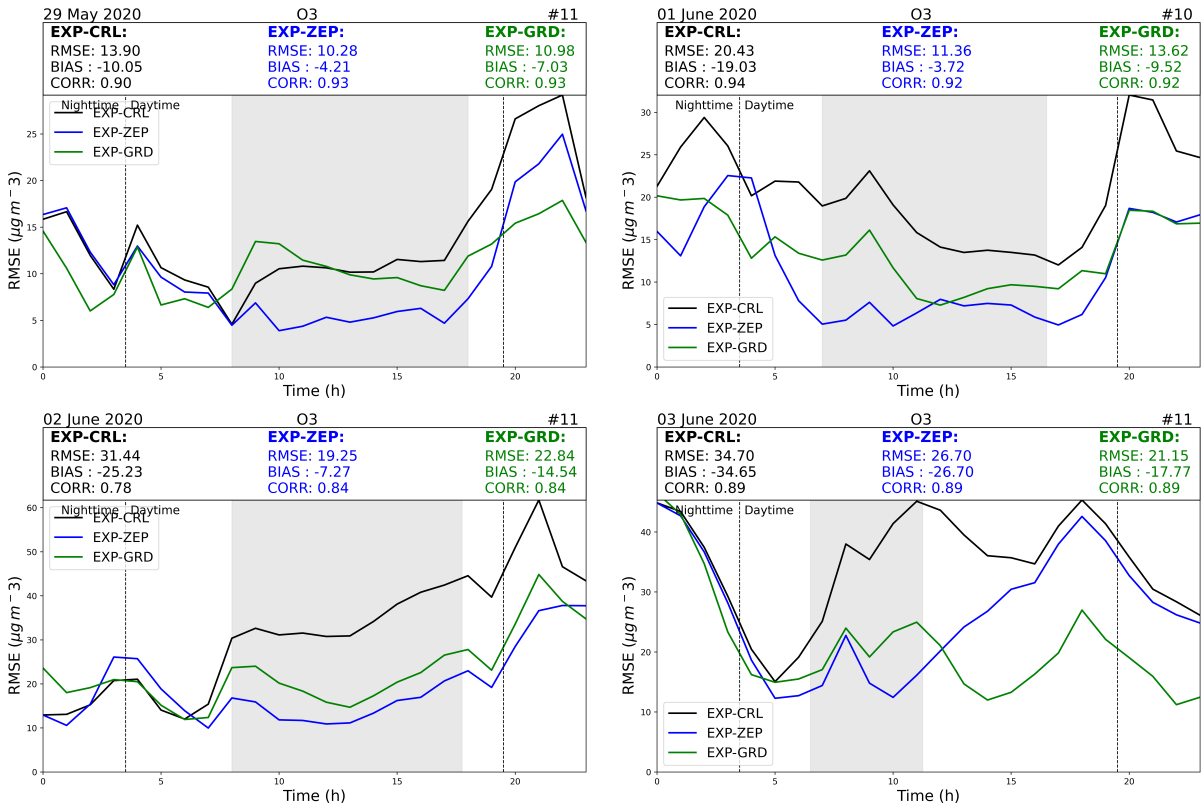

Figure 6.12: *Same as 6.11 but for O_3.*

The improvements in the analyses are more evident in the case of O_3 concentrations across all days (Figure 6.12). The *EXP-ZEP* demonstrated superior performance in comparison to the *EXP-GRD* during the initial three days. The RMSE for the *EXP-ZEP* was reduced by 26.04% (-3.62 µg m^{-3}) on 29 May, 44.40% (-9.07µg m^{-3}) on 01 June and 38.77% (-12.19 µg m^{-3}) on 02 June. In comparison, *EXP-GRD* decreased the RMSE by 21.01% (-2.92 µg m^{-3}), 33.33% (-6.81 µg m^{-3}) and 27.35% (-8.6 µg m^{-3}) for the same days respectively. This result indicates that the assimilation of Zeppelin observations positively affects the surface O_3 concentration. The resulting improvement is superior to the assimilation of ground-based observations, particularly during the daytime.

In contrast, on 03 June 2020, the *EXP-GRD* demonstrated a superior model performance, with a reduction in RMSE of 39.05% (-13.55 µg m^{-3}) in comparison to the 23.05% reduction (-8.00 µg m^{-3}) analysed in the *EXP-ZEP* simulation. However, the *EXP-ZEP* is still superior in performance on this day within the assimilation window (shaded area in Fig. 6.11). This is evidenced by a reduction of RMSE (calculated over the assimilation window) of 54.33% (-18.49 µg m^{-3}) for *EXP-ZEP* in comparison with 39.26% (- 13.36 µg m^{-3}) for *EXP-GRD*. This reflects a better emission rate optimisation for the local power plants.

The superior performance of the assimilation of ground observations, especially after 12 UTC, is related to a successful assimilation of ground-based observations. On 03 June 2020, unlike other days, good observability of the emissions is achieved by ground-based observations due to their favourable position with respect to wind directions and emission sources. As a result,

the emissions from the two largest power plants in the study area are well-optimised, similar to the results obtained from the Zeppelin data assimilation. Nevertheless, given the spatial distribution of the assimilated ground stations in the NRW and the wind conditions on that day, the emission optimisation from ground observations is applied to a broader region much larger than the optimisation resulting from the Zeppelin assimilation (see Fig. 6.5, bottom plots). The reduction of emissions in altitude from other power plants and industries in the region was considerable (see Fig. A.6), which means that the assimilation resulted in a better representation of emissions in the altitude of the NRW.
In contrast, for the *EXP-ZEP* analysis, the observations available for assimilation are limited spatially compared to the ground observations and even temporally compared to the Zeppelin observations on other days. The relatively strong winds at higher altitudes likely led to a strong pollution dispersion and transportation of pollutants from distant regions. When observations are limited in time, as was the case for *EXP-ZEP* on 03 June, only a part of the relevant information content is captured by the observations, leading to a limited impact when assimilated. These findings highlight the critical need for a long assimilation window, particularly on days characterised by strong dispersion, to achieve a better performance.

Long range transport

Due to the long-range transport of pollutants, an improvement in performance was found for stations further away and even outside the German borders. Figure 6.13 shows the hourly O_3 RMSE calculated at stations in Belgium and the Netherlands. An improvement in performance is seen in the *EXP-ZEP* analysis on 29 May and 01 June. The RMSE decreased by 2.21 $\mu g\,m^{-3}$ and 2.7 $\mu g\,m^{-3}$ in the *EXP-ZEP* experiment, in contrast to the 0.29 $\mu g\,m^{-3}$ and 1.57 $\mu g\,m^{-3}$ reductions by the *EXP-GRD* experiment. The positive effect can be attributed to the transport of the increment outwards from Germany, a consequence of the dominance of south-easterly and southerly winds on these days.
The long-range effect on 02 June showed a slight superiority of *EXP-GRD* (-1.28 $\mu g\,m^{-3}$ in RMSE) compared to *EXP-ZEP* (-0.99 $\mu g\,m^{-3}$ in RMSE). On 03 June, the *EXP-GRD* showed a significantly larger reduction in the RMSE (-2.32 $\mu g\,m^{-3}$ in RMSE) compared to the *EXP-ZEP* (-0.83 $\mu g\,m^{-3}$ in RMSE). The enhanced improvement of *EXP-GRD* can be attributed to initial value corrections and emission optimisation in Belgium and the Netherlands resulting from the assimilation of ground data on 02 and 03 June 2020 (as shown in Fig. 6.5). The relatively strong winds at high altitudes influenced the optimisation process. During assimilation, the information contained in ground observations was exploited to retrace the origin of the observed signals. This allows for detecting emission sources and pollutant concentrations in Belgium and the Netherlands, thereby improving the O_3 concentrations at the surface. The limited improvement obtained after the assimilation of the Zeppelin observation can be attributed to the constraints of availability and spatial distribution of the observations.
In summary, the assimilation of Zeppelin data demonstrated its ability to transport the increment over longer distances in the downwind regions. This impact is stronger than the effect of ground assimilation. However, the enhancement in the upwind areas may be limited, as it depends on the model's ability to derive corrections for emission rates and initial values in those areas.

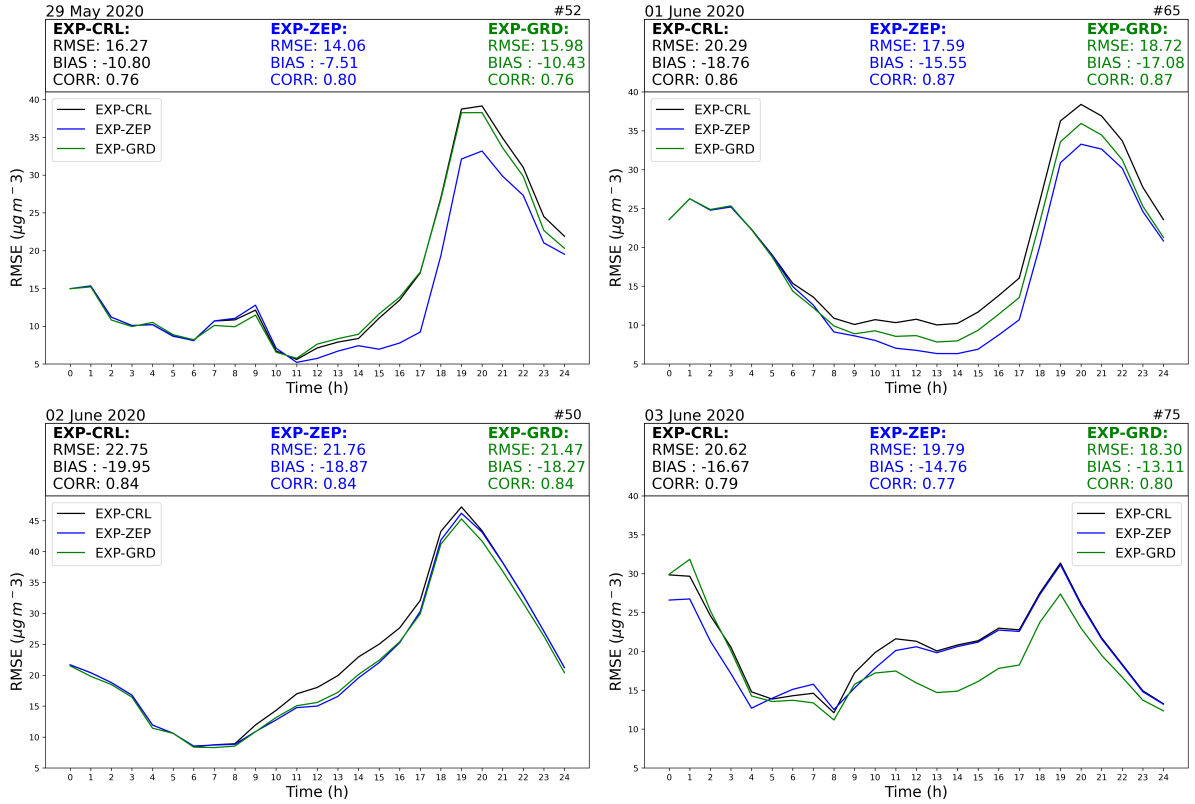

Figure 6.13: *Root mean square error (RMSE) for O_3 from all model simulations, based on comparison with independent ground-based observations over Belgium and the Netherlands for the four days considered.*

Discussion

The present case study shows that measurements during Zeppelin flights represent an effective tool for acquiring information on emissions and pollutant concentrations at high altitudes. Given the dense network of ground monitoring stations and their ability to provide continuous 24-hour measurements, assimilating ground data leads to better improvements compared to the Zeppelin data assimilation results. Nevertheless, Zeppelin data remains superior for optimising local emission sources and yielding better results for surface ozone concentrations within the data assimilation window. The key factor behind this is the high emission observability provided by the Zeppelin observations. The enhanced observability results from operating at relatively high altitudes (500 m on average) near the primary elevated power plants emission sources. The Zeppelin flew on the downwind side of these emission sources and thus intersected the emission plumes multiple times.

In contrast, ground-based observations generally have a limited impact on the overall 4D-Var analysis because the observability of emissions and pollutants at high altitudes is often restricted. However, the results show that the observability can increase in conditions of atmospheric instability and relatively strong winds at higher altitudes, as well as when the ground stations are positioned on the downwind side of strong emission source. A decrease in atmospheric stability led to more substantial vertical mixing, which enhanced the assimilation of ground observations.

6.2 Case study 2: The added value of the Zeppelin data assimilation

The objective of this section is to determine the added value of the Zeppelin observations when assimilated in the EURAD-IM 4D-Var system. To ensure that the analysis reflects a realistic daily scenario, this study uses the same simulation setup as outlined in the previous section 6.1. However, it employs the adjusted emission data for the year 2020 from the most recent inventory (CAMS-REG-v6.1) which accounts for the reductions due to the COVID-19 pandemic.

6.2.1 Simulation setup

The experimental setup from section 6.1.2 is employed, with two exceptions. Firstly, the adjusted emission data for 2020 are utilised for simulations with and without assimilation from 29 May to 03 June. Secondly, a continuous run is enabled from 01 June to 03 June. This implies that each day is initiated with the initial state and emission factors resulting from the previous days. For 29 May and 01 June, the simulations were initiated with emission factors of 1. The initial conditions of the simulations on 29 May are derived from the spin-up, which is calculated using the TNO-MACC_ II emissions data for the year 2016. Simulation assimilating Zeppelin data is denoted *EXP-ZEP*, while the one assimilating ground-based observations is denoted *EXP-GRD*. An additional simulation, *EXP-ALL*, is performed, which assimilates observations from both the Zeppelin and the ground-based stations (Table 6.3).

Table 6.3: *Details of simulation setups.*

Simulation	Number of Iterations	Assimilated Observations	Assimilation Window
EXP-CTR	-	-	-
EXP-ZEP	12	Observations of O_3, NO, NO_2, and CO from Zeppelin flights	From 00 UTC to the hour for which Zeppelin observations are available
EXP-GRD	10	Observations of O_3 and NO_2 from ground-based stations	24 hours
EXP-ALL	10	Observations of O_3, NO_2 and CO from ground-based stations + Zeppelin observations	24 hours

6.2.2 Assimilation performance

In this case study, the emission rates are assumed to be slightly inaccurate, as they exhibit daily variability that may not fully be captured in the inventory. Fig. 6.14 shows the difference between the optimised emission rates and the reference emission rates for the *EXP-GRD* and *EXP-ZEP* experiments during the 4 studied days. The *EXP-GRD* resulted in a marginal change between -0.1 t and +2.1 t on 29 May and between 0 t and +0.6 t on 01 June, while the *EXP-ZEP* corrected the emissions up to +12.8 t on 29 May and -9.2 t on 01 June. This change is mainly related to the power plants located in the study area (see Fig. 6.7). The results indicate that the assimilation of the Zeppelin observations has the strongest impact on the optimisation of emission rates on 29 May and 01 June. However, on 02 and 03 June *EXP-GRD* led to a much stronger correction than *EXP-ZEP*. While a slight decrease is noticed for *EXP-ZEP* in the power plants location (up to -2.1 t), *EXP-GRD* led to an increase of +5.8 t on 02 June and +27 t on 03 June. This discrepancy in the simulation results can be attributed to the variations

in wind conditions with respect to the location of the observations, as discussed in section 6.1 (Fig. 6.10).

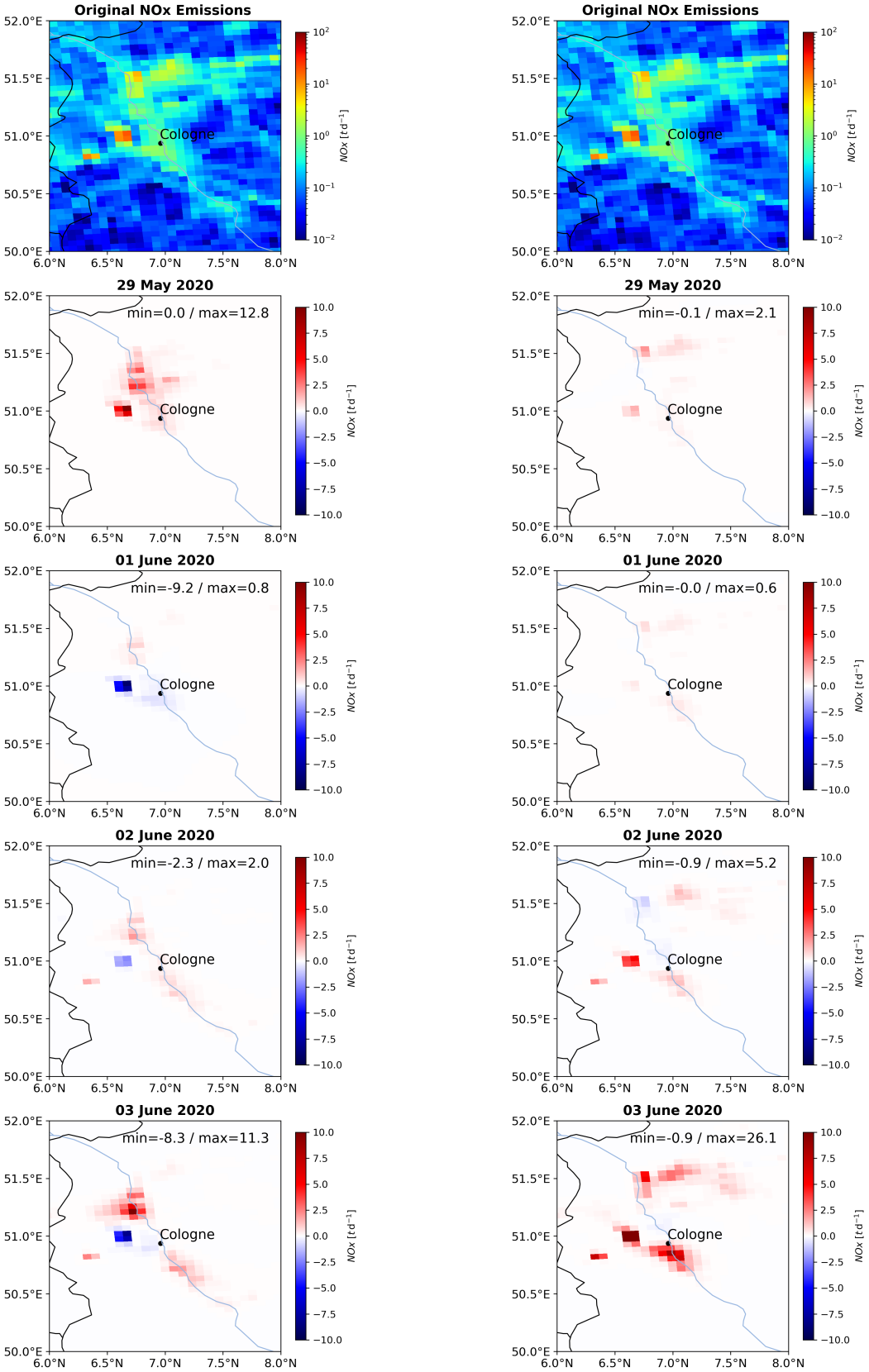

Figure 6.14: *Daily NO_x emissions of the inventory (top) and the analysed NO_x emission changes for each analysed day of 29 May, and 01-03 June 2020 (2-5 lines). The changes are shown for EXP-ZEP in the right panels and EXP-GRD in the left panels.*

Evaluation of the optimisation of initial values

In the present case study, it is assumed that the initial values (IVs) also contain errors that need to be corrected for a better analysis. The analysis increment, which represents the analysis minus the background, at the initial time step (t=0) is used for the evaluation of the correction made to the initial values. Figure 6.15 shows the O_3 increment at ground level and at an altitude of about 450 m (model level 11) for the two experiments *EXP-ZEP* and *EXP-GRD*. On 29 May, the increment of *EXP-ZEP* varies between -7 ppbv and 4 ppbv at ground level, while for *EXP-GRD* the increment is larger, between from -28 ppbv and 16 ppbv. On 01 and 02 June, a large increase up to 41 ppbv in the IVs is seen at ground level for *EXP-ZEP*, east of the location where the Zeppelin flew. On 03 June, this increment was analysed west of the Zeppelin flight region (up to 16 ppbv). The location of the IV increments is mainly controlled by the wind direction, such that the information about the model-observation discrepancy collected during the Zeppelin flights is transported to upwind surface regions by the adjoint model. For *EXP-GRD*, in contrast, the IV increment exhibits negative and positive changes (from -30 ppbv to 41 ppbv). Here, the increment location is associated with the positions of the assimilated ground observations.
Regarding the increment at 450 m altitude, *EXP-ZEP* results in a large increment (up to 45 ppbv) compared to *EXP-GRD*, which has an increment between -4 ppbv and 7 ppbv. Generally, the increments are situated at the same location and identify the same sign. This suggests that the assimilation of ground-based observations cannot significantly affect corrections for the atmospheric pollutants at altitudes of 450 m and higher. An increase of the initial values of ground-level O_3 will likely have a limited impact over time, because, in areas with high NO_x concentrations, the rise in O_3 levels tends to dissipate quickly overnight due to the NO_x titration process. This process affects NO_x and O_3 concentrations during the night rather than affecting daytime O_3 levels. In contrast, correcting O_3 at higher altitudes can have a more significant and longer lasting effect. Thus, the assimilation of Zeppelin observations has resulted in a more substantial correction of the initial conditions at higher altitudes.

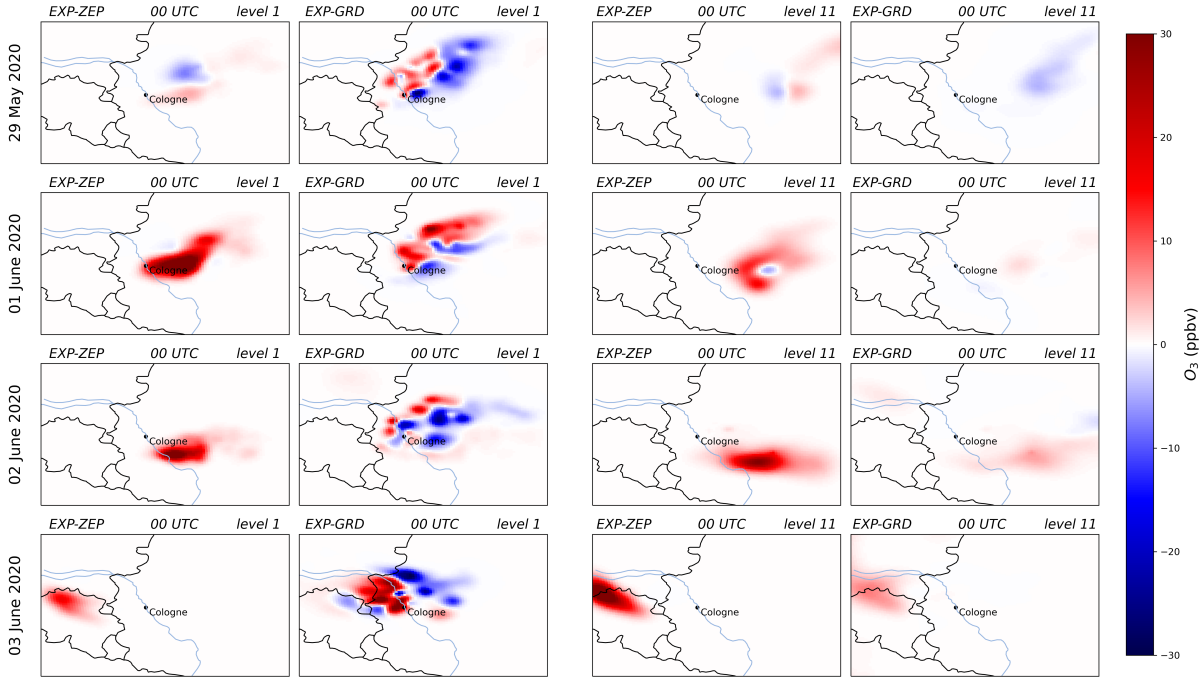

Figure 6.15: *O_3 analysis increment (analysis - background) at the initial timestep (00 UTC) for model level 1 (about 18 m) and model level 11 (about 450 m) for EXP-ZEP and EXP-GRD, shown for the four study days.*

Evaluation of 4D-Var analyses against independent observations

The performance of the model configurations using different data set for the assimilation is evaluated against independent ground-based observations. Fig. 6.16 shows the time series of O_3 RMSE for the four studied days for all simulations. Overall, the 24-hour RMSE analysis indicates that *EXP-ZEP* performs better than *EXP-GRD*. However, a distinct diurnal pattern is noticed: *EXP-ZEP* outperforms *EXP-GRD* during the daytime, whereas *EXP-GRD* exhibits superior performance at night hours. During the daytime (between 5 UTC and 19 UTC), the RMSE for *EXP-ZEP* is reduced by 31.05% on 29 May, 46.38% on 01 June, 54.08% on 02 June, and 24.55% on 03 June. In contrast, *EXP-GRD* reduced the RMSE by only 17.94%, 12.04%, 22.56%, and 19.87% compared to the background simulations on the same respective days.
At night, *EXP-GRD* proved to be more effective in reducing the RMSE. Specifically, the RMSE reductions of 20.29%, 16.09%, 14.21%, and 11.38% were obtained on 29 May, 01 June, 02 June, and 03 June, respectively. In contrast, *EXP-ZEP* showed only minor reductions of 2.08% on 29 May and 6.86% on 02 June, while the RMSE increased by 5.87% on 01 June and 2.14% on 03 June.
The best model performance is attributed to the *EXP-ALL* experiment, in which both types of observations are assimilated simultaneously. *EXP-ALL* consistently demonstrates superior performance, outperforming *EXP-GRD* at night and *EXP-ZEP* during the daytime. For instance, on 03 June, *EXP-ALL* achieved an additional RMSE reduction of 2 $\mu g\,m^{-3}$ (6.15%) during the daytime compared to *EXP-ZEP*, and a reduction of 1.3 $\mu g\,m^{-3}$ (6.79%) at night relative to *EXP-GRD*. A distinct case is identified on 03 June, where *EXP-GRD* shows better RMSE reduction compared to other simulations from 13 UTC onwards. By relating this performance

to the evaluation of emission rates and initial values optimisation, there is evidence that the analysis using ground station observations profits from advantageous observability with respect to emissions. This is enabled by the prevailing westerly winds on that day. The influence of assimilated Zeppelin observations appears to be limited due to their timely restricted availability and the reduced assimilation window, leading the analysis of *EXP-ZEP* to gradually converge to the *EXP-CTR* at the end of the day.
In conclusion, the 4D-Var assimilation of both types of observations provides improved the model performance compared to the control simulations. The results demonstrate the potential of the Zeppelin observations in improving the daytime O_3 analysis.

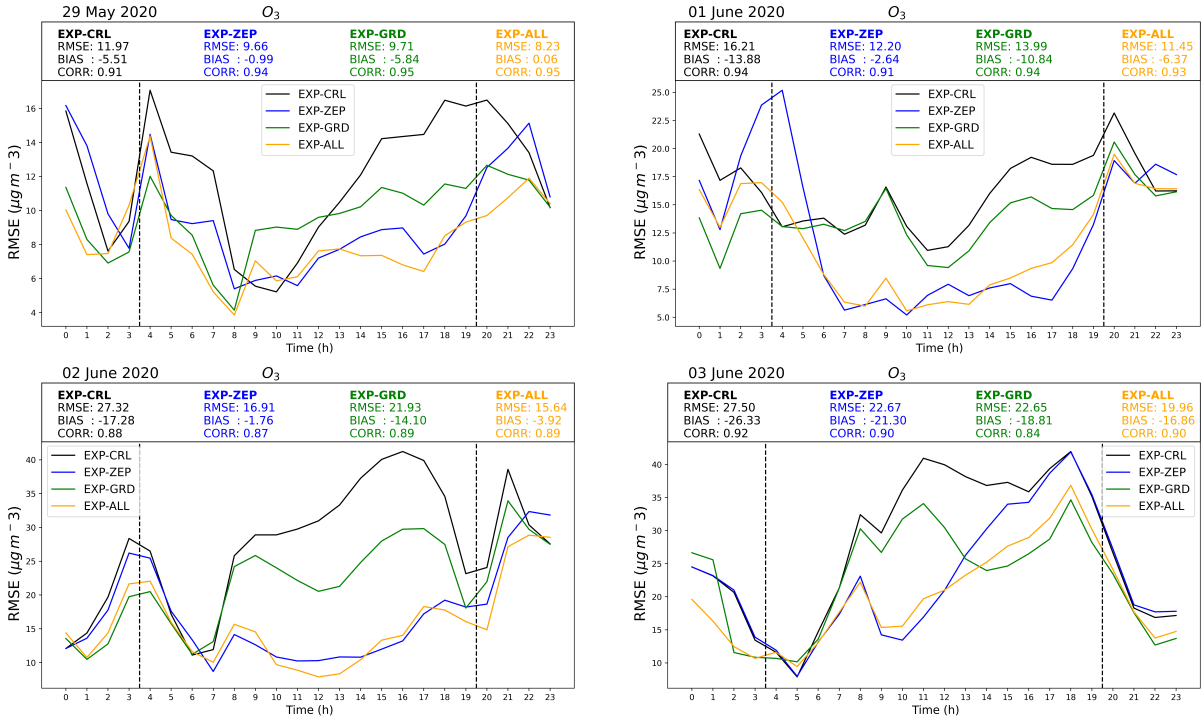

Figure 6.16: *Root mean square error (RMSE) of O_3 for all simulations, averaged over all validation stations, for the four days of the study.*

The added value of the Zeppelin observations

To gain more insight into the additional contribution of the Zeppelin observations and to understand the limitations of the ground-based observations, a detailed evaluation of the simulations' performances is carried out. This evaluation focuses on the O_3 concentrations at a monitoring station, for which the atmospheric composition was corrected in all assimilation simulations. Fig. 6.17 presents the observed and model predicted O_3 concentration from all experiments for the day of 02 June at one ground-based station in Mönchengladbach. This station is located in the area where the Zeppelin observations were made. Although the observations from this station have been assimilated in *EXP-GRD*, the O_3 concentrations during the day are not well predicted. In contrast, *EXP-ZEP* predicts an O_3 concentration that remarkably reproduces the observed rapid increase and the high surface O_3 concentration from 6 UTC onwards. The

strong agreement between the 4D-Var analysis from *EXP-ZEP* and observations suggests that O_3 production by photolysis as well as the vertical mixing are accurately represented. This is on the one hand due to the precise estimation of local O_3 precursors, NO_x and VOCs, and on the other hand due to the improvement of initial O_3 concentrations at higher altitudes (See Fig. 6.15). Furthermore, the results indicate that the model effectively captures the evolution of the PBL height, facilitating the vertical mixing of O_3. The evident underestimation of O_3 by *EXP-GRD* during the daytime suggests that photolysis alone cannot account for the observed high O_3 levels. The O_3 transport from upwind regions and higher altitudes can play a major role in shaping the observed O_3 levels at this location. Several studies (Pay et al., 2019; Kaser et al., 2017; Hu et al., 2018) have shown that elevated concentrations of O_3 are often derived from the background levels and emissions of precursors in upwind regions and subsequently horizontally transported.

Figure 6.18 shows a time-height plot of the O_3 analysis increment at the same station for all three analysis simulations. A strong positive increment is obtained for *EXP-ZEP* at higher altitudes, peaking within the residual layer. This indicates that the assimilation of Zeppelin observations leads to an increase in the O_3 concentrations at higher altitudes (between 1500 m and 2500 m). High O_3 levels in the residual layer are generally attributed to accumulated O_3 from previous days and to the long-range advection from upwind areas. In the case of *EXP-GRD*, only a small increment is present near the ground with almost no signal at higher altitudes. This indicates that information of ground level observations is not efficiently mixed into higher model levels during the adjoint integration, highlighting the need for upper-air observations. When both types of observations are assimilated in *EXP-ALL*, the increment combined the effects of the two individual experiments, *EXP-GRD* and *EXP-ZEP*, with more impact from *EXP-GRD* during the night and *EXP-ZEP* during daytime. In *EXP-ZEP*, the correction of surface observations was achieved through the adjustment of O_3 concentrations in the residual layer. As the PBL evolves over time, O_3 stored in the residual layer is progressively entrained into the PBL, influencing surface concentrations through vertical mixing. In contrast, *EXP-GRD* did not produce a sufficient correction of surface O_3, even though the O_3 initial value corrections at the station's location were larger. These findings are consistent with recent studies, which have demonstrated that the vertical exchange of O_3 between the residual layer or the free atmosphere with the PBL mixing layer plays a major role in the rapid increase of near surface O_3.

The assimilation of Zeppelin observations improved the analysis by enhancing the O_3 background in the residual layer, enabling a more accurate correction of daytime O_3 through vertical exchange with the PBL. This highlights the critical role of PBL observations in refining the 4D-Var analysis, an improvement not achievable with ground-based data alone.

Discussion

This case study focuses on investigating the added value of Zeppelin data assimilation to improve the air quality simulations. The results reveal that the assimilation of Zeppelin observations leads to better emission rate optimisation and improved initial conditions compared to other assimilation simulations. Zeppelin assimilation positively impacted daytime ozone concentrations, whereas ground-based assimilation proved more effective during nighttime hours. The latter could be expected, as the Zeppelin did not operate during nighttime. Simulations that combined both types of observations produced the most accurate results overall. This conclu-

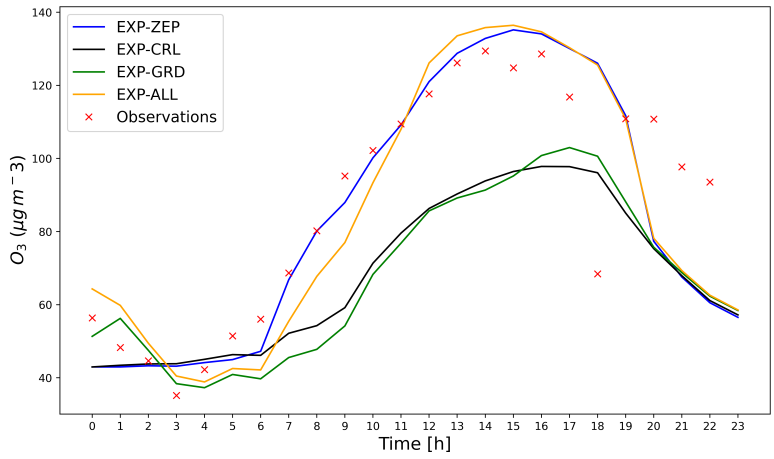

Figure 6.17: *Evolution of O_3 concentrations at the DENW096 station in Mönchengladbach in comparison with the model predictions for all simulation experiments on 02 June 2020.*

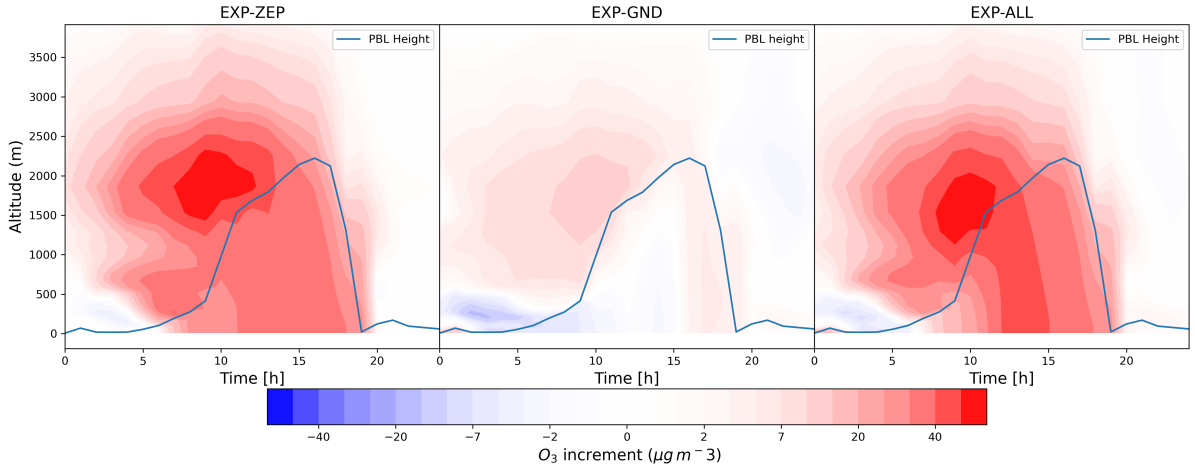

Figure 6.18: *The time-height analysis increment of O_3 at station DENW096 on 02 June 2020. The blue line indicates the height of the planetary boundary layer.*

sion is particularly significant as it highlights the necessity of integrating both airborne and ground-based observations to achieve the best model performance.
The key result here is that the enhancement in the vertical distribution of ozone is primarily attributed to the improved representation of ozone concentrations within the residual layer. This layer serves as a reservoir of ozone, either accumulating ozone from previous days or transporting ozone or its precursors from upwind regions. During the daytime, the evolution of the PBL results in vertical mixing, which is critical in regulating ozone concentrations near the surface. In contrast, ground-based observations are limited in their ability to influence the upper layers and the top of the PBL, which also constrains the improvement of the vertical distribution within the PBL.
The primary added value of Zeppelin observations lies in their capacity to refine the vertical distribution of pollutants within both the PBL and the residual layer. This improvement in particular affects the accuracy of surface ozone concentrations. Zeppelin observations are par-

ticularly valuable during episodes when elevated ozone from the upper atmospheric layers is transported long-range and mixed downward into the PBL due to vertical exchange processes between the upper layers and the PBL.

6.3 Case study 3: Limitations of the Zeppelin data assimilation

The previous section highlighted the additional benefits of the Zeppelin data assimilation. In this section, the aim is to explore the limitations of this assimilation to develop a comprehensive understanding of the potential of Zeppelin observations and, consequently, of observations within the PBL. To achieve this, the Frankfurt region has been selected for analysis. This choice is motivated by the aim to evaluate the impact of the assimilation of Zeppelin observations in a region with different emission characteristics. While North Rhine-Westphalia is characterised by high emissions from power plants and industrial activities that emit at high altitudes, Frankfurt has comparatively much lower emissions from these sectors. The urban area is more dominated by surface emissions from transport-related sectors, including aviation.

The present study covers the period from 11 to 13 September 2020. During these three days, the Zeppelin conducted continuous measurement flights over the Frankfurt region (see Fig. 6.19), performing more than nine round trips daily between 07:00 and 17:00 UTC. The objective of this study is to evaluate the ability of Zeppelin to detect the distribution of urban pollutant concentrations in the PBL. In addition, emphasis will be placed on evaluating the improvements achieved through 4D-Var assimilation of Zeppelin observations and identifying any potential limitations.

Figure 6.19: *Flight path of the Zeppelin over Frankfurt on 11 September 2020..*

6.3.1 Meteorological conditions

From 11 to 13 September 2020, persistent high-pressure systems dominated the atmospheric circulation in central and eastern Europe (Fig. 6.20). The high-pressure system over Germany helped to maintain stable weather conditions, particularly in the southern and eastern regions. Temperatures rose above 28 °C at the surface for the three studied consecutive days, accompanied by low wind speeds. Such conditions are favourable for the development of ozone pollution.

Table 6.4: *Details of simulation setups for the investigation of the Frankfurt Zeppelin campaign on 11-13 September 2020.*

Simulation	Number of Iterations	Assimilated Observations	Assimilation Window
EXP-CTR	-	-	-
EXP-ZEP	10	Zeppelin observations (O_3, NO, NO_2, and CO)	00 UTC - 17 UTC
EXP-GRD	10	Ground-based observations (O_3, NO_2 and CO)	24 hours
EXP-ALL	10	Ground-based observations (O_3, NO_2 and CO) + Zeppelin observations (O_3, NO, NO_2, and CO)	24 hours

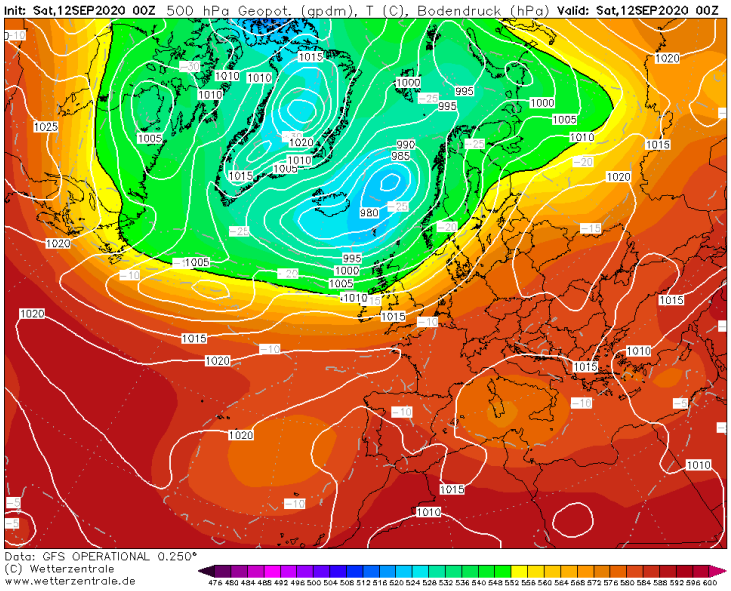

Figure 6.20: *500 hPa geopotential height (in gpdm, colour-coded) and surface pressure (in hPa, white lines) over Europe on 12 September 2020 at 00 UTC from GFS reanalysis data (`www.Wetterzentrale.de`). The black line indicates the 552 gpdm contour.*

6.3.2 Simulation setup

To investigate the gain of observational information from Zeppelin based measurements for an air quality analysis, a similar study to section 6.2 was performed for the region of Frankfurt, where the Zeppelin performed daily measurement flights from 11 to 13 September 2020. Four simulation experiments were performed for all three days of this campaign: one control simulation without data assimilation and three applying the 4D-Var of EURAD-IM. The horizontal resolution of the model grids was selected to be 5 km x 5 km, implicating a temporal resolution of 60 s. In all assimilation experiments, initial values and emission rates were jointly optimised. Table 6.4 outlines the observations employed in each scenario, the assimilation windows, and the simulation details.

The simulations are conducted continuously, such that the initial conditions and emission rates of day n are used to simulate the following day n+1. The model is initialised from a climatological chemical state with a 10-day spin-up simulation (1-10 September 2020) to ensure a chemically balanced initial state. The spin-up was conducted with business-as-usual emissions, while the three-day simulations were carried out with adjusted 2020 emission rates.

6.3.3 Comparison between simulated and observed data

The comparison between observed values and the background model estimates allows for a comprehensive assessment of the model's performance. Model biases can be identified by directly evaluating the differences between an observation and the equivalent modelled value. The Figures 6.21 and 6.22 show the time-height profiles of O_3 and NO_2 concentrations simulated by EURAD-IM along the flight tracks of the Zeppelin on 11-13 September 2020, respectively. The time–height profiles of NO are shown in Fig. A.7 in the appendix. The corresponding Zeppelin observations are included as well as the WRF model derived PBL height. The observed values have been averaged over 60-second intervals to align with the model's temporal resolution. The Zeppelin flights primarily occurred within the mixing layer of the PBL, except for measurements conducted before 10 UTC on 12 and 13 September (Fig. 6.21 c, d), when the Zeppelin briefly ascended a few hundred meters into the residual layer above the PBL.

In Fig. 6.21, the O_3 concentrations in the residual layer are underestimated by the model. The mean absolute difference between observed and modelled O_3 concentrations in the residual layer is 17.57 ppbv on 12 September and 13.19 ppbv on 13 September. However, in the lowest 100 m during the first 3 hours, the Zeppelin observations are in better agreement with the model, with a mean absolute difference of 6.5 ppbv on 12 September and 4.1 ppbv on 13 September. The model has performed relatively well in representing the O_3 concentrations within the PBL during the morning hours. Nevertheless, it struggles to accurately represent concentrations in the residual layer, likely due to suboptimal O_3 representation from the previous day or the incorrect vertical distribution of anthropogenic emissions of its precursors. The PBL height agrees well between observations and EURAD-IM, when analysing the change of pollutant concentrations with height. These findings emphasise the effectiveness of Zeppelin observations in capturing the layered structure of the PBL and their ability to monitor the lower troposphere. In the mixing layer, the model largely underestimated the O_3 concentrations across all analysed days. On 11 September, the O_3 mean absolute difference between model and observations is 5.31 ppbv, increasing to 8.31 ppbv in the afternoon (after 12 UTC). The afternoon mean absolute difference grows to 17.04 ppbv on 12 September and 18.64 ppbv on 13 September. This indicates that the model does not reproduce the high O_3 concentration measured in the PBL during the midday and afternoon. Furthermore, the underestimation becomes more pronounced each day as the O_3 concentrations rise.

As shown in Fig. 6.22, the model underestimates NO_2 concentrations on 11 and 13 September although to a lesser extend than it was for O3. The mean absolute observation minus background difference is 2.33 ppbv on 11 September and 2.83 ppbv on 12 September. The underestimation is more pronounced before 12 UTC, reaching 3.4 ppbv and 4.3 ppbv, respectively. In the afternoon, the discrepancies decrease, with mean absolute differences of 0.97 ppbv on 11 September and 1.19 ppbv on 12 September. The high concentrations of NO_2 on 12 September during the morning are not well represented by the model during these two days. This discrepancy may be attributed to poorly represented emission rates, unresolved emission sources due to the model resolution, or the underestimation of O_3 levels. Additionally, on 12 September between 09:30 and 11 UTC, substantial mean absolute differences of up to 18.2 ppbv are seen at approximately 300 m altitude. This suggests that the model fails to resolve local emission plumes.

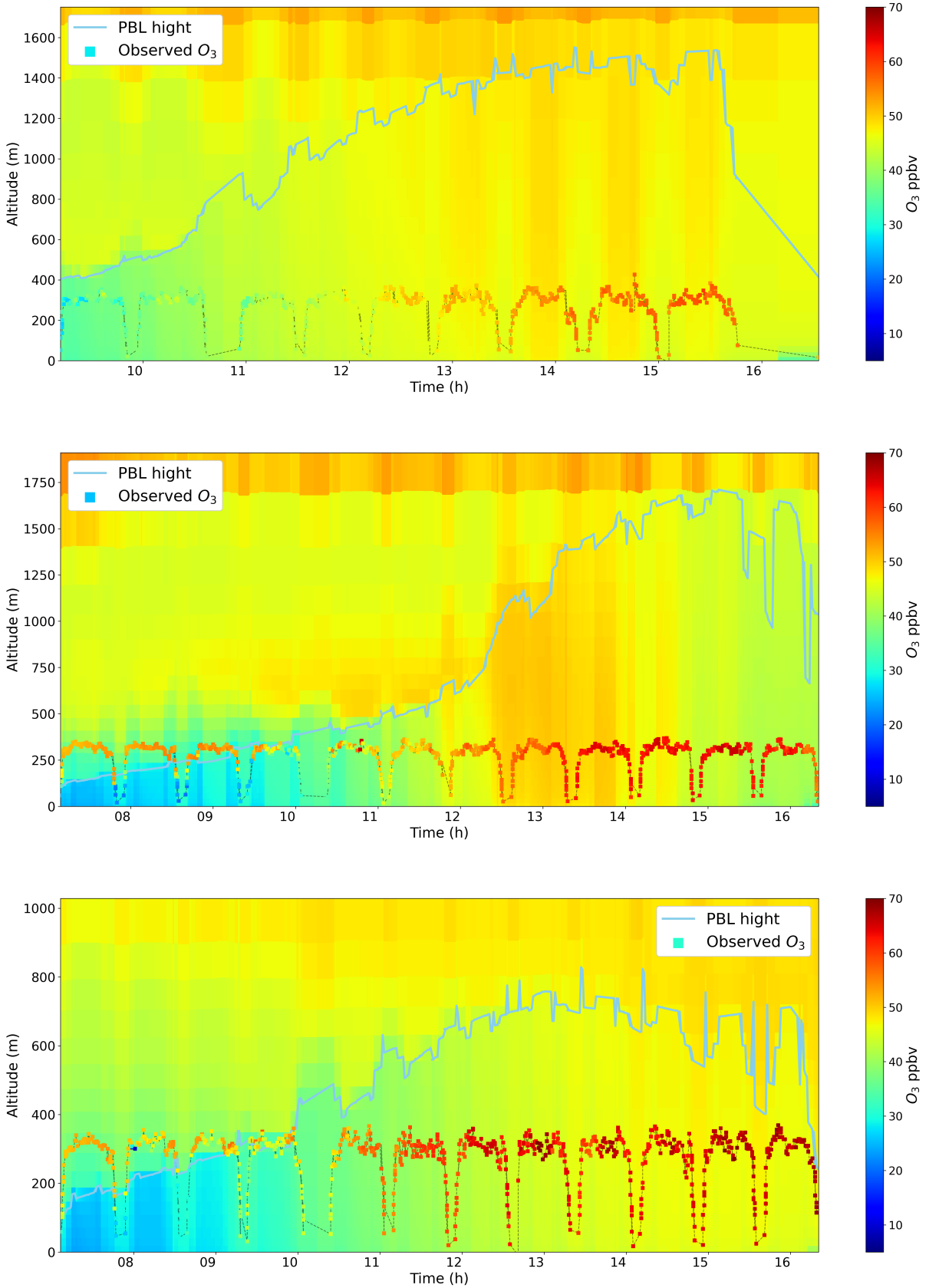

Figure 6.21: *Time series of O_3 observations from the Zeppelin as a function of altitude for 11 September 2020 (top), 12 September 2020 (middle), and 13 September 2020 (bottom), with model predictions from the reference simulation (without assimilation) shown in the background. The PBL height calculated by the model is indicated by the blue line.*

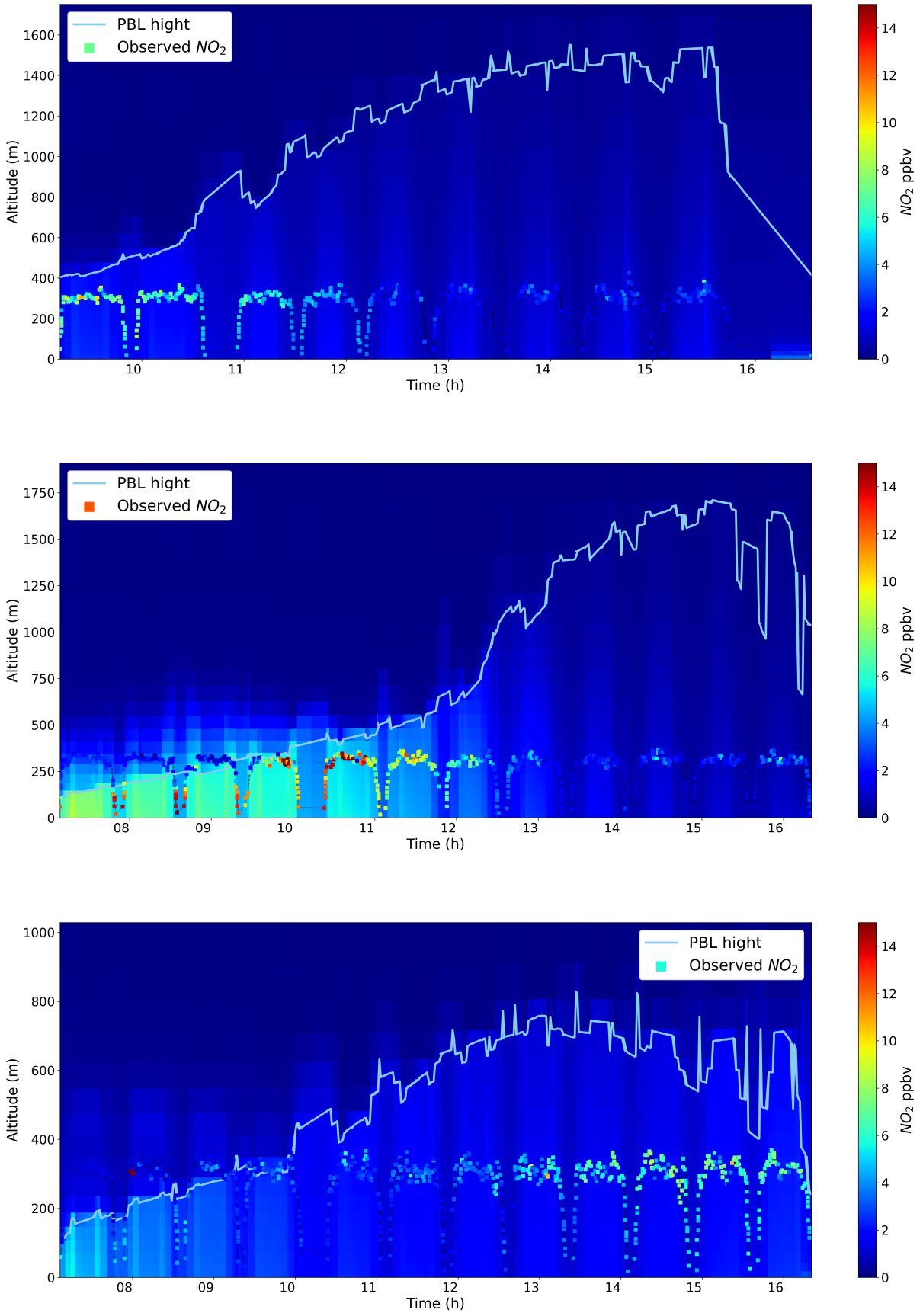

Figure 6.22: *Same as Fig. 6.21, but for NO_2.*

6.3.4 Assimilation results

Evaluation against Zeppelin observations

Comparing the results of 4D-Var assimilation with the assimilated observations helps to evaluate how effectively the system integrate the observed data and enhances model accuracy. Figures 6.23 and 6.24 show scatter-plots comparing the model results with the Zeppelin observations of O_3 and NO_2, colour-coded by time for the three studied days (11-13 September). Here, the objective of the assimilation analysis is not that the model perfectly reproduces the observed pollutant concentration values but to obtain the optimal fit between the model background and the observations, taking background and observation errors into account. The assimilation process has considerably reduced the difference between the model and the observations for O_3 by more than 60%. The RMSE decreased from 6.51 ppbv to 2.49 ppbv on 11 September, from 15.32 ppbv to 5.67 ppbv on 12 September, and from 17.36 ppbv to 6.13 ppbv on 13 September. An improvement in the correlation was obtained on 11 September, when the assimilation improved the correlation from 0.86 to 0.96, indicating an almost perfect agreement between the observations and the model. However, on 12 and 13 September, several data points are further away from the 1:1 line after the assimilation process. These data points are collected within the PBL between 7 UTC and 12 UTC in the PBL. This suggests that the assimilation process overestimates O_3 values within the PBL. In contrast, the analysis well represents the O_3 concentrations in the morning and afternoons in the residual layer. These results indicate an improvement in the representation of O_3 levels during the afternoon and the residual layer. However, the decline of model observation agreement found in the early hours of the day requires further analysis to gain a complete understanding.

An improvement in the simulation performance of NO_2 concentration is achieved due to the assimilation of the Zeppelin observations. The RMSE decreased from 2.99 ppbv to 1.19 ppbv on 11 September, from 3.68 ppbv to 2.80 ppbv on 12 September, and from 3.44 ppbv to 2.06 ppbv on 13 September. However, after the assimilation, the model did not effectively reproduce high NO_2 concentrations within the PBL on 12 September and outside the PBL on 13 September. These high NO_2 concentrations were likely linked to local emission plumes. The limitation is attributed to the resolution of the model, which may not be sufficient to accurately represent and optimise local emission sources.

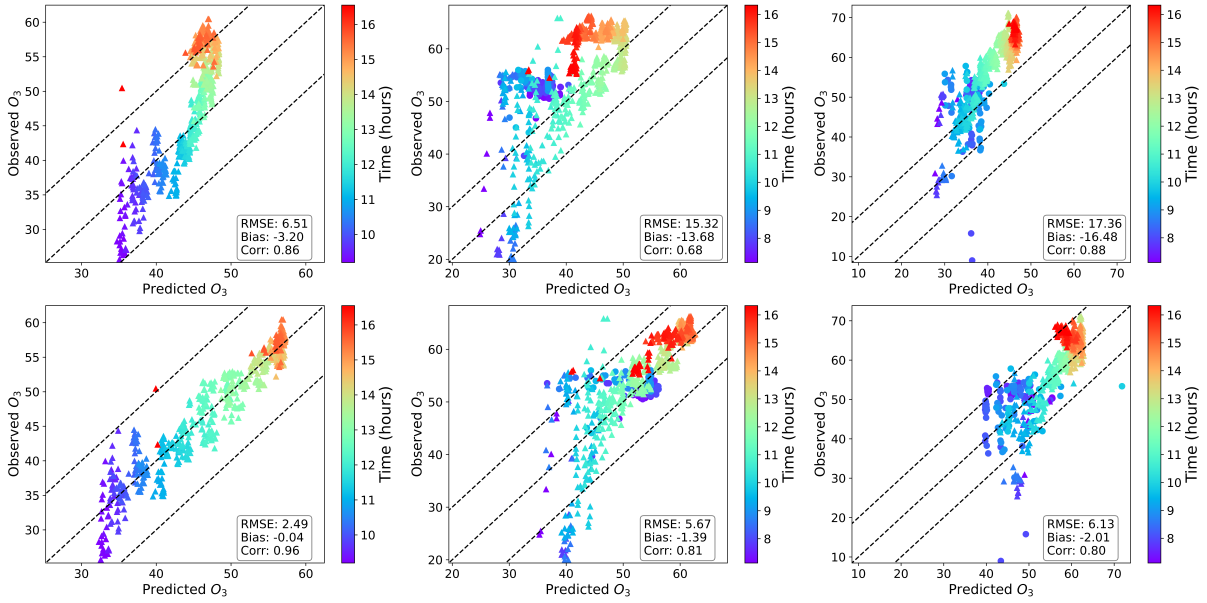

Figure 6.23: *Scatter plots of predicted versus observed data for O_3 from the Zeppelin flight on 11-13 September 2020 (from left to right). Observations are compared with model data from the reference simulation(top) and EXP-ZEP (bottom). Circle markers represent points within the residual layer, while triangle markers indicate points within the PBL.*

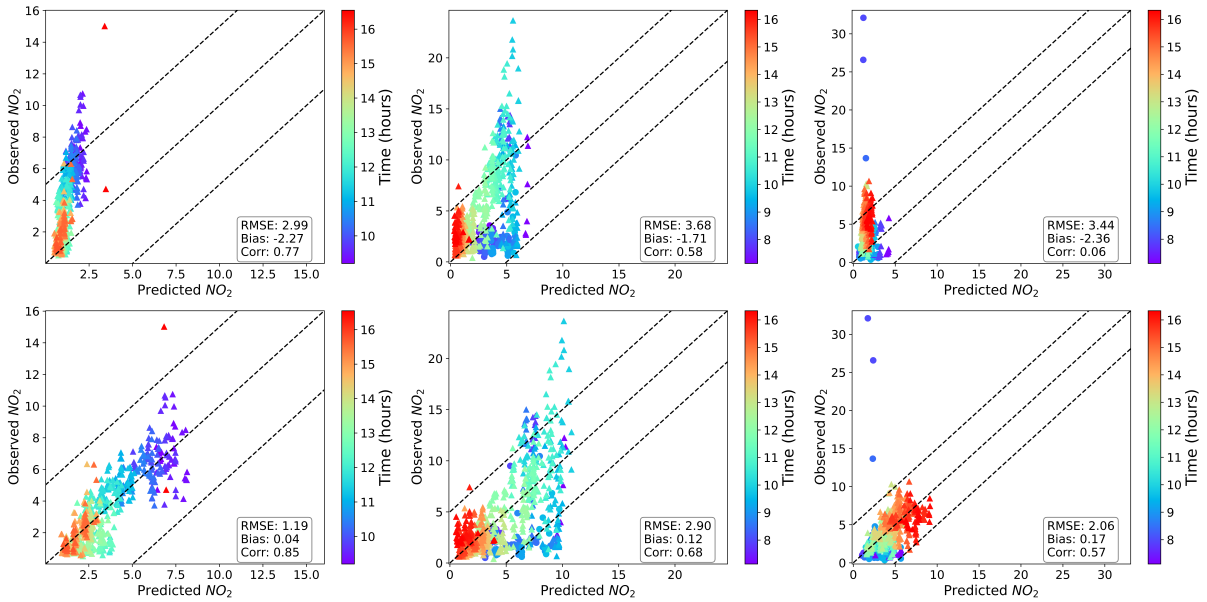

Figure 6.24: *Scatter plots of predicted versus observed data for NO_2 from the Zeppelin flight on 11-13 September 2020 (from left to right). Observations are compared with model data from the reference simulation (top) and EXP-ZEP (bottom). Circle markers represent points within the residual layer, while triangle markers indicate points within the PBL.*

Simulations performance

The model simulation results were compared with independent observations from ground-based stations to validate the impact of Zeppelin data assimilation. Furthermore, the analysis assimilating the Zeppelin observations was compared to the results from the ground-based data assimilation, as well as to the analysis that included both types of observations. Thus, the added value and potential limitation of the Zeppelin observations can be assessed in the urban area of Frankfurt and its surrounding environment. The validation stations are divided into four categories: suburban, traffic, rural, and remote. The region of validation is illustrated in Fig. A.8.

Figures 6.25, 6.26 and 6.27 presents the hourly RMSE for O_3, NO and NO_2, respectively, per station type for all simulations and across the three analysed days. For O_3, the *EXP-ZEP* performs best for O_3 during daytime, while *EXP-GRD* performs better at night. An exception is noted for remote and mountain stations during the night hours at the end of the day, where *EXP-ZEP* shows better correction for O_3 compared to *EXP-GRD*. This indicate that the representation of O_3 was improved in elevated altitudes.

For NO, a minimal RMSE reduction is observed for all simulations. The best performance is noted for *EXP-GRD*, except for suburban stations on 13 September, where *EXP-ALL* is slightly better. The model effectively predicts the low NO concentrations at most monitoring stations. However, during rush hours, the model struggles to accurately represent the high concentrations derived because of traffic transport emissions. This limitation is likely due to the model's resolution. A decrease of the RMSE is seen for the case of NO_2, with the best performance noted for *EXP-GRD* and *EXP-ALL*.

However, for suburban and traffic stations on 13 September, the significant improvement in RMSE for O_3 during daytime in the *EXP-ZEP* experiment is accompanied by a notable increase in RMSE during the night and the early morning, late afternoon, and nighttime, compared to the control simulation. Similar patters is also seen NO_2. Several reasons can be responsible for the failure of the model to accurately represent the O_3 and NO_2 ground concentrations on 13 September. The first reason to consider is the PBL height. On 13 September, the PBL height, as modelled by the WRF model, was very low, limited to only 800 m in the area of the measurement campaign location. As presented in Fig. 6.21, by crossing the PBL top, the Zeppelin observations captured the PBL structure as it is modelled, indicating that it was likely well represented between 7 UTC and 10 UTC. However, during midday and the afternoon, the PBL height may have been underestimated. As discussed in the previous section, vertical mixing with the residual layer drives the increase in O_3 concentrations during daytime. However, given the shallow PBL, the vertical mixing is low, which limits the exchange process. Therefore, the exchange process with the residual layer is insufficient to increase the O_3 to the observed levels. This suggests that the PBL height, in reality, likely exceeded 800 m. As a result, the model increased O_3 levels during the *EXP-ZEP* in the early morning to compensate for this issue. The second possible cause for the insufficient correction of O_3 is the misrepresentation of O_3 precursor emissions and Volatile Organic Compounds (VOCs) concentrations. Since NO concentrations were very low, an overestimation of VOCs could have led to the formation of peroxy radicals (RO_2). These radicals react with NO, competing with the reaction between O_3 and nitrogen oxides, which either reduces the O_3 destruction or leads to the accumulation of both O_3 and NO_2 . In addition, the poor prediction of NO peaks in the morning between 4

UTC and 7 UTC, may be responsible for the overestimation of O_3. A high NO concentrations during this time could have helped to reduce O_3 levels by generating NO_2, which would then enhance the photolysis of O_3 in the presence of sunlight. Improving the model spatio-temporal resolution, particularly for urban modelling, would allow for a better representation of NO_x and, consequently, O_3 levels.

Discussion

This study aims to evaluate the impact of Zeppelin data assimilation on air quality analyses in an urban environment. The findings suggest that the Zeppelin observations have a strong capability to monitor the air in PBL, thereby providing valuable information on the vertical distribution of pollutants and the temporal evolution of pollutant concentrations. The assimilation of these observations allows for a significant improvement in surface ozone concentrations during daytime periods, with better accuracy compared to the other assimilation experiments. However, degradation of the analysis during the nighttime was also noted, primarily occurring at suburban and traffic monitoring stations during nighttime and early morning hours, particularly on 13 September when the boundary layer height was shallow. Therefore, using Zeppelin observations for data assimilation over urban and suburban areas should be accompanied by the assimilation of ground-based observations during the night. Those observations significantly helped the data assimilation system to constrain the modelled atmospheric state towards the optimal solution.

In conclusion, Zeppelin data assimilation demonstrates a high potential to improve air quality analyses, particularly within strongly polluted environments. Still, various factors can limit the impact beyond the data assimilation window, especially during nighttime. These factors include on the one hand observation related limitations, as for example the limitation of available Zeppelin observations to day time flight operations, and on the other hand model constraints, as the model resolution, hard to evaluate meteorological parameters (e.g. PBL height), or the difficulty to well represent pollutants that are not observed.

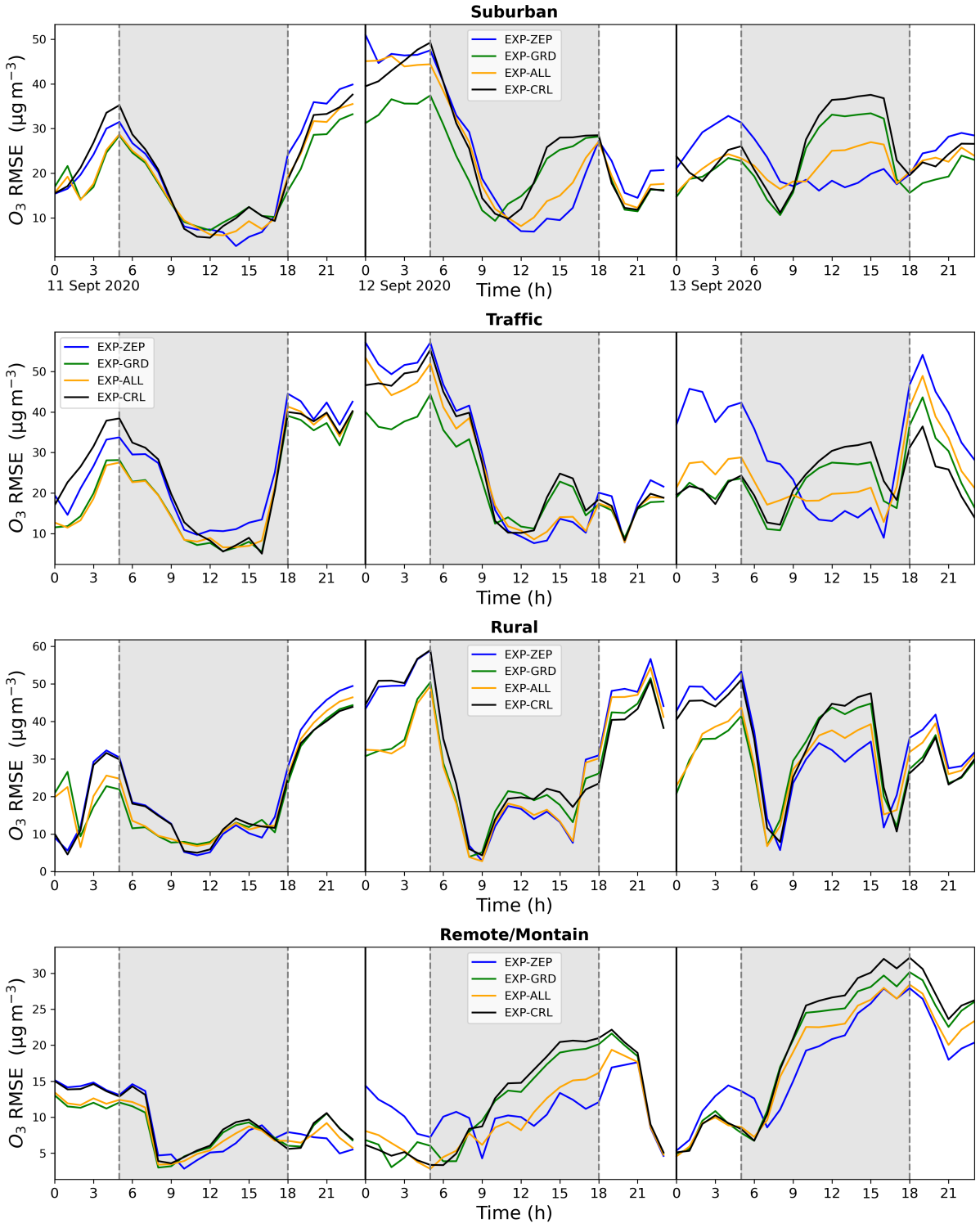

Figure 6.25: *Hourly RMSE of O_3 concentrations for all simulations across four types of monitoring stations. The grey area represent the daytime period.*

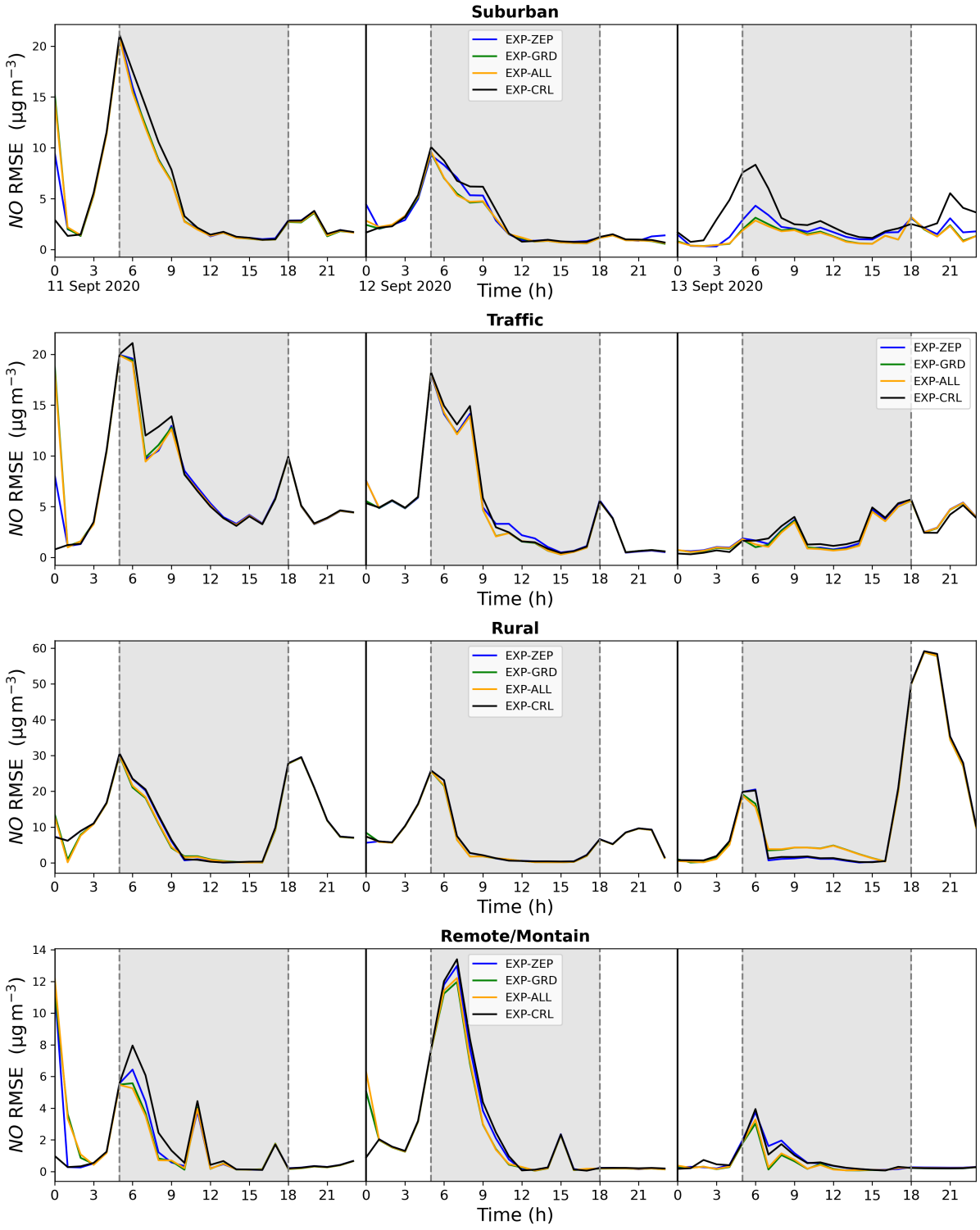

Figure 6.26: *Hourly RMSE of NO concentrations for all simulations across four types of monitoring stations. The grey area represent the daytime period.*

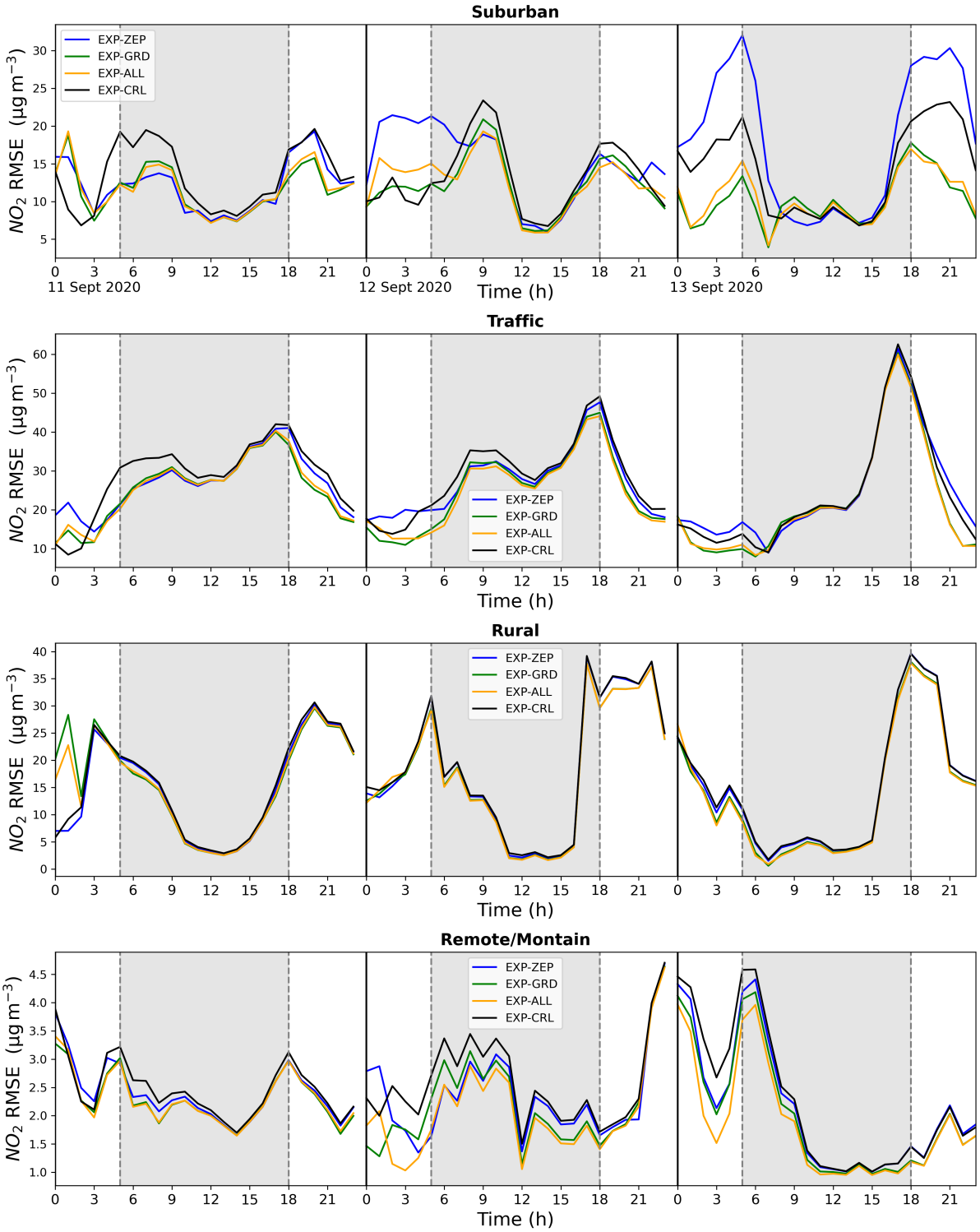

Figure 6.27: *Hourly RMSE of NO_2 concentrations for all simulations across four types of monitoring stations. The grey area represent the daytime period.*

7

Conclusion and Outlook

An observation gap exists in the planetary boundary layer (PBL) due to a lack of data within the lowest 1 to 2 kilometres of the atmosphere above the ground. However, observations of the dynamically active PBL are of great interest as they provide information on the horizontal and vertical distribution of pollutants in the lower troposphere. The main objective of this study is to investigate the potential and limitation of assimilating in situ airborne observations within the PBL to regional air quality analyses. The airborne observations evaluated here are recorded on drone and Zeppelin platforms.

Drone observations offer a promising solution to fill the observation gap in existing air quality monitoring infrastructures. While several drone measurement campaigns with the aim to characterise the vertical structure of meteorological and pollutant parameters have been conducted over the past decade, no modelling studies exist that utilised a chemical transport model to assess the possible impact of the assimilation of these observations. Therefore, the first part of the thesis aimed to investigate the potential of drone observations to improve regional air quality analyses. To achieve this, the EURAD-IM 4D-Var data assimilation system was used, employing a combined approach that optimises initial values and emission correction factors. The vertical profiles of ozone (O_3) and nitrogen oxide (NO) collected by a quadcopter drone during a two-day campaign were assimilated. The results show that the 4D-Var assimilation of the drone measurements positively impacts the representation of pollutants within the PBL and even at the ground in the widespread area around the campaign location. The vertical profiles of O_3 and NO concentrations overall improved in the analysis compared to the reference simulation without assimilation. A comparison with independent observations from ground-based stations at the campaign location revealed a remarkable correction of the surface concentrations of O_3 and NO during the early hours of the day and throughout the assimilation window. This positive impact of O_3 and nitrogen dioxide NO_2 ground-level concentrations propagated to locations more distant to the measurement site due to the corrected initial values and emission rates. The emission correction factors were identified as driver for the analysis improvements. This underlines that profile measurements within the lowest 350 m of the atmosphere have a great potential for capturing pollutants that can be attributed to emission corrections and thus improving air quality predictions. Although the drones were just equipped with low cost

sensors, the information obtained is beneficial for initial value and emission factor optimisation.

To draw broader conclusions about the impact of measurements in the PBL on air quality analyses, additional data are required. However, the drone campaign provided only two days of successful measurement acquisition, which limits the statistical significance of the results. For this reason, Zeppelin observations were additionally considered for an assimilation study. In contrast to the drones, the Zeppelin did not simply measure vertical profiles but also collected data during prolonged flights within a few hundred meters altitude and thus observed pollutants in the PBL across larger areas.

The potential of the Zeppelin observations to enhance the air quality analysis was examined through three case studies. In the first case, the realistic, yet extreme scenario for the year 2020 was considered, using emissions inventory that are highly uncertain because of the COVID-19 pandemic. The results showed that Zeppelin observations generally provide information for reliable emission rate optimisation. In particular, emissions from the power plant sector can be optimised well, as power plants mainly exhaust above a chimney height within the first hundreds of meters in altitude. This sector assignment was confirmed by the satellite observations in the study. Achieving similar performance in emission optimisation with ground-based observations is challenging due to the limitations in the observability of emissions. The investigation revealed that wind strength and direction, combined with the location of ground stations relative to emissions sources, control the observability of emissions emitted in elevated altitudes. Therefore, it was only possible to achieve similar emission optimisation results when the assimilated ground-based observations were located downwind of the local emission sources and with the presence of sufficiently strong winds. The validation against independent ground-based observations distributed in the study region allowed for the evaluation of the model analysis performance. The 4D-Var assimilation of Zeppelin observations has substantially improved the O_3 analysis, particularly within the assimilation window. A key result of this study is that the impact of Zeppelin data assimilation was generally more beneficial than the impact of ground-based data assimilation. However, the effect of the assimilation was influenced by the length of the assimilation window, the distribution of the observations, and their location relative to the emissions sources.

In the second case, another emission scenario was considered for the simulations, using an adjusted emission inventory that improved the emissions for 2020 by considering the emission reduction due to the COVID-19 lockdown. A comparison with independent observations demonstrated that the assimilation of Zeppelin observations resulted in an improved analysis of O_3 concentrations during daytime. In contrast, the assimilation of ground-based observations performed better at night hours. The overall analysis performance was best when observations from Zeppelin and ground-based stations were jointly assimilated. Here, the daytime improvements of O_3 were linked to the correction made to the initial values of O_3 concentrations in the residual layer. The resulting increase of surface O_3 concentrations was obtained due to the vertical mixing and exchange between the PBL and the residual layer. The adjustment of O_3 in the residual layer was less pronounced when only ground-based observations were assimilated, indicating that these observations have limited influence in higher altitudes.

The third case study evaluates the potential of Zeppelin observations in an urban polluted environment. These observations strongly improved the daytime O_3 analysis. However, the analysis degraded compared to the model background during night hours. Factors that con-

tributed to this deterioration include the representation of the PBL vertical extent, the abundance of reactants, and the associated representation of pollutants and their emissions. These findings indicate that enhancing the EURAD-IM model in respect to these factors is essential to fully leverage the observations in the PBL. In conclusion, Zeppelin observations have shown high potential to monitor the distribution of pollutants in the PBL and to improve air quality analyses through data assimilation in regions with high emissions, particularly at elevated altitudes.

All the studies conducted in this thesis demonstrate the importance of the PBL observations for enhancing air quality analyses. Drones and Zeppelins consequently provide effective measuring platforms for bridging the observation gap in the lowest troposphere. While the Zeppelin observations are not intended for operational data collection and assimilation, they serve as a valuable tool for investigating and understanding the impact of observations. In contrast, drones are more suitable for operational use due to their low cost and easy operation. In the future, they might even define the next generation of air quality observing networks (O'Sullivan et al., 2021), but will certainly be used more for field campaigns. One excellent example of existing profile data within and above the PBL are the observations collected during passenger flights as part of IAGOS (In-service Aircraft for a Global Observing System). These observations are regularly assimilated in the CAMS regional analysis if available. For the analyses conducted in this study, IAGOS profiles could not be used for evaluation due to the lack of availability in the studied areas during the COVID-19 restrictions.

Given the encouraging results of this study, the widespread adoption of drones for measuring air pollutants and the assimilation of the collected data into air quality models is recommended. Conducting measurements strategically aligned with modelling requirements is essential to fully exploit the potential of drone and Zeppelin based observations. Particular emphasis should be placed on the time and location of the measurements. The study demonstrated that observations at night, during sunrise, and during the middle of the day are beneficial and informative as their assimilation improves the diurnal cycle of pollutants. However, it remains to be proved how regular observation flights throughout the entire day and night can further constrain the initial values and emission factors and thus improve the model analysis. Drone and Zeppelin measurement locations should be selected based on the wind speed and direction. Taking the observations downwind of dominant emission sources will likely improve the analysis as they catch the emissions and provide information on required corrections. Thus, campaign planning consulting an air quality model can help to determine optimal measurement sites and allow for better observability with respect to emission optimisation.

It is essential to acknowledge several limitations that influenced the assimilation results. First, in both studies presented in this thesis, the observational errors were approximated using the same method, following Elbern et al. (2007), which is a simple approach to estimate the observation errors. However, given the use of low-cost sensors onboard drones, accurate characterisation of observation error remains a critical aspect. More advanced techniques, such as the Desroziers Diagnostic (Desroziers et al., 2005) or ensemble-based approaches (Waller et al., 2014), could offer improved error estimates. Second, the model's resolution used in this study may not be sufficient to fully resolve local emissions, such as emission from the transport sector. This is especially evident in urban polluted environments. Exploring the assimilation of high-resolution drones and Zeppelin data with a high-resolution model grid might be partic-

ularly beneficial, as it has the potential to finer resolve pollutant dispersion and thus further improve the representation of pollutants in the PBL. Finally, an important constraint of the assimilation system lies in the consideration of fixed daily emission profiles in the optimisation algorithm. This inversion system is designed to optimise observations on a daily basis, meaning that data collected over a 24-hour period is generally necessary for effective optimisation of the daily emission factor that adjusts the amplitude of the temporal emission profile. Given the challenge of continuously observing the PBL using drones or Zeppelins for 24 hours, the need to develop an inversion system based on hourly rates to optimise the emission rates becomes apparent. Additionally, as drone and Zeppelin observations were proven to be most effective in observing emissions from local single sources (e.g., power plants), adopting a sector-specific approach to emission optimisation can yield better assimilation results (Backes, 2023).

For future studies on the impact of PBL observations assimilation on air quality analyses, the following studies are suggested. As discussed in the thesis and found in the literature, biases in PBL structure can lead to errors in pollutant forecasts (Peng et al., 2021; Mohan and Gupta, 2018). Evaluating different PBL parameterisation schemes (Cohen et al., 2015) in WRF and their impact on the EURAD-IM analysis when assimilating drone and Zeppelin observation is a sensitivity study that can further investigate the effect of the PBL representation in the model. Choosing the right PBL parameters is likely to improve the representation of vertical mixing and exchange processes between the convective mixed layer, the residual layer, and the free troposphere. For a good representation of O_3 concentrations in EURAD-IM, a good description of precursor emissions and concentrations is essential. While nitrogen oxides (NO_x) can be well constrained by observations, there are neither operational nor campaign-based volatile organic compound (VOC) observations available. Consequently, a good evaluation of VOCs in EURAD-IM is missing. Future studies can focus on comparing the model results with in situ VOCs measurements. For instance, this work could be conducted in collaboration with future measurement campaigns using the Zeppelin platform. As this thesis is limited to gaseous pollutants only, it would further be interesting to investigate the impact on the overall representation of air pollutants in the analysis by assimilating in situ aerosol observations in the PBL (e.g., particulate matter with diameters less than 2.5 µm ($PM_{2.5}$), and less than 10 µm (PM_{10})). Finally, one perspective is to increase the horizontal resolution of EURAD-IM to better resolve the meteorological and chemical processes and emission patterns. This improvement may significantly impact assimilating high-resolution airborne observations in the PBL.

Appendix A

Supplementary material for chapter 6

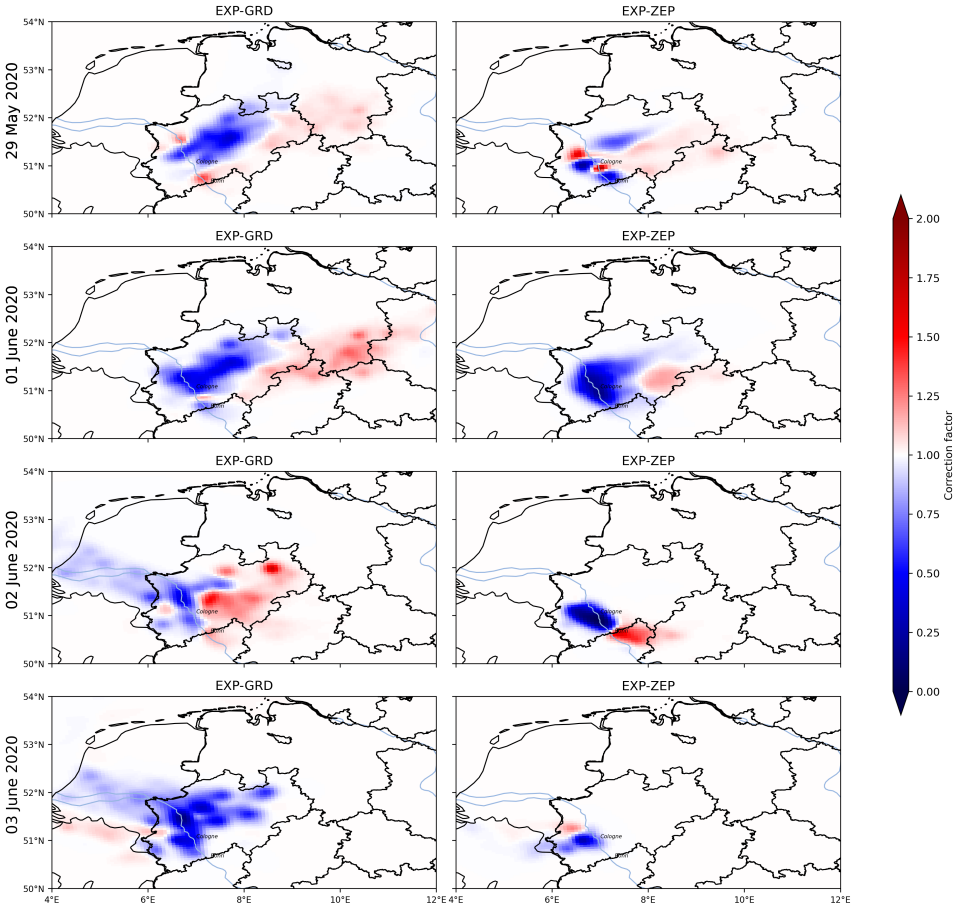

Figure A.1: *NO emission factors resulting from the EXP-ZEP (right) and EXP-GRD (left) simulations for the four study days.*

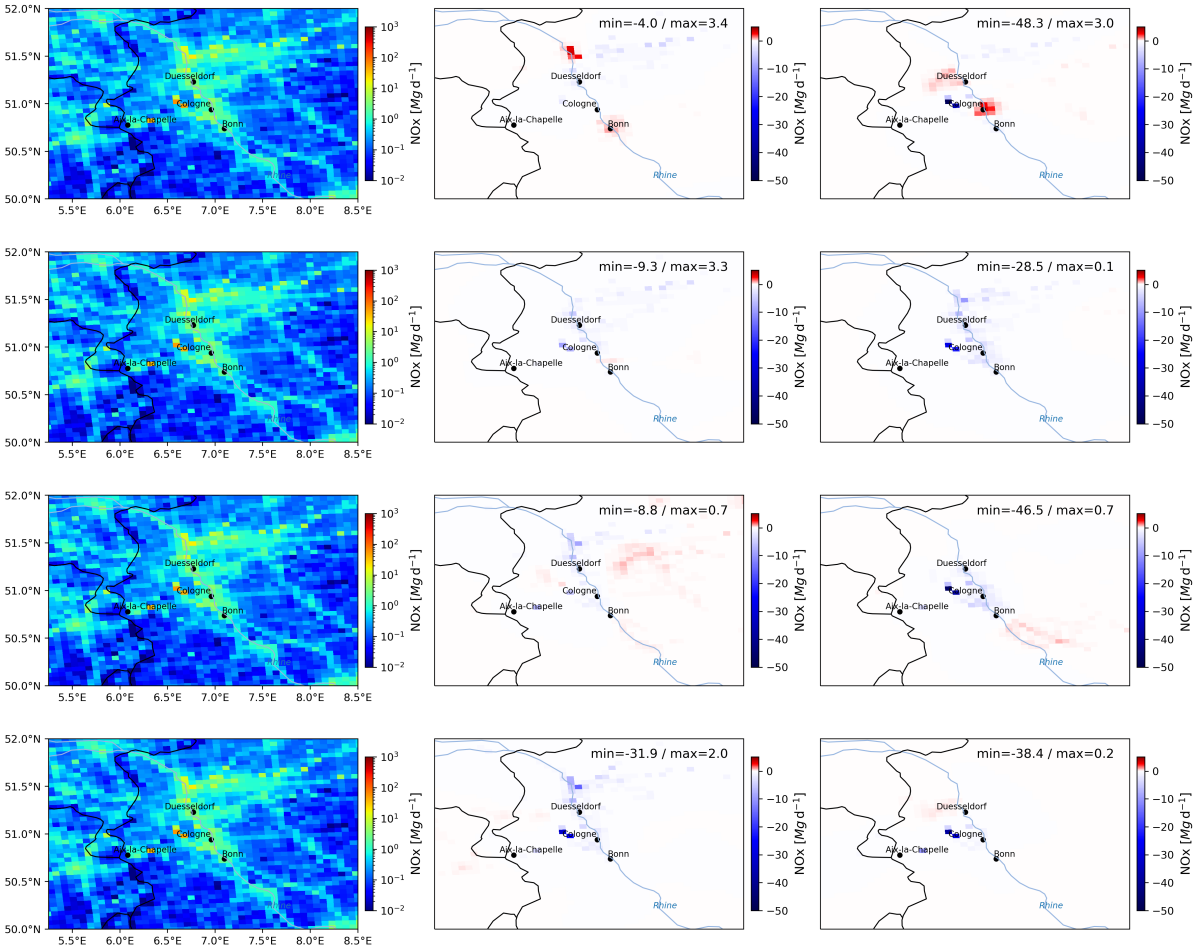

Figure A.2: *Daily NO_x emissions of the inventory (left) and the analysed NO_x emission changes for each analysed day of 29 May, and 01-03 June 2020 (1-4 lines). The changes are shown for EXP-ZEP in the right panels and EXP-GRD in the middle panels.*

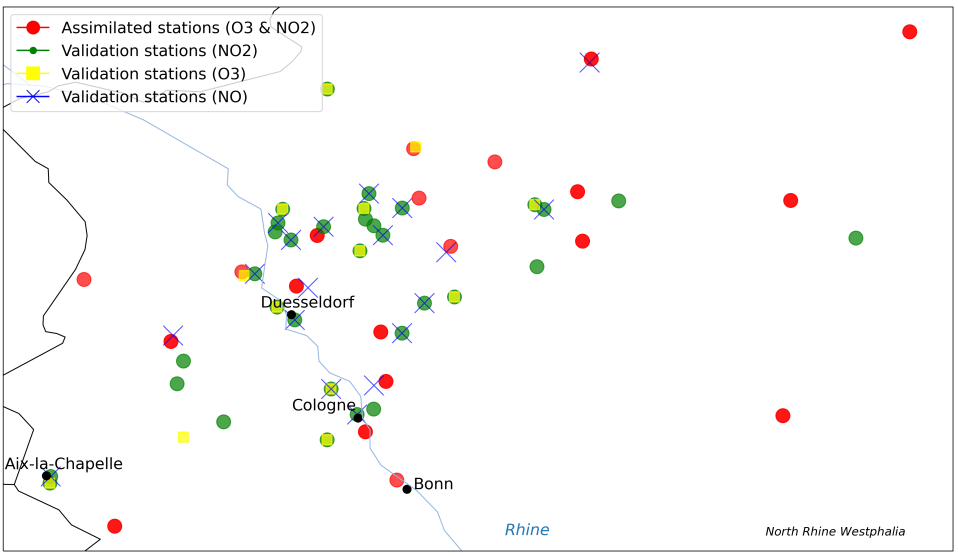

Figure A.3: *Map of ground-based observations assimilated in EXP-GRD and additional ground-based observations used for model validation in Section 6.1 and 6.2.*

Table A.1: *Information about ground-based monitoring stations used for data assimilation in Section 6.1 and 6.2.*

Station Code	Station Name	Station Type	Latitude (°N)	Longitude (°E)	Altitude
DENW079	Leverkusen-Manfort	Rural	51.0289	7.0051	50 m
DENW068	Soest-Ost	Remote/Mountain	51.5707	8.1481	110 m
DENW059	Köln-Rodenkirchen	Rural	50.8898	6.9852	45 m
DENW064	Simmerath (Eifel)	Remote/Mountain	50.6532	6.2811	572 m
DENW065	Netphen (Rothaargebirge)	Remote/Mountain	50.9303	8.1919	635 m
DENW067	Bielefeld-Ost	Suburban	52.0232	8.5484	102 m
DENW080	Solingen-Wald	Rural	51.1838	7.0526	207 m
DENW095	Münster-Geist	Suburban	51.9365	7.6116	63 m
DENW179	Schwerte	Suburban	51.4488	7.5823	157 m
DENW029	Hattingen-Blankenstein	Rural	51.4030	7.2086	93 m
DENW062	Bonn-Auerberg	Rural	50.7536	7.0827	57 m
DENW066	Nettetal-Kaldenkirchen	Remote/Mountain	51.3269	6.1959	49 m
DENW038	Mülheim-Styrum	Suburban	51.4535	6.8651	37 m
DENW078	Ratingen-Tiefenbroich	Rural	51.3039	6.8200	41 m
DENW006	Lünen-Niederaden	Rural	51.5922	7.5698	58 m
DENW022	Gelsenkirchen-Bismarck	Rural	51.5336	7.1018	40 m
DENW002	Datteln-Hagem	Rural	51.6414	7.3314	80 m
DENW015	Marl-Sickingmühle	Rural	51.6990	7.1227	42 m
DENW096	Mönchengladbach-Rheydt	Rural	51.1546	6.4257	78 m
DENW042	Krefeld-Linn	Suburban	51.3377	6.6402	32 m

Table A.2: *Information about ground-based monitoring stations used for data assimilation in Section 6.3.*

Station Code	Station Name	Station Type	Latitude (°N)	Longitude (°E)	Altitude
DERP007	Mainz-Mombach	Suburban	50.0171	8.2165	120 m
DERP009	Mainz-Zitadelle	Suburban	49.9950	8.2740	110 m
DERP025	Wörth-Marktplatz	Suburban	49.0523	8.2535	104 m
DEHE042	Linden/Leihgestern	Remote/Mountain	50.5330	8.6844	172 m
DERP001	Ludwigshafen-Oppau	Suburban	49.5151	8.4024	91 m
DERP022	Bad Kreuznach-Bosenheimer Str.	Suburban	49.8421	7.8662	108 m
DEHE001	Darmstadt	Suburban	49.8723	8.6646	158 m
DEHE011	Hanau	Traffic	50.1348	8.9181	106 m
DEBW004	Eggenstein	Remote/Mountain	49.0765	8.4067	109 m
DEBY004	Kleinwallstadt/Hofstetter Str.	Remote/Mountain	49.8694	9.1715	124 m
DEHE005	Frankfurt-Höchst	Traffic	50.1019	8.5421	104 m
DEHE026	Spessart	Remote/Mountain	50.1644	9.3994	502 m
DEHE039	Burg Herzberg (Grebenau)	Remote/Mountain	50.7704	9.4594	491 m
DEHE043	Riedstadt	Remote/Mountain	49.8252	8.5168	87 m
DEHE045	Michelstadt	Suburban	49.6725	9.0020	209 m
DENW065	Netphen (Rothaargebirge)	Remote/Mountain	50.9303	8.1919	635 m
DERP028	Westerwald-Neuhäusel	Remote/Mountain	50.4243	7.7299	546 m
DERP053	—	Rural	49.3511	8.4230	103 m
DERP060	—	Suburban	49.1920	7.6146	378 m
DEBW010	Wiesloch	Rural	49.3007	8.7001	162 m
DEHE008	Frankfurt-Ost	Suburban	50.1253	8.7463	100 m
DEHE051	Wasserkuppe	Remote/Mountain	50.4977	9.9359	931 m
DEBW015	Heilbronn	Urban	49.1655	9.2248	157 m
DEHE044	Limburg	Suburban	50.3832	8.0610	128 m
DEBW081	Karlsruhe-Nordwest	Suburban	49.0286	8.3556	114 m
DEHE030	Marburg	Suburban	50.8043	8.7693	182 m
DEBY077	Würzburg/Kopfklinik	Rural	49.8047	9.9564	226 m

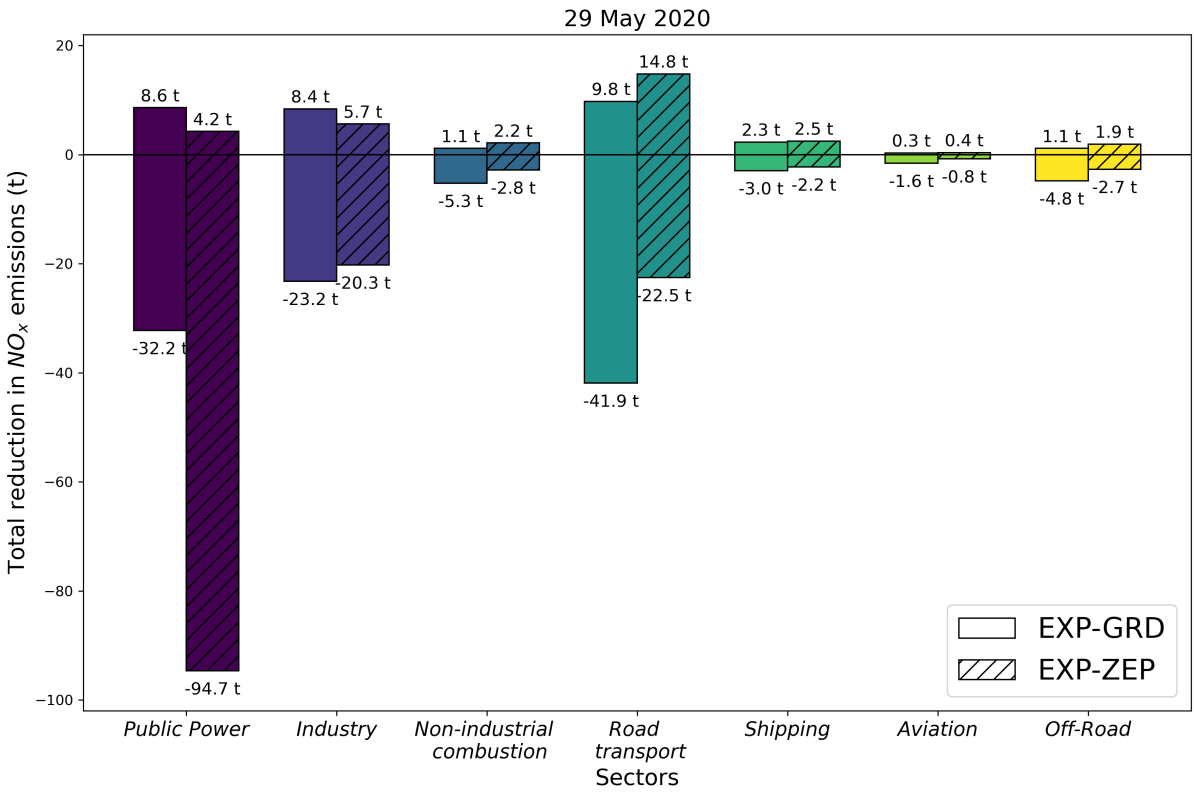

Figure A.4: *Total change in NO_x emissions between the optimised and original emisison inventories for different emission sectors on 29 May 2020. Negative changes (reductions) and positive changes (increases) are summed separately. Bars indicate contributions from EXP-ZEP (non-shaded) and EXP-GRD (shaded) to the emission change in tonnes/day.*

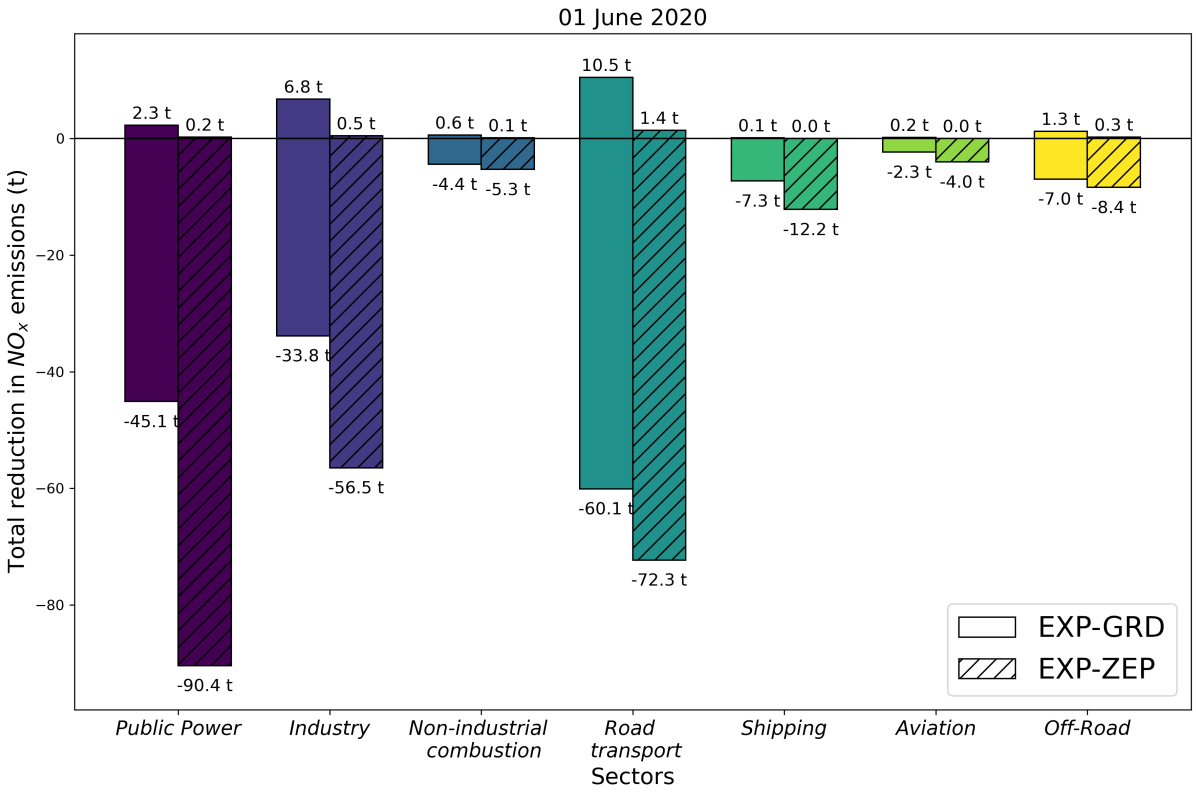

Figure A.5: *Same as Fig. A.4 but for 01 June 2020.*

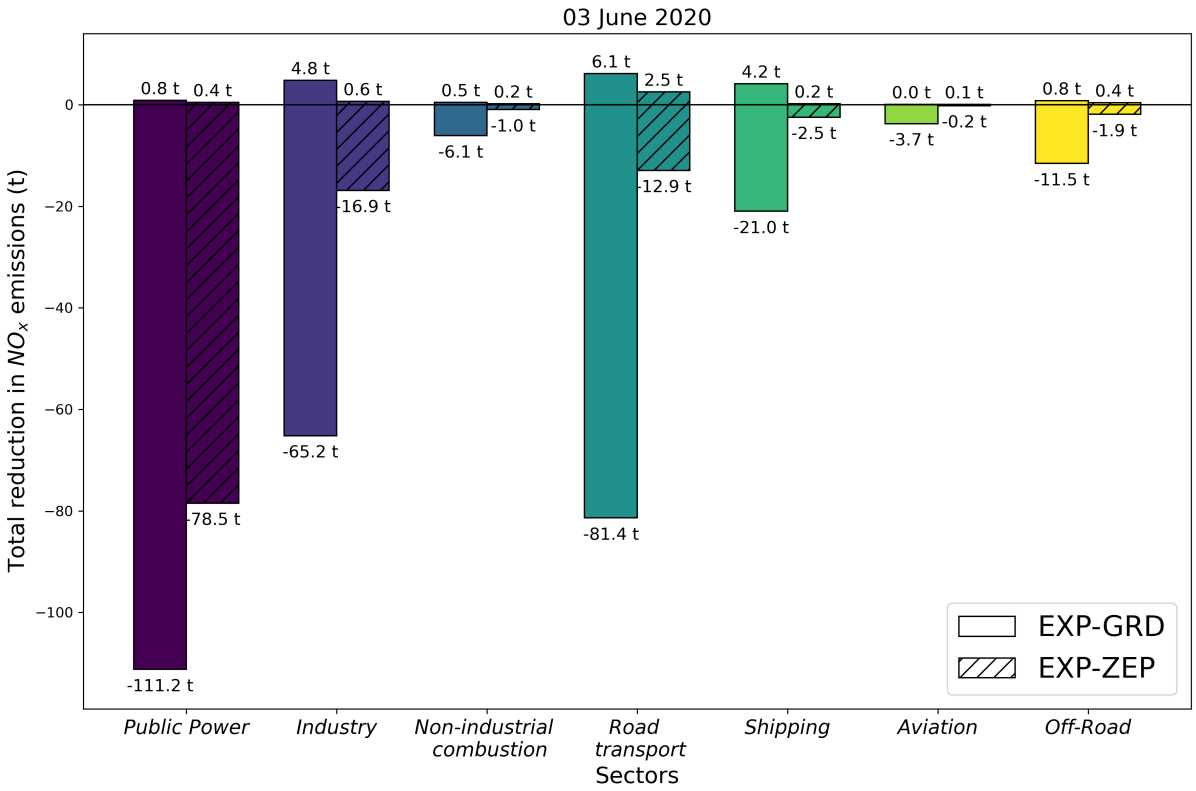

Figure A.6: *Same as Fig. A.4 but for 03 June 2020.*

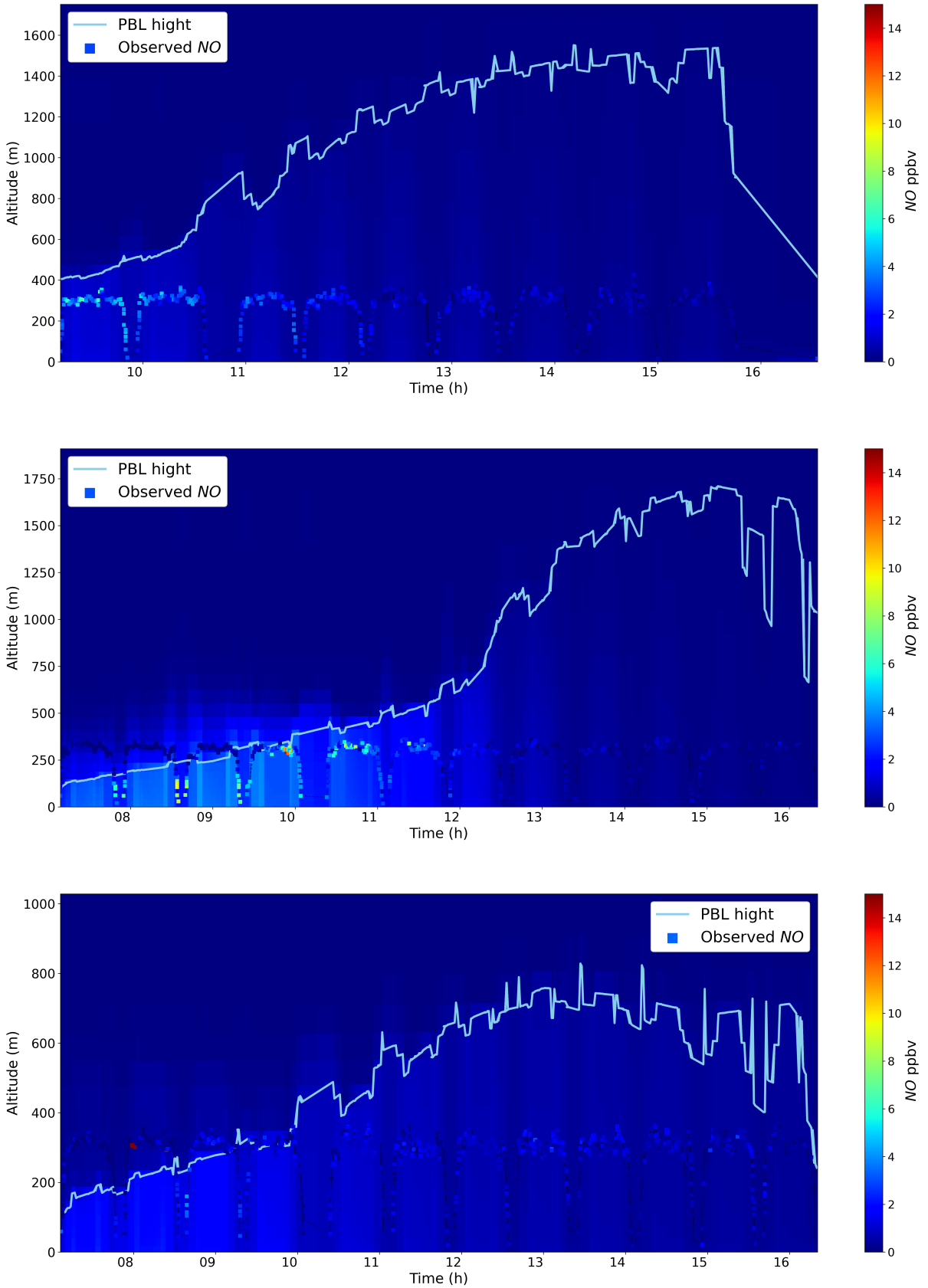

Figure A.7: *Time series of NO observations from the Zeppelin as a function of altitude for 11 September 2020 (top), 12 September 2020 (middle), and 13 September 2020 (bottom), with model predictions from the reference simulation (without assimilation) shown in the background. The PBL height calculated by the model is indicated by the blue line.*

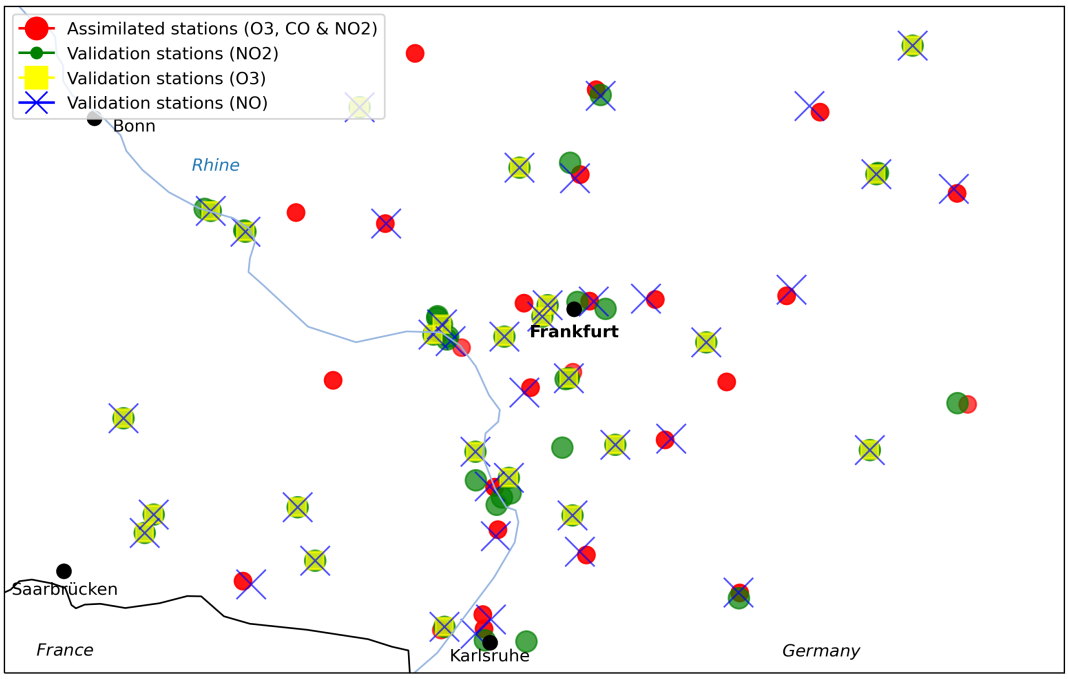

Figure A.8: *Validation stations for section 6.3.*

Bibliography

Ackermann, I. J., Hass, H., Memmesheimer, M., Ebel, A., Binkowski, F. S., and Shankar, U.: Modal aerosol dynamics model for Europe: development and first applications, *Atmos. Environ.*, 32, 2981–2999, https://doi.org/10.1016/S1352-2310(98)00006-5, 1998.

Alamouri, A., Lampert, A., and Gerke, M.: An Exploratory Investigation of UAS Regulations in Europe and the Impact on Effective Use and Economic Potential, *Drones*, 5 (3), https://doi.org/10.3390/drones5030063, 2021.

Arakawa, A. and Lamb, V. R.: Computational Design of the Basic Dynamical Processes of the UCLA General Circulation Model, *General Circulation Models of the Atmosphere*, 17, 173–265, https://doi.org/10.1016/B978-0-12-460817-7.50009-4, 1977.

Backes, P. M.: Polluter group specific emission optimisation for regional air quality analyses using four-dimensional variational data assimilation, Ph.D. thesis, University of Cologne, https://kups.ub.uni-koeln.de/70492/, 2023.

Baklanov, A. and Zhang, Y.: Advances in air quality modeling and forecasting, *Global Transitions*, 2, 261–270, https://doi.org/https://doi.org/10.1016/j.glt.2020.11.001, 2020.

Balamurugan, V., Chen, J., Qu, Z., Bi, X., Gensheimer, J., Shekhar, A., Bhattacharjee, S., and Keutsch, F. N.: Tropospheric NO_2 and O_3 Response to COVID-19 Lockdown Restrictions at the National and Urban Scales in Germany, *J. Geophys. Res.: Atmospheres*, 126 (19), e2021JD035 440, https://doi.org/10.1029/2021JD035440, 2021.

Barton-Grimley, R. A., Nehrir, A. R., Kooi, S. A., Collins, J. E., Harper, D. B., Notari, A., Lee, J., DiGangi, J. P., Choi, Y., and Davis, K. J.: Evaluation of the High Altitude Lidar Observatory (HALO) methane retrievals during the summer 2019 ACT-America campaign, *Atmospheric Measurement Techniques*, 15 (15), 4623–4650, https://doi.org/10.5194/amt-15-4623-2022, 2022.

Bauer, P., Thorpe, A., and Brunet, G.: The quiet revolution of numerical weather prediction, *Nature*, 525, 47–55, https://doi.org/10.1038/nature14956, 2015.

Beirle, S., Borger, C., Dörner, S., Eskes, H., Kumar, V., de Laat, A., and Wagner, T.: Catalog of NO_x emissions from point sources as derived from the divergence of the NO_2 flux for TROPOMI, *Earth System Science Data*, 13 (6), 2995–3012, https://doi.org/10.5194/essd-13-2995-2021, 2021.

Bocquet, M., Elbern, H., Eskes, H., Hirtl, M., Žabkar, R., Carmichael, G. R., Flemming, J., Inness, A., Pagowski, M., Pérez Camaño, J. L., Saide, P. E., San Jose, R., Sofiev, M., Vira, J., Baklanov, A., Carnevale, C., Grell, G., and Seigneur, C.: Data assimilation in atmospheric chemistry models: current status and future prospects for coupled chemistry meteorology models, *Atmos. Chem. Phys.*, 15 (10), 5325–5358, https://doi.org/10.5194/acp-15-5325-2015, 2015.

Boersma, K. F., Eskes, H. J., and Brinksma, E. J.: Error analysis for tropospheric NO_2 retrieval from space, *J. Geophys. Res.: Atmospheres*, 109 (D4), https://doi.org/10.1029/2003JD003962, 2004.

Boersma, K. F., Vinken, G. C. M., and Eskes, H. J.: Representativeness errors in comparing chemistry transport and chemistry climate models with satellite UVVis tropospheric column retrievals, *Geoscientific Model Development*, 9 (2), 875–898, https://doi.org/10.5194/gmd-9-875-2016, 2016.

Bolek, A., Heimann, M., and Göckede, M.: UAV-based in situ measurements of CO_2 and CH_4 fluxes over complex natural ecosystems, *Atmospheric Measurement Techniques*, 17 (18), 5619–5636, https://doi.org/10.5194/amt-17-5619-2024, 2024.

Brandt, T.: Zeppelin NT - The Utility Airship Zeppelin NT as a Platform for Remote Sensing for Environmental and Industrial Applications, https://doi.org/10.2514/6.2007-7879, 2007.

Bretschneider, L., Schlerf, A., Baum, A., Bohlius, H., Buchholz, M., Düsing, S., Ebert, V., Erraji, H., Frost, P., Käthner, R., Krüger, T., Lange, A. C., Langner, M., Nowak, A., Pätzold, F., Rüdiger, J., Saturno, J., Scholz, H., Schuldt, T., Seldschopf, R., Sobotta, A., Tillmann, R., Wehner, B., Wesolek, C., Wolf, K., and Lampert, A.: MesSBAR-Multicopter and Instrumentation for Air Quality Research, *Atmosphere*, https://doi.org/10.3390/atmos13040629, 2022.

Chen, Z., Petetin, H., Méndez Turrubiates, R., Achebak, H., García-Pando, C., and Ballester, J.: Population exposure to multiple air pollutants and its compound episodes in Europe, *Nature Communications*, 15, 2094, https://doi.org/10.1038/s41467-024-46103-3, 2024.

Cohen, A. E., Cavallo, S. M., Coniglio, M. C., and Brooks, H. E.: A Review of Planetary Boundary Layer Parameterization Schemes and Their Sensitivity in Simulating Southeastern U.S. Cold Season Severe Weather Environments, *Weather and Forecasting*, 30 (3), 591 – 612, https://doi.org/10.1175/WAF-D-14-00105.1, 2015.

Colette, A., Collin, G., Besson, F., Blot, E., Guidard, V., Meleux, F., Royer, A., Petiot, V., Miller, C., Fermond, O., Jeant, A., Adani, M., Arteta, J., Benedictow, A., Bergström, R., Bowdalo, D., Brandt, J., Briganti, G., Carvalho, A. C., Christensen, J. H., Couvidat, F., D'Elia, I., D'Isidoro, M., Denier van der Gon, H., Descombes, G., Di Tomaso, E., Douros, J., Escribano, J., Eskes, H., Fagerli, H., Fatahi, Y., Flemming, J., Friese, E., Frohn, L., Gauss, M., Geels, C., Guarnieri, G., Guevara, M., Guion, A., Guth, J., Hänninen, R., Hansen, K.,

Im, U., Janssen, R., Jeoffrion, M., Joly, M., Jones, L., Jorba, O., Kadantsev, E., Kahnert, M., Kaminski, J. W., Kouznetsov, R., Kranenburg, R., Kuenen, J., Lange, A. C., Langner, J., Lannuque, V., Macchia, F., Manders, A., Mircea, M., Nyiri, A., Olid, M., Pérez García-Pando, C., Palamarchuk, Y., Piersanti, A., Raux, B., Razinger, M., Robertson, L., Segers, A., Schaap, M., Siljamo, P., Simpson, D., Sofiev, M., Stangel, A., Struzewska, J., Tena, C., Timmermans, R., Tsikerdekis, T., Tsyro, S., Tyuryakov, S., Ung, A., Uppstu, A., Valdebenito, A., van Velthoven, P., Vitali, L., Ye, Z., Peuch, V.-H., and Rouïl, L.: Copernicus Atmosphere Monitoring Service – Regional Air Quality Production System v1.0, *EGUsphere*, 2024, 1–92, https://doi.org/10.5194/egusphere-2024-3744, 2024.

Collin, G.: Regional Production, Updated documentation covering all Regional operational systems and the ENSEMBLE Following U2 upgrade, February 2020, Tech. rep., METEO-FRANCE, https://atmosphere.copernicus.eu/sites/default/files/2020-09/CAMS50_2018SC2_D2.0.2-U2_Models_documentation_202003_v2.pdf, 2020.

Copernicus Atmosphere Monitoring Service: Annual EQC Report for the Interim Reanalysis for 2023, for Each of the Operational Systems and the ENSEMBLE, Tech. Rep. CAMS283 2021SC2 D83.2.1.1-2023 202406 EQC IRA2023 v1, Copernicus Atmosphere Monitoring Service (CAMS), https://atmosphere.copernicus.eu/sites/default/files/custom-uploads/EQC-regional/IRA/CAMS283_2021SC2_D83.2.1.1-2023_202406_EQC_IRA2023_v1.pdf, Issued by INERIS / F. Meleux, 2024.

De Souza Fernandes Duarte, E., Franke, P., Lange, A. C., Friese, E., Juliano da Silva Lopes, F., João da Silva, J., Souza dos Reis, J., Landulfo, E., Santos e Silva, C. M., Elbern, H., and Hoelzemann, J. J.: Evaluation of atmospheric aerosols in the metropolitan area of São Paulo simulated by the regional EURAD-IM model on high-resolution, *Atmospheric Pollution Research*, 12 (2), 451–469, https://doi.org/10.1016/j.apr.2020.12.006, 2021.

der Gon, H. D. V., Gauss, M., Granier, C., Arellano, S., Benedictow, A., Darras, S., Dellaert, S., Guevara, M., Jalkanen, J.-P., Krueger, K., Kuenen, J., Liaskoni, M., Liousse, C., Markova, J., Perez, A. P., Quack, B., Simpson, D., Sindelarova, K., and Soulie, A.: CAMS2_61 – Global and European Emission Inventories: Documentation of CAMS Emission Inventory Products, Technical Report CAMS261_2021SC1_D6.1.2-2022_202306_Docu_v1, TNO, MET Norway, CNRS, https://doi.org/10.24380/q2si-ti6i, 2023.

Desroziers, G., Berre, L., Chapnik, B., and Poli, P.: Diagnosis of observation, background and analysis-error statistics in observation space, *Q. J. Roy. Meteor. Soc.*, 131 (613), 3385–3396, https://doi.org/10.1256/qj.05.108, 2005.

Douros, J., Eskes, H., van Geffen, J., Boersma, K. F., Compernolle, S., Pinardi, G., Blechschmidt, A.-M., Peuch, V.-H., Colette, A., and Veefkind, P.: Comparing Sentinel-5P TROPOMI NO_2 column observations with the CAMS regional air quality ensemble, *Geosci. Model Dev.*, 16 (2), 509–534, https://doi.org/10.5194/gmd-16-509-2023, 2023.

ECMWF: IFS Documentation CY48R1 - Part VIII: Atmospheric Composition, 8, ECMWF, https://doi.org/10.21957/749dc09059, 2023.

Elbern, H. and Schmidt, H.: A four-dimensional variational chemistry data assimilation scheme for Eulerian chemistry transport modeling, *J. Geophys. Res.: Atmospheres*, 104 (D15), 18 583–18 598, https://doi.org/10.1029/1999JD900280, 1999.

Elbern, H., Strunk, A., Schmidt, H., and Talagrand, O.: Emission rate and chemical state estimation by 4-dimensional variational inversion, *Atmos. Chem. Phys*, 7, 3749–3769, https://doi.org/10.5194/acp-7-3749-2007, 2007.

European Commission: Euro 6/VI evaluation study, Publications Office of the European Union, https://doi.org/10.2873/933978, 2022.

Foret, G., Eremenko, M., Cuesta, J., Sellitto, P., Barré, J., Gaubert, B., Coman, A., Dufour, G., Liu, X., Joly, M., Doche, C., and Beekmann, M.: Ozone pollution: What can we see from space? A case study, *J. Geophys. Res.: Atmospheres*, 119 (13), 8476–8499, https://doi.org/10.1002/2013JD021340, 2014.

Franke, P., Lange, A. C., Steffens, B., Pozzer, A., Wahner, A., and Kiendler-Scharr, A.: European air quality in view of the WHO 2021 guideline levels: Effect of emission reductions on air pollution exposure, *Elem. Sci. Anth.*, 12 (1), 00 127, https://doi.org/10.1525/elementa.2023.00127, 2024.

Freney, E. J., Sellegri, K., Canonaco, F., Colomb, A., Borbon, A., Michoud, V., Doussin, J.-F., Crumeyrolle, S., Amarouche, N., Pichon, J.-M., Bourianne, T., Gomes, L., Prevot, A. S. H., Beekmann, M., and Schwarzenböeck, A.: Characterizing the impact of urban emissions on regional aerosol particles: airborne measurements during the MEGAPOLI experiment, *Atmospheric Chemistry and Physics*, 14 (3), 1397–1412, https://doi.org/10.5194/acp-14-1397-2014, 2014.

Geiger, H., Barnes, I., Bejan, I., Benter, T., and Spittler, M.: The tropospheric degradation of isoprene: an updated module for the regional atmospheric chemistry mechanism, *Atmos. Environ.*, 37 (11), 1503–1519, https://doi.org/10.1016/S1352-2310(02)01047-6, 2003.

Griffin, D., McLinden, C. A., Racine, J., Moran, M. D., Fioletov, V., Pavlovic, R., Mashayekhi, R., Zhao, X., and Eskes, H.: Assessing the Impact of Corona-Virus-19 on Nitrogen Dioxide Levels over Southern Ontario, Canada, *Remote Sensing*, 12 (24), 4112, https://doi.org/10.3390/rs12244112, 2020.

Guenther, A. B., Jiang, X., Heald, C. L., Sakulyanontvittaya, T., Duhl, T., Emmons, L. K., and Wang, X.: The Model of Emissions of Gases and Aerosols from Nature version 2.1 (MEGAN2.1): an extended and updated framework for modeling biogenic emissions, *Geosci. Model Dev.*, 5, 1471–1492, https://doi.org/10.5194/gmd-5-1471-2012, 2012.

Guevara, M., Jorba, O., Tena, C., Denier van der Gon, H., Kuenen, J., Elguindi, N., Darras, S., Granier, C., and Pérez García-Pando, C.: Copernicus Atmosphere

Monitoring Service TEMPOral profiles (CAMS-TEMPO): global and European emission temporal profile maps for atmospheric chemistry modelling, *Earth System Science Data*, 13 (2), 367–404, https://doi.org/10.5194/essd-13-367-2021, 2021.

Guevara, M., Petetin, H., Jorba, O., Denier van der Gon, H., Kuenen, J., Super, I., Jalkanen, J.-P., Majamäki, E., Johansson, L., Peuch, V.-H., and Pérez García-Pando, C.: European primary emissions of criteria pollutants and greenhouse gases in 2020 modulated by the COVID-19 pandemic disruptions, *Earth System Science Data*, 14 (6), 2521–2552, https://doi.org/10.5194/essd-14-2521-2022, 2022.

Hersbach, H., Bell, B., Berrisford, P., Hirahara, S., Horányi, A., Muñoz-Sabater, J., Nicolas, J., Peubey, C., Radu, R., Schepers, D., Simmons, A., Soci, C., Abdalla, S., Abellan, X., Balsamo, G., Bechtold, P., Biavati, G., Bidlot, J., Bonavita, M., De Chiara, G., Dahlgren, P., Dee, D., Diamantakis, M., Dragani, R., Flemming, J., Forbes, R., Fuentes, M., Geer, A., Haimberger, L., Healy, S., Hogan, R. J., Hólm, E., Janisková, M., Keeley, S., Laloyaux, P., Lopez, P., Lupu, C., Radnoti, G., de Rosnay, P., Rozum, I., Vamborg, F., Villaume, S., and Thépaut, J.-N.: The ERA5 global reanalysis, *Q. J. Roy. Meteor. Soc.*, 146 (730), 1999–2049, https://doi.org/10.1002/qj.3803, 2020.

Hervo, M., Romanens, G., Martucci, G., Weusthoff, T., and Haefele, A.: Evaluation of an Automatic Meteorological Drone Based on a 6-Month Measurement Campaign, *Atmosphere*, 14 (9), https://doi.org/10.3390/atmos14091382, 2023.

Hu, J., Li, Y., Zhao, T., Liu, J., Hu, X.-M., Liu, D., Jiang, Y., Xu, J., and Chang, L.: An important mechanism of regional O_3 transport for summer smog over the Yangtze River Delta in eastern China, *Atmos. Chem. Phys.*, 18 (22), 16 239–16 251, https://doi.org/10.5194/acp-18-16239-2018, 2018.

Ialongo, I., Virta, H., Eskes, H., Hovila, J., and Douros, J.: Comparison of TROPOMI/Sentinel-5 Precursor NO_2 observations with ground-based measurements in Helsinki, *Atmos. Meas. Tech.*, 13 (1), 205–218, https://doi.org/10.5194/amt-13-205-2020, 2020.

Jaffe, D.: Relationship between Surface and Free Tropospheric Ozone in the Western U.S., *Environmental Science & Technology*, 45 (2), 432–438, https://doi.org/10.1021/es1028102, pMID: 21142065, 2011.

Jensen, A. A., Pinto, J. O., Bailey, S. C. C., Sobash, R. A., de Boer, G., Houston, A. L., Chilson, P. B., Bell, T., Romine, G., Smith, S. W., Lawrence, D. A., Dixon, C., Lundquist, J. K., Jacob, J. D., Elston, J., Waugh, S., and Steiner, M.: Assimilation of a Coordinated Fleet of Uncrewed Aircraft System Observations in Complex Terrain: EnKF System Design and Preliminary Assessment, *Mon. Wea. Rev.*, 149, 1459–1480, https://doi.org/10.1175/MWR-D-20-0359.1, 2021.

Jin, X., Zhu, Q., and Cohen, R. C.: Direct estimates of biomass burning NO_x emissions and lifetimes using daily observations from TROPOMI, *Atmos. Chem. Phys.*, 21 (20), 15 569–15 587, https://doi.org/10.5194/acp-21-15569-2021, 2021.

Jäger, J.: Airborne VOC measurements on board the Zeppelin NT during the PEGASOS campaigns in 2012 deploying the improved Fast-GC-MSD System, Ph.d. thesis, Forschungszentrum Jülich GmbH, Troposphere (IEK-8), http://kups.ub.uni-koeln.de/id/eprint/5462, 2014.

Kalnay, E.: Atmospheric Modeling, Data Assimilation and Predictability, Cambridge University Press, Cambridge, United Kingdom, https://www.cambridge.org/9780511074738, 2005.

Kaser, L., Patton, E. G., Pfister, G. G., Weinheimer, A. J., Montzka, D. D., Flocke, F., Thompson, A. M., Stauffer, R. M., and Halliday, H. S.: The effect of entrainment through atmospheric boundary layer growth on observed and modeled surface ozone in the Colorado Front Range, *J. Geophys. Res.: Atmospheres*, 122 (11), 6075–6093, https://doi.org/10.1002/2016JD026245, 2017.

Kazanas, K.: Morning aerosol vertical profiles in the Planetary Boundary Layer: Observations on a Zeppelin NT Airship and comparison with a Regional Model, Ph.D. thesis, Universität zu Köln, Köln, Germany, https://kups.ub.uni-koeln.de/8294/1/thesis_Kazanas.pdf, 2017.

Kilian, M., Grewe, V., Jöckel, P., Kerkweg, A., Mertens, M., Zahn, A., and Ziereis, H.: Ozone source attribution in polluted European areas during summer 2017 as simulated with MECO(n), *Atmos. Chem. Phys.*, 24 (23), 13 503–13 523, https://doi.org/10.5194/acp-24-13503-2024, 2024.

Koelemeijer, R. B. A., Stammes, P., Hovenier, J. W., and de Haan, J. F.: A fast method for retrieval of cloud parameters using oxygen A band measurements from the Global Ozone Monitoring Experiment, *J. Geophys. Res.: Atmospheres*, 106 (D4), 3475–3490, https://doi.org/10.1029/2000JD900657, 2001.

Kuenen, J. J. P., Visschedijk, A. J. H., Jozwicka, M., and van der Gon, H. A. C. D.: TNO-MACC-II emission inventory; a multi-year (2003-2009) consistent high-resolution European emission inventory for air quality modelling, *Atmos. Chem. Phys.*, 14, 10 963–10 976, https://doi.org/10.5194/acp-14-10963-2014, 2014.

Lakkala, K., Kujanpää, J., Brogniez, C., Henriot, N., Arola, A., Aun, M., Auriol, F., Bais, A. F., Bernhard, G., De Bock, V., Catalfamo, M., Deroo, C., Diémoz, H., Egli, L., Forestier, J.-B., Fountoulakis, I., Garane, K., Garcia, R. D., Gröbner, J., Hassinen, S., Heikkilä, A., Henderson, S., Hülsen, G., Johnsen, B., Kalakoski, N., Karanikolas, A., Karppinen, T., Lamy, K., León-Luis, S. F., Lindfors, A. V., Metzger, J.-M., Minvielle, F., Muskatel, H. B., Portafaix, T., Redondas, A., Sanchez, R., Siani, A. M., Svendby, T., and Tamminen, J.: Validation of the TROPOspheric Monitoring Instrument (TROPOMI) surface UV radiation product, *Atmospheric Measurement Techniques*, 13 (12), 6999–7024, https://doi.org/10.5194/amt-13-6999-2020, 2020.

Lampert, A., Altstädter, B., Bärfuss, K., Bretschneider, L., Sandgaard, J., Michaelis, J., Lobitz, L., Asmussen, M., Damm, E., Käthner, R., Krüger, T., Lüpkes, C., Nowak, S., Peuker, A., Rausch, T., Reiser, F., Scholtz, A., Zakharov,

D. S., Gaus, D., Bansmer, S., Wehner, B., and Pätzold, F.: Unmanned Aerial Systems for Investigating the Polar Atmospheric Boundary Layer - Technical Challenges and Examples of Applications, *Atmosphere*, 11, 416, https://doi.org/10.3390/atmos11040416, 2020.

Lange, K., Richter, A., and Burrows, J. P.: Variability of nitrogen oxide emission fluxes and lifetimes estimated from Sentinel-5P TROPOMI observations, *Atmos. Chem. Phys.*, 22 (4), 2745–2767, https://doi.org/10.5194/acp-22-2745-2022, 2022.

Liu, C., Gao, M., Hu, Q., Brasseur, G. P., and Carmichael, G. R.: Stereoscopic Monitoring: A Promising Strategy to Advance Diagnostic and Prediction of Air Pollution, *Bulletin of the American Meteorological Society*, 102 (4), E730 – E737, https://doi.org/10.1175/BAMS-D-20-0217.1, 2021.

Liu, D. C. and Nocedal, J.: On the limited memory BFGS method for large scale optimization, *Math. Program.*, 45, 503–528, https://doi.org/10.1007/BF01589116, 1989.

Lorenc, A. C.: Analysis methods for numerical weather prediction, *Q. J. Roy. Meteor. Soc.*, 112 (474), 1177–1194, https://doi.org/10.1002/qj.49711247414, 1986.

Lorente, A. and Boersma, K.F.and Eskes, H.: Quantification of nitrogen oxides emissions from build-up of pollution over Paris with TROPOMI., *Sci*, 9, https://doi.org/10.1038/s41598-019-56428-5, 2019.

Marin, D. B., Becciolini, V., Santana, L. S., Rossi, G., and Barbari, M.: State of the Art and Future Perspectives of Atmospheric Chemical Sensing Using Unmanned Aerial Vehicles: A Bibliometric Analysis, *Sensors (Basel)*, 23 (20), 8384, https://doi.org/10.3390/s23208384, 2023.

McRae, G. J., Goodin, W. R., and Seinfeld, J. H.: Numerical solution of the atmospheric diffusion equation for chemically reacting flows, *Journal of Computational Physics*, 45 (1), 1–42, https://doi.org/10.1016/0021-9991(82)90101-2, 1982.

Menut, L. and Bessagnet, B.: What Can We Expect from Data Assimilation for Air Quality Forecast? Part I: Quantification with Academic Test Cases, *Journal of Atmospheric and Oceanic Technology*, 36 (2), 269 – 279, https://doi.org/10.1175/JTECH-D-18-0002.1, 2019.

Mohan, M. and Gupta, M.: Sensitivity of PBL parameterizations on PM10 and ozone simulation using chemical transport model WRF-Chem over a sub-tropical urban airshed in India, *Atmos. Environ.*, 185, 53–63, https://doi.org/10.1016/j.atmosenv.2018.04.054, 2018.

Myriokefalitakis, S., Daskalakis, N., Fanourgakis, G. S., Voulgarakis, A., Krol, M. C., Aan de Brugh, J. M. J., and Kanakidou, M.: Ozone and carbon monoxide budgets over the eastern Mediterranean, *Science of The Total Environment*, 563-564, 40–52, https://doi.org/10.1016/j.scitotenv.2016.04.061, 2016.

O'Sullivan, D., Taylor, S., Elston, J., Baker, C. B., Hotz, D., Marshall, C., Jacob, J., Barfuss, K., Piguet, B., Roberts, G., Omanovic, N., Fengler, M., Jensen, A. A., Steiner, M., and Houston, A. L.: The Status and Future of Small Uncrewed Aircraft Systems (UAS) in Operational Meteorology, *Bull. Am. Meteorol. Soc.*, 102, E2121–E2136, https://doi.org/10.1175/BAMS-D-20-0138.1, 2021.

Parrish, D. D., Aikin, K. C., Oltmans, S. J., Johnson, B. J., Ives, M., and Sweeny, C.: Impact of transported background ozone inflow on summertime air quality in a California ozone exceedance area, *Atmos. Chem. Phys.*, 10 (20), 10 093–10 109, https://doi.org/10.5194/acp-10-10093-2010, 2010.

Paschalidi, Z.: Inverse Modelling for Tropospheric Chemical State Estimation by 4-Dimensional Variational Data Assimilation from Routinely and Campaign Platforms, Ph.D. thesis, University of Cologne, http://kups.ub.uni-koeln.de/id/eprint/6588, 2015.

Pay, M. T., Gangoiti, G., Guevara, M., Napelenok, S., Querol, X., Jorba, O., and Pérez García-Pando, C.: Ozone source apportionment during peak summer events over southwestern Europe, *Atmos. Chem. Phys.*, 19 (8), 5467–5494, https://doi.org/10.5194/acp-19-5467-2019, 2019.

Peng, Y., Wang, H., Zhang, X., Zhao, T., Jiang, T., Che, H., Zhang, X., Zhang, W., and Liu, Z.: Impacts of PBL schemes on PM2.5 simulation and their responses to aerosol-radiation feedback in GRAPES_CUACE model during severe haze episodes in Jing-Jin-Ji, China, *Atmospheric Research*, 248, 105 268, https://doi.org/10.1016/j.atmosres.2020.105268, 2021.

Peng, Z., Liu, Z., Chen, D., and Ban, J.: Improving PM2.5 forecast over China by the joint adjustment of initial conditions and source emissions with an ensemble Kalman filter, *Atmos. Chem. Phys.*, 17 (7), 4837–4855, https://doi.org/10.5194/acp-17-4837-2017, 2017.

Pires, C., Vautard, R., and Talagrand, O.: On Extending the Limits of Variational Assimilation in Nonlinear Chaotic Systems, *Tellus A: Dynamic Meteorology and Oceanography*, 48 (1), 96–121, https://doi.org/10.3402/tellusa.v48i1.11634, 1996.

Poraicu, C., Muller, J.-F., Stavrakou, T., Fonteyn, D., Tack, F., Deutsch, F., Laffineur, Q., Van Malderen, R., and Veldeman, N.: Cross-evaluating WRF-Chem v4.1.2, TROPOMI, APEX, and in situ NO_2 measurements over Antwerp, Belgium, *Geosci. Model Dev.*, 16 (2), 479–508, https://doi.org/10.5194/gmd-16-479-2023, 2023.

Qu, K., Wang, X., Cai, X., Yan, Y., Jin, X., Vrekoussis, M., Kanakidou, M., Brasseur, G. P., Shen, J., Xiao, T., Zeng, L., and Zhang, Y.: Rethinking the role of transport and photochemistry in regional ozone pollution: insights from ozone concentration and mass budgets, *Atmos. Chem. Phys.*, 23 (13), 7653–7671, https://doi.org/10.5194/acp-23-7653-2023, 2023.

Rosati, B., Gysel, M., Rubach, F., Mentel, T. F., Goger, B., Poulain, L., Schlag, P., Miettinen, P., Pajunoja, A., Virtanen, A., Klein Baltink, H., Henzing, J. S. B., Größ, J., Gobbi, G. P., Wiedensohler, A., Kiendler-Scharr, A., Decesari,

S., Facchini, M. C., Weingartner, E., and Baltensperger, U.: Vertical profiling of aerosol hygroscopic properties in the planetary boundary layer during the PEGASOS campaigns, *Atmospheric Chemistry and Physics*, 16 (11), 7295–7315, https://doi.org/10.5194/acp-16-7295-2016, 2016.

Sandu, A. and Chai, T.: Chemical Data Assimilation—An Overview, *Atmosphere*, 2 (3), 426–463, https://doi.org/10.3390/atmos2030426, 2011.

Schlosser, F., Maier, B. F., Jack, O., Hinrichs, D., Zachariae, A., and Brockmann, D.: COVID-19 lockdown induces disease-mitigating structural changes in mobility networks, *Proceedings of the National Academy of Sciences*, 117 (52), 32 883–32 890, https://doi.org/10.1073/pnas.2012326117, 2020.

Schuldt, T., Gkatzelis, G. I., Wesolek, C., Rohrer, F., Winter, B., Kuhlbusch, T. A. J., Kiendler-Scharr, A., and Tillmann, R.: Electrochemical sensors on board a Zeppelin NT: in-flight evaluation of low-cost trace gas measurements, *Atmos. Meas. Tech.*, 16 (2), 373–386, https://doi.org/10.5194/amt-16-373-2023, 2023.

Schultz, M. G., Schröder, S., Lyapina, O., Cooper, O. R., Galbally, I., Petropavlovskikh, I., von Schneidemesser, E., Tanimoto, H., Elshorbany, Y., Naja, M., Seguel, R. J., Dauert, U., Eckhardt, P., Feigenspan, S., Fiebig, M., Hjellbrekke, A.-G., Hong, Y.-D., Kjeld, P. C., Koide, H., Lear, G., Tarasick, D., Ueno, M., Wallasch, M., Baumgardner, D., Chuang, M.-T., Gillett, R., Lee, M., Molloy, S., Moolla, R., Wang, T., Sharps, K., Adame, J. A., Ancellet, G., Apadula, F., Artaxo, P., Barlasina, M. E., Bogucka, M., Bonasoni, P., Chang, L., Colomb, A., Cuevas-Agulló, E., Cupeiro, M., Degorska, A., Ding, A., Fröhlich, M., Frolova, M., Gadhavi, H., Gheusi, F., Gilge, S., Gonzalez, M. Y., Gros, V., Hamad, S. H., Helmig, D., Henriques, D., Hermansen, O., Holla, R., Hueber, J., Im, U., Jaffe, D. A., Komala, N., Kubistin, D., Lam, K.-S., Laurila, T., Lee, H., Levy, I., Mazzoleni, C., Mazzoleni, L. R., McClure-Begley, A., Mohamad, M., Murovec, M., Navarro-Comas, M., Nicodim, F., Parrish, D., Read, K. A., Reid, N., Ries, L., Saxena, P., Schwab, J. J., Scorgie, Y., Senik, I., Simmonds, P., Sinha, V., Skorokhod, A. I., Spain, G., Spangl, W., Spoor, R., Springston, S. R., Steer, K., Steinbacher, M., Suharguniyawan, E., Torre, P., Trickl, T., Weili, L., Weller, R., Xiaobin, X., Xue, L., and Zhiqiang, M.: Tropospheric Ozone Assessment Report: Database and metrics data of global surface ozone observations, *Elementa: Science of the Anthropocene*, 5, 58, https://doi.org/10.1525/elementa.244, 2017.

Schuyler, T. and Guzman, M.: Unmanned Aerial Systems for Monitoring Trace Tropospheric Gases, *Atmosphere*, 8, 206, https://doi.org/10.3390/atmos8100206, 2017.

Segales, A. R., Greene, B. R., Bell, T. M., Doyle, W., Martin, J. J., Pillar-Little, E. A., and Chilson, P. B.: The CopterSonde: an insight into the development of a smart unmanned aircraft system for atmospheric boundary layer research, *Atmospheric Measurement Techniques*, 13 (5), 2833–2848, https://doi.org/10.5194/amt-13-2833-2020, 2020.

Seinfeld, J. H. and Pandis, S. N.: Atmospheric Chemistry and Physics: From Air Pollution to Climate Change, John Wiley & Sons, Hoboken, NJ, 3rd edn., 2016.

Skamarock, W. C., Klemp, J. B., Dudhia, J., Gill, D. O., Barker, D. M., Duda, M. G., Huang, X.-Y., Wang, W., and Powers, J. G.: A Description of the Advanced Research WRF Version 3, https://doi.org/10.5065/D68S4MVH, 2008.

Sokhi, R. S., Moussiopoulos, N., Baklanov, A., Bartzis, J., Coll, I., Finardi, S., Friedrich, R., Geels, C., Grönholm, T., Halenka, T., Ketzel, M., Maragkidou, A., Matthias, V., Moldanova, J., Ntziachristos, L., Schäfer, K., Suppan, P., Tsegas, G., Carmichael, G., Franco, V., Hanna, S., Jalkanen, J.-P., Velders, G. J. M., and Kukkonen, J.: Advances in air quality research – current and emerging challenges, *Atmospheric Chemistry and Physics*, 22 (7), 4615–4703, https://doi.org/10.5194/acp-22-4615-2022, 2022.

Stull, R. B.: An Introduction to Boundary Layer Meteorology, Atmospheric and Oceanographic Sciences Library, Springer Netherlands, 2012.

Sun, Q., Vihma, T., Jonassen, M. O., and Zhang, Z.: Impact of Assimilation of Radiosonde and UAV Observations from the Southern Ocean in the Polar WRF Model, *Adv. Atmos. Sci.*, 37, 441–454, https://doi.org/10.1007/s00376-020-9213-8, 2020.

Tang, X., Zhu, J., Wang, Z. F., and Gbaguidi, A.: Improvement of ozone forecast over Beijing based on ensemble Kalman filter with simultaneous adjustment of initial conditions and emissions, *Atmos. Chem. Phys.*, 11 (24), 12 901–12 916, https://doi.org/10.5194/acp-11-12901-2011, 2011.

Tillmann, R., Gkatzelis, G. I., Rohrer, F., Winter, B., Wesolek, C., Schuldt, T., Lange, A. C., Franke, P., Friese, E., Decker, M., Wegener, R., Hundt, M., Aseev, O., and Kiendler-Scharr, A.: Air quality observations onboard commercial and targeted Zeppelin flights in Germany - a platform for high-resolution trace-gas and aerosol measurements within the planetary boundary layer, *Atmos. Meas. Tech.*, 15, 3827–3842, https://doi.org/10.5194/amt-15-3827-2022, 2022.

Umweltbundesamt: Greenhouse Gas Emissions in 2022 – Executive Summary: Stationary Installations and Aviation Subject to Emissions Trading Germany (2022 VET Report), Tech. rep., German Environment Agency (UBA), Dessau-Roßlau, Germany, https://www.umweltbundesamt.de/, accessed: March 2025, 2023.

Veefkind, J., Aben, I., McMullan, K., Förster, H., de Vries, J., Otter, G., Claas, J., Eskes, H., de Haan, J., Kleipool, Q., van Weele, M., Hasekamp, O., Hoogeveen, R., Landgraf, J., Snel, R., Tol, P., Ingmann, P., Voors, R., Kruizinga, B., Vink, R., Visser, H., and Levelt, P.: TROPOMI on the ESA Sentinel-5 Precursor: A GMES mission for global observations of the atmospheric composition for climate, air quality and ozone layer applications, *Remote Sensing of Environment*, 120, 70–83, https://doi.org/https://doi.org/10.1016/j.rse.2011.09.027, the Sentinel Missions - New Opportunities for Science, 2012.

Villa, T., Gonzalez, F., Miljievic, B., Ristovski, Z., and Morawska, L.: An Overview of Small Unmanned Aerial Vehicles for Air Quality Measurements: Present Applications and Future Prospectives, *Sensors*, 16, 1072, https://doi.org/10.3390/s16071072, 2016.

Vogel, A. and Elbern, H.: Identifying forecast uncertainties for biogenic gases in the Po Valley related to model configuration in EURAD-IM during PEGASOS 2012, *Atmos. Chem. Phys.*, 21 (5), 4039–4057, https://doi.org/10.5194/acp-21-4039-2021, 2021.

Waller, J. A., Dance, S. L., Lawless, A. S., and and, N. K. N.: Estimating correlated observation error statistics using an ensemble transform Kalman filter, *Tellus A: Dynamic Meteorology and Oceanography*, 66 (1), 23 294, https://doi.org/10.3402/tellusa.v66.23294, 2014.

Wang, Y., Sartelet, K. N., Bocquet, M., and Chazette, P.: Assimilation of ground versus lidar observations for PM10 forecasting, *Atmos. Chem. Phys.*, 13 (1), 269–283, https://doi.org/10.5194/acp-13-269-2013, 2013.

Wang, Y., Wang, J., Xu, X., Henze, D. K., Qu, Z., and Yang, K.: Inverse modeling of SO_2 and NO_x emissions over China using multisensor satellite data – Part 1: Formulation and sensitivity analysis, *Atmos. Chem. Phys.*, 20 (11), 6631–6650, https://doi.org/10.5194/acp-20-6631-2020, 2020.

Weaver, A. and Courtier, P.: Correlation modelling on the sphere using a generalized diffusion equation, *Q. J. Roy. Meteor. Soc.*, 127, 1815–1846, https://doi.org/10.1002/qj.49712757518, 2001.

WMO: Global Demonstration Campaign for Evaluating the Use of Uncrewed Aircraft Systems in Operational Meteorology: White Paper, White Paper WMO-No. 1318, World Meteorological Organization, Geneva, https://library.wmo.int/idurl/4/66308, 2023.

Wood, K., Liu, E. J., Richardson, T., Clarke, R., Freer, J., Aiuppa, A., Giudice, G., Bitetto, M., Mulina, K., and Itikarai, I.: BVLOS UAS Operations in Highly-Turbulent Volcanic Plumes, *Frontiers in Robotics and AI*, Volume 7 - 2020, https://doi.org/10.3389/frobt.2020.549716, 2020.

Xie, Y., Wu, X., Hou, Z., Li, Z., Luo, J., Lüddeke, C. T., Huang, L., Wu, L., and Liao, J.: Gleaning insights from German energy transition and large-scale underground energy storage for China's carbon neutrality, *International Journal of Mining Science and Technology*, 33 (5), 529–553, https://doi.org/10.1016/j.ijmst.2023.04.001, 2023.

Zhang, S., Tian, X., Han, X., Zhang, M., Zhang, H., and Mao, H.: Improvement of PM2.5 forecast over China by the joint adjustment of initial conditions and emissions with the NLS-4DVar method, *Atmos. Environ.*, 271, 118 896, https://doi.org/10.1016/j.atmosenv.2021.118896, 2022.

Zupanski, M.: A Preconditioning Algorithm for Four-Dimensional Variational Data Assimilation, *Mon. Wea. Rev.*, 124 (11), 2562 – 2573, https://doi.org/10.1175/1520-0493(1996)124<2562:APAFFD>2.0.CO;2, 1996.

Personal Acknowledgments

As my PhD journey comes to a close and a new path unfolds, I pause with gratitude to acknowledge all those whose support made this accomplishment possible.
Beginning a PhD in 2021 while in COVID lockdown and working entirely from home was difficult, but the assistance, practical support, and approachable supervision provided by my daily supervisor Dr. Anne Caroline Lange made it possible. Thank you for assisting me in overcoming every obstacle, for exhaustively reviewing my work, and for your encouragement, especially during the preparation of my first paper.
I would like to sincerely thank Prof. Dr. Andreas Wahner and Prof. Dr. Ulrich Löhnert for kindly dedicating their time to reviewing my thesis and evaluating my PhD work.
I am also thankful to Dr. Philipp Franke for his insightful supervision and careful examination of my thesis manuscript. His suggestions greatly enhanced the quality of my work, and his expert assistance with the EURAD-IM model was especially beneficial.
Sincere thanks to my fellow Regional Modelling research team members, Alex and Christoph, for their collaboration, instructive lunch-break discussions, and persistent support.
To Mohamed, thank you for reading my thesis with fresh eyes and offering honest feedback. Your encouragement over the past six months helped me through tough times. I'm so grateful; your support made a big difference.
To my parents, sisters, brother, and the entire family: thank you for your endless support, constant encouragement, and unwavering faith in me. Your belief has been my greatest motivation.
To my friends in my home country and those who were a step ahead of me in the PhD journey, thank you for your guidance and advice. Your insights and support helped me find my way.
Last but certainly not least, my deepest gratitude goes to my dear friend Fatima, who turned my PhD years—and my life in Germany—into something truly special. Meeting you through the GSGS graduate school wasn't just luck; it felt like destiny. Over these four years, we've shared ups and downs, weekends, travels, and countless unforgettable moments. Thank you, Fatima, for everything. I can't wait for our next trip together as doctors!